SYNTHESIS AND CHARACTERIZATION OF Mn-DOPED CdSe QUANTUM DOTS VIA INVERSE MICELLE TECHNIQUE

NOR ALIYA BINTI HAMIZI

THESIS SUBMITTED IN FULFILMENT OF THE REQUIREMENTS FOR THE DEGREE OF DOCTOR OF PHILOSOPHY

FACULTY OF ENGINEERING
UNIVERSITY OF MALAYA
KUALA LUMPUR

2017

UNIVERSITI MALAYA

ORIGINAL LITERARY WORK DECLARATION

Name of Candidate: Nor Aliya binti Hamizi

Registration/Matric No: KHA 110069

Name of Degree: Doctor of Philosophy

Title of Project Paper/Research Report/Dissertation/Thesis ("this Work"): Synthesis And Characterization Of Mn-Doped CdSe Quantum Dots Via Inverse Micelle Technique

Field of Study: Advance Materials/Nanomaterials

I do solemnly and sincerely declare that:

(1) I am the sole author/writer of this Work;
(2) This Work is original;
(3) Any use of any work in which copyright exists was done by way of fair dealing and for permitted purposes and any excerpt or extract from, or reference to or reproduction of any copyright work has been disclosed expressly and sufficiently and the title of the Work and its authorship have been acknowledged in this Work;
(4) I do not have any actual knowledge nor do I ought reasonably to know that the making of this work constitutes an infringement of any copyright work;
(5) I hereby assign all and every rights in the copyright to this Work to the University of Malaya ("UM"), who henceforth shall be owner of the copyright in this Work and that any reproduction or use in any form or by any means whatsoever is prohibited without the written consent of UM having been first had and obtained;
(6) I am fully aware that if in the course of making this Work I have infringed any copyright whether intentionally or otherwise, I may be subject to legal action or any other action as may be determined by UM.

Candidate's Signature Date

Subscribed and solemnly declared before,

Witness's Signature Date

Name:

Designation:

ABSTRACT

Various sizes of manganese-doped cadmium selenide quantum dots (Mn-doped CdSe QDs) synthesized using inverse Micelle technique with organic solvent and surfactant possesses zinc blende structure with physical size ranging from 3 to 14 nm and crystallite size 2.46 to 5.46 nm respectively for 0 to 90 mins samples with narrow size distribution. Mn-doped CdSe QDs observed to growth larger QDs compared to pure CdSe QDs at significantly same reaction times. The lattice parameter compressed with QDs sizes growth due to the introduction of lattice strain due to the incorporation of Mn atoms into CdSe QDs lattice. The Mn-doped CdSe QDs shows a slight blue-shift on absorption and emission spectra's compared to pure CdSe even though is possessed larger QDs. The band gap structure modification prominently affected by the lattice strain were transition of Stoke`s, Rayleigh to anti-Stoke`s shifts observed as the Mn-doped CdSe QDs size growth. The typical red-shift of absorption and emission wavelength observed with growth of QDs sizes. The role of oleic acid acid as a surfactant and capping agent shows in FTIR spectra. The lattice strain tailored the binding energy between the ion prominently on the surface of the QDs with growth of QDs sizes.

ABSTRAK

Pelbagai saiz Mangan-dop cadmium selenida titik terkurung (Mn-doped CdSe QDs) yang telah di sintesis dengan teknik ‘inverse Micelle’ mengunakan cecair dan ‘surfactant’ organik mempunyai struktur hablur ‘zinc blende’ dengan saiz fizikal dalam julat daripada 3 ke 14 nm dan Saiz hablur daripada 2.46 hingga 5.46 nm untuk sampel-sampel 0 hingga 90 minit dengan taburan saiz yang rendah. Mn-doped CdSe QDs menghasilkan QDs dengan saiz yang lebih besar berbanding CdSe QDs. Jarak kekisi hablur mengalami pemampatan apabila size QDs meningkat disebabkan oleh daya tarikan ke atas kekisi hablur. Menariknya, Mn-doped CdSe QDs menunjukkan anjakan biru berbanding CdSe QDs walaupun ia menghasilkan QDs dengan saiz yang lebih besar. Struktur jalur orbit Mn-doped CdSe QDs mengalami perubahan besar disebabkan oleh daya tarikan ke atas kekisi hablur yang mengakibatkan perubahan dari peralihan Stoke`s, Rayleigh seterusnya anti-Stoke`s apabila saiz QDs meningkat. Peralihan dari panjang gelombang rendah kepada tinggi dilihat daripada spectrum serapan dan spectrum lepasan dengan peningkatan saiz QDs. Peranan asid oleic sebagai ‘surfactant’ dan ajen penyalut dibuktikan dalam spectrum FTIR. Daya tarikan boleh mengubahsuai tenaga ikatan antara ion-ion terutamanya di permukaan QDs juga dengan peningkatan saiz QDs.

ACKNOWLEDGEMENT

All Praise Be to Allah S.W.T. for granting me the knowledge, inspiration, patience, perseverance and serenity to complete my Phd research. My warmest appreciation goes to my kind and respected supervisor, Prof. Dr. Mohd Rafie Johan, for his continuing guidance and support. This research has been meaningful and rewarding to me because I had the opportunity to work under a supervisor who is always willing to lend me a helping hand in order for me to give my best in this research work. I am eternally grateful to my beloved family for their endless encouragement, support and prayers, and for always being there for me through the thick and thin. I would not be able to complete my Phd journey without my family's assistance, especially my lovely mother Madam Mashitah binti Sulaiman, my kind father Mr. Hamizi bin Adin, my beloved husband, Mr. Shahrol Nizam bin Shamsudin. This work is specially dedicated to my beautiful children`s Izz iman bin Shahrol Nizam and Zara Saffiya binti Shahrol Nizam. My special gratitude goes to MyBrain15 scholarship and Malaysia Ministry of Higher Education for the financial support throughout my Phd study. My heartfelt thanks go to my lecturers, lab assistants and the support staff of Department of Mechanical Engineering. Thank you for making my Phd researches a wonderful and enjoyable learning experience despite the number of obstacles, and I wish you all the best.

TABLE OF CONTENT

DECLARATION……..……ii

ABSTRACT……iii

ABSTRAK……...iv

ACKNOWLEDGEMENT……v

TABLE OF CONTENT……...vi

LIST OF FIGURES……viii

LIST OF TABLES……...xi

LIST OF ABBREVIATIONS……xii

CHAPTER ONE……1

INTRODUCTION……1

1.1 Background……1

1.2 Important Research Problem……5

1.3 Significance of Research……...……5

1.4 Research Objectives…….....6

CHAPTER TWO……...7

LITERATURE REVIEW……7

2.1 Quantum Dots……7

2.2 Synthesis Techniques of QDs Materials……....9

2.3 Materials in QDs……...……...22

2.4 Doping in QDs……27

2.5 Quantum Confinement Effect……..30

2.6 Synthesis of Mn-doped CdSe QDs……..35

2.7 Mechanism in Synthesizing Mn-doped CdSe QDs……38

2.8 Strain in QDs……...……41

CHAPTER THREE……46

METHODOLOGY……46

3.1 Materials……..46

3.2 Samples Preparation……47

3.3 Samples Characterizations……...48

CHAPTER FOUR……...……51

RESULTS AND DISCUSSIONS……...……51

4.1 Physical Observations……51

4.2 High Resolution Transmission Electron Microscopy (HRTEM) Analysis……...53

4.3 X-ray Diffraction Analysis……..70

4.4 Ultraviolet Visible (UV-vis) Analysis……83

4.5 Photoluminescence (PL) Analysis……...90

4.6 Fourier Transform Infra-red (FTIR) Analysis……...……..99

4.7 Raman Spectroscopy Analysis……..101

4.8 X-ray Photoelectron Spectroscopy (XPS) Analysis……..105

4.9 Mechanism of Mn-doped CdSe QDs Formation……...119

CHAPTER FIVE……...121

CONCLUSION……121

FURTHER RECOMMENDATIONS……...122

REFERENCES……xx

LIST OF PUBLICATIONS……..xliii

APPENDIX……...xliv

LIST OF FIGURES

Figure 2.1: The general Williamson-Hall plot……..……43

Figure 3.1: The experimental setup for Mn-doped CdSe QDs sample upon Cd-Mn solution injection into Se solution……..48

Figure 3.2: Flow chart of characterization of Mn-doped CdSe QD……..……50

Figure 4.1: Mn-doped CdSe QDs samples with various colours at various reaction time: (a) 0 , (b) 0.2, (c) 0.5, (d) 1, (e) 5, (f) 16, (g) 46 and (h) 90 mins….52

Figure 4.2: HRTEM image of Mn-doped CdSe QDs with QDs size distribution (insert) at 0 min reaction time…….55

Figure 4.3: HRTEM image of Mn-doped CdSe QDs with QDs size distribution (insert) at 0.2 min reaction time……..56

Figure 4.4: HRTEM image of Mn-doped CdSe QDs with QDs size distribution (insert) at 0.5 min reaction time……..57

Figure 4.5: HRTEM image of Mn-doped CdSe QDs with QDs size distribution (insert) at 1 min reaction time…….58

Figure 4.6: HRTEM image of Mn-doped CdSe QDs with QDs size distribution (insert) at 5 min reaction time…….59

Figure 4.7: HRTEM image of Mn-doped CdSe QDs with QDs size distribution (insert) at 16 min reaction time……...60

Figure 4.8: HRTEM image of Mn-doped CdSe QDs with QDs size distribution (insert) at 46 min reaction time……...61

Figure 4.9: HRTEM image of Mn-doped CdSe QDs with QDs size distribution (insert) at 90 min reaction time……...……62

Figure 4.10: Relationship of QDs physical size with reaction times……..63

Figure 4.11: HRTEM image of Mn-doped CdSe QDs lattice of 0 min sample.……..65

Figure 4.12: HRTEM image of Mn-doped CdSe QDs lattice of 0.2 min sample……65

Figure 4.13: HRTEM image of Mn-doped CdSe QDs lattice of 0.5 min sample……66

Figure 4.14: HRTEM image of Mn-doped CdSe QDs lattice of 1 min sample……...66

Figure 4.15: HRTEM image of Mn-doped CdSe QDs lattice of 5 min sample……...67

Figure 4.16: HRTEM image of Mn-doped CdSe QDs lattice of 16 min sample…….67

Figure 4.17: HRTEM image of Mn-doped CdSe QDs lattice of 46 min sample…….68

Figure 4.18: HRTEM image of Mn-doped CdSe QDs lattice of 90 min sample…….68

Figure 4.19: XRD patterns of Mn-doped CdSe QDs samples at various reaction times……..…….71

Figure 4.20: Plot of $\beta_r cos\theta$ versus $sin\theta$ from XRD data of 0 min sample……...…76

Figure 4.21: Plot of $\beta_r cos\theta$ versus $sin\theta$ from XRD data of 0.2 min sample……76

Figure 4.22: Plot of $\beta_r cos\theta$ versus $sin\theta$ from XRD data of 0.5 min sample……77

Figure 4.23: Plot of $\beta_r cos\theta$ versus $sin\theta$ from XRD data of 1 min sample……...…77

Figure 4.24: Plot of $\beta_r cos\theta$ versus $sin\theta$ from XRD data of 5 min sample……...78

Figure 4.25: Plot of $\beta_r cos\theta$ versus $sin\theta$ from XRD data of 16 min sample…….78

Figure 4.26: Plot of $\beta_r cos\theta$ versus $sin\theta$ from XRD data of 46 min sample…….79

Figure 4.27: Plot of $\beta_r cos\theta$ versus $sin\theta$ from XRD data of 90 min sample…….79

Figure 4.28: Lattice strain effect with growth of Mn-doped CdSe QDs crystallite size……...81

Figure 4.29: Temporal evolution of UV-vis absorption spectra for the as-synthesized Mn-doped CdSe QDs at different reaction times……84

Figure 4.30: The Tauc`s plot of Mn-doped Cdse QDs at various reaction times……86

Figure 4.31: Temporal evolution of Mn-doped CdSe QD optical band gap and exciton energy against their crystallite radius……..89

Figure 4.32: PL emission spectra of Mn-doped CdSe QDs samples……..92

Figure 4.33: The evolution of exciton and emission energy of Mn-doped CdSe QDs various sizes…….96

Figure 4.34: The approximation of carrier energy structure evolution of Mn-doped CdSe QDs throughout different reaction times……...…97

Figure 4.35: The approximation of carrier energy structure evolution of pure CdSe QDs throughout different reaction times (Hamizi & Johan, 2010)….....98

Figure 4.36: The FTIR pattern of paraffin oil, oleic acid and Mn-doped CdSe QDs at various reaction time and……...100

Figure 4.37: Raman scattering spectra of Mn-doped CdSe QDs at various reaction times……..103

Figure 4.38: XPS wide scan of Mn-doped CdSe QDs at different reaction times ……...107

Figure 4.39: XPS scan of Cd 3d traced for Mn-doped CdSe QDs samples……...110

Figure 4.40: The XPS scan of Se traced for Mn-doped CdSe QDs at various reaction times……..112

Figure 4.41: XPS scan for Mn traced for Mn-doped CdSe QDs at various reaction time……114

Figure 4.42: Relation between peak intensity and the variation in size of Mn-doped CdSe QDs……..118

LIST OF TABLES

Table 2.1: Chronological summary of hot-solution decomposition methods of various size QDs.....15

Table 3.1: Details of chemical materials used in synthesis of Mn-doped CdSe QDs samples……...46

Table 4.1: Lattice parameter of Mn-doped CdSe QDs for all samples……...69

Table 4.2: FWHM of (111) XRD peaks and the calculated crystallite sizes of Mn-doped CdSe QDs at various reaction times……72

Table 4.3: FWHM of XRD diffraction peaks of Mn-doped CdSe QDs correspond to (111), (220) and (311) planes……73

Table 4.4: The optical and exciton energy of Mn-doped CdSe QDs changes with crystallite size……89

Table 4.5: Raman scattering parameters and excitation wavelengths for various sizes of Mn-doped CdSe QDs samples……104

Table 4.6: Full width at half maximum of XPS peak of Mn-doped CdSe QDs for different reaction times……118

LIST OF ABBREVIATIONS

%	Percentage
(*hkl*)	Atomic unit cell
$\Delta(lnV)$	Fractional volume change
ΔE_e	Emission photon energy
ΔE_g	Shift of band gap energy
ΔE_{go}	Unstrained semiconductor band gap energy
ΔE_i	Exciton photon energy
ΔE_v	Stokes shift photon energy difference
1s	First electron configured in sharp orbital
2LO	First overtone of longitudinal optical
2p	Second electron configured in principle orbital
3d	Third electron configured in diffuse orbital
Å	Amstrong (unit)
A	Constant
a	Negative deformation potential
a.u.	Arbitrary unit
Ac	Acetate
Ag	Silver
Ag_2S	Silver (II) sulfide
Ag_2Se	Silver (II) selenide
AlGaAs	Aluminum Galium Arsenide
AOT	Aerosol OT
Ar	Argon
atm	Standard atmosphere pressure
Au	Gold

B	Boron
C	Carbon
c	Intercept at y-axis
c	Speed of light
$C_{36}H_{66}MnO_4$	Manganese-oleate
$C_{36}H_{70}CdO_4$	Cadmium-oleate
Cd	Cadmium
$CdMe_2$	Dimetyl cadmium
CdS	Cadmium selenide
CdSe	Cadmium selenide
CdTe	Cadmium telluride
CFQDs	Cadmium free quantum dots
CH_2	Methylene or carbene
CH_3	Methyl group
CH_4	Methane
cm	Centimeter (unit)
Co	Cobalt
Co.sol	Coordinating solvent
C-QDs	Carbon quantum dots
Cr	Cromium
CTAB	Cetyl trimethyl-ammonium bromide
Cu	Cooper
CV	Cyclic voltametry
d	Diameter
D_A	Area weighted average
DDA	Dodecylamine

DEPE	1,2-bis(diethyl-phosphino)-ethane
DMPA	2,2 –dimethoxy-2-phenylacetophenone
DMS	Diluted magnetic semiconductor
DNA	Deoxyribonucleic acid
D_V	Volume weighted average
e	Charge of electron
ε	Dielectric constant
E	Energy primary to photon energy
E_g	Band gap energy
EGDMA	Ethylene glycol domethacrylate
EMA	Effective mass approximation
E_{Ry}^*	Rydberg energy
Et	Ethyl
eV	Electron volt (unit)
Fe	Iron
FIB	Focused ion beam
FTIR	Fourier Transform Infrared Spectroscopy
FWHM	Full-width at half maximum
g	gram (unit)
g/ml	gram per milliliter (unit)
g/mol	gram per molar (unit)
Ga	Galium
GaAs	Galium Arsenide
GPa	Gigapascal (unit)
GQDs	Graphene quantum dots
h	Plank`s constant

$\hbar$	Reduced Plank`s constant
H_2	Hidrogen
HAD	Hexadecylamine
Hg	Mercury
HgTe	Mercury telluride
HOMO	Highest occupied molecular orbital
HPA	Hexyl-phosphonic acid
HRTEM	High Resolution Transmission Electron Microscopy
I	Electron intensity
I_{2LO}	Peak intensity of first overtone of longitudinal optical
I_{LO}	Peak intensity of longitudinal optical
I_{max}	Maximum peak intensity
InP	Indium phosphate
J	Photon flux
j	Total electronic angular momenta
K	Instrumental factors
k	Scherrer`s constant
$\hat{k}$	Wave vector
kV	Kilo volt (unit)
L	Crystallite size
l	Total orbital angular or angular quantum number
LA	Lauric acid
LCAO	Linear combination of atomic orbitals
Li	Litium
LO	Longitudinal optical
$LP(\theta)$	Lorentz and polarization factor

LUMO	Lowest un-occupied molecular orbital
m^*	Effective mass
m_e	Effective mass of electrons
Me	Methyl
meV	Milli electron volt (unit)
Mg	Magnesium
m_h	Effective mass of holes
M_{hkl}	Multiplicity
min	Minute
ml	milliliter (unit)
mm	Millimeter (unit)
MMA	Methylmethacrylate
Mn	Manganese
MPA	Marcaptopropionic acid
MRI	Magnetic resonance imaging
N	Nitrogen
Na	Sodium
NaOH	Sodium hydroxide
NCs	Nanocrystals
NIR	Near infrared
OA	Oleic acid
ODA	Octadecylamine
ODE	1-octadecene
P	Phosphorus
PbS	Lead sulfide
PEG	Polyetylynglicol

PL	Photoluminescence
QDs	Quantum dots
QY	Quantum yield
R	Crystal size
r	Radius
$r_{(dot)}$	Radius of quantum dots
r_B	Bohr radius
$R\text{-}CH_3(CH_2)nCH_3$	Paraffin oil
RIE	Reactive ion etching
RNA	Ribonucleic acid
s	Spin momenta or spin quantum number
S	Sulfur
$S_{(hkl)}$	Structural factor
s^{-1}	Per second
SA	Stearic acid
SDS	Sodium dodecyl sulphate
Se	Selenium
sec	Second
SERS	Enhanced raman spectroscopy
Si	Silicon
SO	Surface optical
TBP	Tri-n-butyl phosphine
TCH	Thompson-Cox-Hasting function
TDPA	Tetradecylphosphonic acid
Te	Tellurium
tech TOPO	Technical grade TOPO

temp	Temparature
TF(θ)	Temperature factor
TMPPA	Phosphonic acid
TMS	Trimethyl-silyl
TOA	Trioctyl amine
TOP	Trioctylphosphine
TOPO	Tri-n-octyl-phophine oxide
TOPSe	Trioctylphosphine selenide
UCPL	Up converted photoluminescence
UV	Ultra-violet
UV-vis	Ultra-violet visible spectroscopy
W	Molar ratio of water and surfactant
XPS	X-ray photoelectron spectroscopy
XRD	X-ray Diffractometer
Zn	Zinc
ZnO	Zinc oxide
ZnS	Zinc sulfide
ZnSe	Zinc selenide
ZnTe	Zinc Teluride
α	Absorption intensity
β	Peak broadening primary refer to full-width at half maximum
β_i	Broadening by instrument factor
β_o	Observed broadening
β_r	Broadening by crystallite size and strain
Γ_G	Thompson-Cox-Hasting function in Gaussian term
Γ_L	Thompson-Cox-Hasting function in Lorentzian term

η	Strain
θ	Bragg angle
λ	Wavelength
μ	Reduced mass
ρ	Concentration of the atom or ion in the solid
σ	Cross-section for photoelectron production
υ	Frequency
υ_o	Exciton frequency
υ_v	Stokes shift frequency
$\boldsymbol{\lambda}$	Electron attenuation length

CHAPTER ONE

INTRODUCTION

1.1 Background

Quantum confinement effect in quantum dots (QDs) II-VI group semiconductors is prominently factor that contributed to the great optical and electronic properties (Dongzhi et al., 2007). Thus, it had been intensively use in wide range of industrial applications such in laser, bio-medical imaging and labels and light-emitting diodes (Alivisatos, 1996; Lee et al., 2006; Klimov et al., 2000; Leatherdale et al., 2000; Bruzhez et al., 1998; Crooker et al., 2003; Sung et a., 2006; Murray et al., 1993; Peng et al., 1998). Cadmium selenide (CdSe) QDs is the II-VI semiconductor nanocrystal that profoundly shows almost full range of visible light emission within a reasonable size range compared to the other colloidal semiconductor nanocrystals (Sung et al., 2008). Since technology and applications are moving faster with time, the need to produce more sufficient QDs to fulfill the application need and is crucial to the research field all around the world. Many reported works on altering the QDs properties by introducing several doping elements to create core-shell QDs for improving or tailoring the QDs properties to meet the need of applications (Jiang et al., 2012).

Effort on doping of QDs was arise since it is realize that the pure QDs experience unpassivated surface due to the low atomic coordination numbers at the surface compare to interior atoms. Hence, incomplete bonding relative to the interior atoms forms unpassivated orbitals that are localized and carry a slight negative and positive charge (Smith & Shuming, 2010). This inhomogenous charge will weakly

interact among them and form a band structure. If the energy of the unpassivated orbitals band fall within the semiconductor band gap, then electron and holes can be trapped at the surface of the crystal (Pokrant & Whaley, 1999). Example like in CdSe QDs system, Cd unpassivated orbitals role as electron trap while Se unpassivated orbitals role as hole trap. In addition, surface defect can also induce charges carrier trap. This phenomenon induced non-radiative recombination resulting decrease of fluorescence quantum yield. Introduction of surface bound organic ligand is generally used to passivate the surface trap. System like CdSe QDs, the use of tri-n-octylphosphine oxide (TOPO) and trioctylphosphine (TOP) were use as surface passivated and as a surfactant that control the growth of CdSe QDs (Peng et al., 1997). Despite simultaneous surface passivation by organic ligand are difficult for both anionic and cationic surface trap since the QDs surface is incompletely covered by organic ligand due to steric hindrance between bulky organic ligand (Peng et al., 1997; Peng et al., 2000). Furthermore, many have reported the doping of inorganic semiconductor shell onto the QDs surface enables the simultaneous passivation of anionic and cationic surface trap since the probability for excitons to decay through radiative path increase (Pokrant & Whaley, 1999).

Most common doping of CdSe QDs core-shell was the doping of shell with larger band gap energy compare to the one possesses by the core elements. This is in objective of creating band gap heterostuctures and significantly improve the surface passivation (Peng et al., 1997). Example like synthesized of ZnS/CdSe, CdS/CdSe and ZnSe/CdSe core-shell QDs are efficiently improved the quantum yield to about ~80 % (Mekis et al., 2003; Ivanov et al., 2004; Reiss et al., 2002).

Equally important, the doped of intrinsically small transition metal atoms such as magnesium (Mg) (Kwak et al., 2007), manganese (Mn) (Shen et al., 2016; Hou et al., 2016; Norris et al., 2001), zinc (Zn) (Kwak et al., 2007), copper (Cu) (Meulenberg et al., 2004), cobalt (Co) (Giribabu et al., 2013) and iron (Fe) (Das et al., 2014) into variety of II-VI semiconductor QDs to achieve tunable, intense and optical and electronic properties. Among II-VI QDs semiconductor core-shell, CdSe QDs doped with Mn^{2+} catch an interest since it was the simplest way to tune the emission wavelength due to the significantly smaller Mn atom (~0.8 nm) compared to host CdSe atom. The Bawendi group, reported for the first time the successful of synthesized Mn-doped CdSe QDs by organometallic decomposition technique using complex organometallic compound $\{Mn_2(u\text{-}SeMe)_2(CO)_8\}$ (Miculec et al., 2000). A few years later, Erwin et al. (2005), reported that the surface absorption energy during the QDs growth are controlled by impurity incorporation. They proposed that the {001} facets in zinc blende CdSe QDs possesses higher binding energy (~4 – 6 eV) compred to any facets in wurtzite CdSe QDs (Erwin et al., 2005; Sung et al., 2008). Based on this, it is strongly believe that the intention to doped Mn into CdSe are highly restricted to self-purification in it wurtzite structure (Erwin et al., 2005; Sung et al., 2008). A great successful of Mn doping in CdSe with a zinc blende structure was predicted by the density-functional theory (Perdew et al., 1996). Furthermore, Mn-doped CdSe QDs have thermal stability and strong confinement of excited electrons and holes which lead to great optical and electronic properties compared to the un-doped CdSe bulk semiconductor (Kwak et al., 2007).

It has been reported by many researcher on the synthesis of CdSe QDs, such as single molecule precursor route (Green & O`Brien, 1999; Castro et al., 2003), solvothermal route (Guifu et al., 2006; Linhui et al., 2013), sonochemical route

(Yupapin et al., 2011), microwave irradiation route (Schumacher et al., 2009), organometallic precursor route (Murray et al., 1993; Hambrock et al., 2002) and non-organometallic precursor route (Qu et al., 2001; Bullen & Mulvaney, 2004). The popular wet-chemical synthesis methods of CdSe QDs using the coordinating solvents such as TOPO and TOP, which hundreds of papers are published based on this route (Yu & Peng, 2002). However, only little knowledge has been obtained for the formation mechanism of the CdSe QDs by the TOP-Based route (Deng et al., 2005). Furthermore, the costs for large-scale synthesis of QDs are still very high since TOP is expensive. In addition, TOP is hazardous, unstable, and non-environmental friendly solvent (Deng et al., 2005). Therefore, to attain the need of mass production, low cost, greener and fast synthesis process of QDs crucially for various applications, non-TOP based routes are more favorable (Deng et al., 2005). In this respect, high quality zinc blende CdSe QDs are synthesized using non-TOP based routes which organic solvent and surfactant such as paraffin oil and oleic acid were used. Deng et al. (2005) purposed the non-TOP mechanism of CdSe QDs formation via inverse Micelle approach which they successfully synthesized the high quality zinc blende CdSe QDs with oleic acid capping (Deng et al., 2005). For extended studies of CdSe QDs with Mn doping, Kwak et al. (2007) and Sung et al. (2008) used Mn acetate as a Mn precursor, for synthesizing high quality zinc blende Mn-doped CdSe QDs (Kwak et al., 2007; Sung et al., 2008)

In this work, we synthesized Mn-doped CdSe QDs using greener inverse Micelle technique which oleic acid was used as an organic ligand to the QDs surfaces and controling the QDs. Our work is different with Kwak et al. (2007) and Sung et al. (2008) because we synthesized and studied the properties of Mn-doped CdSe QDs at various sizes (Kwak et al., 2007; Sung et al., 2008).

1.2 Important Research Problem

In semiconductor nanocrystal system such CdSe QDs, the crystal surface condition are extremely crucial since the charge carrier transition at a crystal surface draw a significant modification on the electronic and optical properties of CdSe QDs. However, pure QDs such CdSe, will experienced surface defect that acted as a charge carrier trap resulting the probability increase of non-radiative recombination which reduces the fluorescence quantum yield (Talapin et al., 2001). In addition, similar to many other QDs, CdSe QDs possesses high surface area which results in high surface energy. Therefore, it is thermodynamically unstable or metastable (Devi et al., 2014). Much effort has been put by researcher to encounter this problem by introducing dopants into the CdSe QDs surface (Kwak et al., 2007). Surface doping using smaller transition metal (i.e. Mn, Mg and Zn) onto QDs surface are one of the simplest way to tune the light emission wavelength (Sung et al., 2008; Kwak et al., 2007). Among them, Mn incorporation into CdSe QDs promised a high density diluted semiconductor for spintronic application and provide good traps for excitation electrons which significant for electronic and optoelectronic devices (Devi et al., 2014). However, doping of Mn^{2+} into CdSe QDs is limited due to the self-purification for QDs with wurtzite structure (Perdew et al., 1996).

1.3 Significance of Research

CdSe semiconductor QDs has shown almost full range visible light emission within a reasonable size range compared to other colloidal semiconductor nanocrystals (Sung et al., 2008). Thus, this work significantly extended the research of CdSe QDs by introducing Mn^{2+} into various sizes of CdSe QDs and enhanced the electronic and

optical properties of the QDs for various applications such as light-emitting diodes, lasers and biological labels (Sung et al., 2008; Klimov et al., 2000). In addition, the greener inverse Micelle technique was applied using organic ligand that is oleic acid. This organic surface bound improved the QDs surface trap passivation of Mn-doped CdSe QDs which then increase the quantum yield (Talapin et al., 2001). Moreover, inverse Micelle technique is successfully used to doped Mn into CdSe QDs without the risk of self-purification of Mn dopants as reportedly experience by wurzite CdSe QDs (Sung et al., 2007). Mn-doped are predicted to optimize the surface simultaneously pasivation of anionic and cationic surface trap states that cannot be overcome by organic ligand (Talapin et al., 2001). In addition, Mn^{2+} corporation will introduce strain to the CdSe QDs lattice which enable the tuning of inter-band energy structure. This will promise the tunable of overall optical and electronic properties (Kwak et al., 2007).

1.4 Research Objectives

Objectives of this research are:

1. To synthesize colloidal Mn-doped CdSe QDs via inverse Michelle technique
2. To characterize Mn-doped CdSe QDs using several analytical techniques
3. To investigate the effect of varying the QDs size with its properties

CHAPTER TWO

LITERATURE REVIEW

This chapter describes the comprehensive background studies of Mn-doped CdSe QDs including the possible synthesis techniques. The quantum confinement effect also included in this chapter hence it is highly critical to describe the properties of the QDs and doped QDs at various sizes. The possible mechanism of synthesizing Mn-doped CdSe QDs is also included in this chapter for fundamental understanding of the chemical reactions involved.

2.1 Quantum Dots

Quantum dots (QDs) were discovered in the mid of 1980's when scientist found unusual behavior of confined semiconductor atoms after the laser are stimulated to a large amount of porous silicon samples. They discovered a new phenomenon of a red light emission from silicon atom after been stimulated with laser. Prior to this, it is only possible with connecting a diode to the electricity source (Brus, 1983; Brus, 1986; Reed et al., 1988). Ekimov (1981) was the first discovered the present of QDs in a glass matrix (Ekimov , 1981; Ekimov et al., 1985; Ekimov & Efros, 1988). Then Brus (1986) discovered the QDs in a colloidal solution. He derived the relationship of size and bandgap for semiconductor nanoparticles by apply a particle in a sphere model approximation to the wave function for bulk semiconductors (Brus, 1986).

However, the term 'quantum dots' (QDs) is originally created by Reed in 1988 which defined as three-dimensional confined semiconductor quantum well (Reed et al.,

1988). In his paper, the electronic transport through QDs shows fine structure in resonant tunneling which due to the discrete density of states in zero-dimensional system (Reed et al., 1988).

Generally, QDs is defined as a semiconductor materials which having nanoscale dimension (1- 100 nm) and highly confined in three spatial dimensions of either electron pair or electron-hole (Dabbousi et al., 1997; Hamizi & Johan, 2010). The electronic properties of QDs lie between bulk semiconductor and materials with discrete molecules with almost similar sizes (Noris & Bawendi, 1996; Peng, 2000; Suyver et al., 2000). The optoelectronic properties of QDs such as band gap are highly tunable as a function of particles size and shape. Thus, it is possible to manipulate the emission or absorption wavelengths by controlling the particles size to meet the specific application (Murray et al., 2001; Brus, 2008). This serves as a basis to produce efficient semiconductor lasers and optical amplifier, which are precisely tuned (Suri & Mehra, 2007). Furthermore, QDs promise the properties which could be harnessed for a wide range of electronic and optical applications such as solar cells, transistor and laser diode (Ji et al., 2003; Kasuya, 2004).

Beyond the optical and electronic applications, QDs has been applied in in-vivo and in-vitro bioimaging and diagnostic of living cell as a substitute of conventional organic dyes. The tunability of QDs fluorescence as a function of size are widely available for biomedical application such as in surface enhanced raman spectroscopy (SERS) and magnetic resonance imaging (MRI) contrast agent (Lee et al., 2013; Dahan et al., 2003; Sapford et al., 2006).

2.2 Synthesis Techniques of QDs Materials

There are two major approaches for fabrication of QDs semiconductor materials which is bottom-up and top-down methods (Bera et al., 2012).

In basis, the top-down method is the thinning or refining of bulk semiconductor to form the QDs. Electron beam lithography, reactive-ion etching and wet chemical etching is typical of top-down methods. Focused ion or laser beams are also used to form arrays of QDs, however incorporation of impurities into the QDs and structural imperfections by patterning have been it a major drawback. QDs are also widely fabricated using etching technique. Dry etching for example is a plasmonic process, which is operate by filling the etching chamber with a reactive gas species and a radio frequency voltage is applied to in order to break down the gas molecules to form more reactive fragment. These high kinetic energy species hit the surface and form a volatile reaction product that will etch a patterned sample. In reactive ion etching (RIE), the energetic species consist of ion, and with a masking pattern, selective etching of the substrate can be produce (Bera et al., 2006). A Galium arsenide/Aluminium gallium arsenide (GaAs/AlGaAs) quantum structure (~40 nm) has been successfully fabricated using RIE by mixing boron trichloride and argon (Scherer et al., 1987). Furthermore, RIE also reported to be use in production of close-packed arrays of zinc telluride (ZnTe) QDs with interdot distance of 180 - 360 nm using methane (CH_4) and hydrogen (H_2) (Tsutsui et al., 1993). Focused ion beam (FIB) techniques also can be use in fabricating QDs. This techniques use molten metal source such as gallium (Ga) are sputter to the surface of the semiconductor substrate in order to fabricate QDs with shape, size and inter-particle distance that mold by the size and dimension of ion beam (Chason et al., 1997). However this is a slow, low throughput process and requires expensive

equipment that leaves residual surface damage (Bera et al., 2010). Another method to fabricating pattern QDs is electron beam lithography followed by etching or lift-off processes. This method was successfully employed for the synthesis of III-V and II-VI QDs with particle sizes as small as 30 nm (Bera et al., 2010).

The bottom-up methods can be subdivided into wet-chemical and vapor-phase methods (Bera et al., 2012). The main components in the wet-chemical methods are the chemical precursors, surfactant and solvent (Murray et al., 2000; Zherebetskyy et al., 2014). In basis, wet-chemical method is the precipitation methods in solution with precise control of parameters such as synthesis temperature, precursor concentration, ratios of anionic to cationic species, micelle formation and synthesis time, which is crucial in order to get desirable average QDs size, shape and composition. Furthermore, it can be in a single solution or mixture of solutions. The precipitation process always involves both nucleation and controlled growth of QDs (Murray et al., 2000; Zherebetskyy et al., 2014). Nucleation can be classified as homogeneous, heterogeneous or secondary nucleation. Homogeneous nucleation occurs when solute atoms or molecules combine and reach a critical size without the assistance of a pre-existing solid interface (Burda et al., 2005).

Initially, wet-chemical method in QDs production was pioneered by Louis Brus in the late 1970s when he was in Bell Labs, and carried on by some of his post docs, notably Paul Alivisatos and Moungi Bawendi (Bera et al., 2006; Klimov et al., 2000).

Sol-gel is one of the techniques that fall into the wet-chemical methods category which have been used for many years to form QDs (Bang et al., 2006; Spanhel & Anderson, 1991; Bera et al., 2008). The three main steps in sol-gel technique are

hydrolysis, condensation (sol formation) and growth (gel formation). Sol is product of condensed metal precursor (alkoxides, acetates or nitrates) that been hydrolyzed in a solvent that dispersed by Brownian motion. Next, the polymerization process is conduct to produce a gel (Bera et al., 2010). Previously, many II-VI and IV-VI type of QDs successfully prepared by using this method such as cadmium sulfide (CdS) (Spanhel, 1987), zinc oxide (ZnO) (Bang et al., 2006; Spanhel & Anderson, 1991; Bera et al., 2008) and lead sulfide (PbS) (Sashchiuk et al., 2002). Example of this sol-gel method was the production of ZnO QDs by mixing the Zinc acetate in alcohol and sodium hydroxide (NaOH), followed by control aging in air (Bang et al., 2006). This incomplex and economical method is suitable for mass production. However, sol-gel process produced wide size distribution and a high concentration of defects which make it sparingly use for QDs production (Sashchiuk et al., 2002; Bera et al., 2010).

Microemulsion is another popular wet-chemical method that is popular because of its simplicity and can be operates at room temperature. There are two type of microemulsion which is normal microemulsion (oil-in-water) and inverse microemulsion (water-in-oil). It is quit straight forward that inverse microemulsion produce inverse micelle, and this methods is popular among the scientist to produce QDs compared to normal microemulsion. To create emulsion of inverse micelle, two unmixable liquid that is polar solvent (i.e. polar water or polar alcohol), non-polar solvent (i.e. non-polar long-chain alkane) and surfactant are mixed and stirred. As a result, the nano-size water or alcohol droplets dispersed in the n-alkane solution which is due to the contribution of surfactant that increases the surface tension of the water or alcohol droplet. Surfactant like Aerosol OT (AOT), cetyl trimethyl-ammonium bromide (CTAB), sodium dodecyl sulphate (SDS) or triton-X are the common surfactant use in this method. Surfactants are terminated by hydrophilic and hydrophobic groups on

opposite ends, which form numerous tiny droplets called micelles that are thermodynamically stable in the sustained oil medium. These micelles role as 'nanoreactors'. Highly rapid stirring micellar solutions lead to a continuous exchange of reactants due to dynamic collisions (Bera et al., 2010). The QDs size growth is restricted by the micelle size which is controlled by the molar ratio of water and surfactant (W) (Hoener et al., 1992).

The relation between W and the radius (r) of the micelle has been reported as are shown in Eq. (2.1) (Hoener et al., 1992).

$$\left(\frac{r+15}{r}\right)^3 - 1 = \frac{27.5}{W} \tag{2.1}$$

The reverse micelle technique of microemulsion has been used to prepare II-VI core and core/shell QDs, such as cadmium sulfide (CdS) (Colvin et al., 1992), zinc sulfide-doped cadmium sulfide- manganese (CdS:Mn/ZnS) (Yang & Holloway, 2003; Yang et al., 2004; Yang & Holloway, 2004; Yang et al., 2005), CdSe-doped zinc sulfide (ZnS/CdSe) (Kortan et al., 1990), zinc selenide-doped CdSe (CdSe/ZnSe) (Hoener et al., 1992), ZnSe (Reiss et al., 2004) and IV-VI QDs (Ogawa et al., 1997). It is possible to control the size of the QDs using this method by changing the molar ratio of water to surfactant. In addition, the QDs size distribution is narrow compared to the sol-gel method. However, QDs produced by microemulsion shows low yield and present of impurities and defects (Bera et al., 2010).

Another significant wet-chemical method is call hot-solution decomposition process which involve high synthesis temperature. Bawendi and his co-workers, (1993) is the first to intensely discuss on high temperature (~300 °C) pyrolysis of

organometallic compound in 1993 (Murray et al., 1993), which is nowadays among the established method in synthesizing QDs (Hamizi & Johan, 2010). This method required a mixture of precursors solutions of group II [i.e. alkyl (Murray et al., 1993), acetate (Qu et al., 2001), carbonate (Qu et al., 2001) and oxides (Qu et al., 2001; Qu & Peng, 2002) and VI [i.e. phosphene or bis(trimethyl-silyl)] elements by simultaneous injection of group II precursor solution into group VI precursor solution under a rapid stirring condition (Bera et al., 2010; Murray et al., 1993; Hamizi & Johan, 2010). The coordinating solvent such as trioctyl-phosphine oxide (TOPO), trioctyl-phosphine (TOP) (Murray et al., 1993) and oleic acid (Zhengtao et al, 2005; Hamizi & Johan, 2010) are add in the process of preparing precursors solution which is aim to produce well-dispersed QDs, increases surface passivation, and provides an adsorption barrier to slow the growth of the QDs (Bera et al., 2010). As a result, homogeneous nucleation and slow subsequent growth of QDs through 'Ostwald ripening' can be achieves. In Ostwald ripening, smaller sizes QDs that possesses higher free energy lose it mass to larger QDs, and gradually disappear. The final size of the QDs is mainly controlled by the reaction time and temperature (Bera et al., 2010; Hamizi & Johan, 2010).

This method is widely used in synthesizing II-VI (Lee et al., 2006; Bae et al., 2004; Hines & Sionnest, 1998; Yu et al., 2003; Chen et al., 2005), IV-VI (Bakueva et al., 2003) and III-V QDs (Battaglia & Peng, 2002). This method promises a sufficient thermal energy to anneal defects and results in monodispersed QDs (Bera et al., 2010). A series of QDs size can be collect at different time interval from the same precursor bath since growth of the particles is relatively slow using this method (Hamizi & Johan, 2010). Moreover, large amount of QDs can be obtain using this methods (Bae et al., 2008), beside can also be use to produce QDs alloy (Zhong et al., 2003). However, the toxicity of some organometallic compound use in this method essentially needs a great

precaution while handling the compound (Bera et al., 2010). Table 2.1 shows the chronological summary of various QDs synthesized using hot solution decomposition method with vary in chemical precursor and synthesis parameter.

QDs can also grow in water by applying sonic waves or microwaves to the water bath containing a mixture of precursor. The precursor and the water molecules will be separate by the energy from these waves leading to a growth of QDs (Zhu et al., 2000; Qian et al., 2005; Bera et al., 2010).

QDs in the size range of 1 - 5 nm are reported synthesized using the ultrasound waves. Ultrasound wave trigger the formation, growth and implosive collapse of bubbles in a liquid to produce QDs (Zhu et al., 2000). An acoustic cavitation induced a localized hotspot through adiabatic compression within the gas inside the collapsing bubble, enabling the reactions that form QDs (Zhu et al., 2000; Bera et al., 2010).

Table 2.1: Chronological summary of hot-solution decomposition methods of various size QDs

Year	QDs	Precursors	Process parameter	Particles size (nm)	Refereances
1990	GaAs	$GaCl_3$, $(TMS)_3As$ in Quinoline	240 °C for 3days; flame anneal at 450°C	2. 4	Olshavsky et al., 1990
1990	ZnS, ZnSe, CdS, CdSe, CdTe, HgTe	$M(ER)_2$; R: n-butyl phenyl; E: S, Se, Te; M: Cd, Zn, Hg and/or phosphine complexes; Co.Sol.: DEPE	DEPE and $M(ER)_2$ reacted, (Temp.range: 250–300 °C)	2.5–5	Brennan et al., 1990
1993 -1998	CdS, CdSe, CdTe	Me_2Cd, silylchalconides, Phosphine chalconides; Co.sol: TOPO & TOP/TBP	300–350 °C at 1 atm at Ar (TOPO degassing); 230–260 °C (growth temp.)	1.2–11.5	Murray et al., 1993; Katari et al., 1994; Peng et al., 1998

Year	QDs	Precursors	Process parameter	Particles size (nm)	Refereances
1994	GaAs	$GaCl_3$/ GaI_3, diglyme, As, toluene, Na-K alloy	As, Na-K alloy mixture refluxed to 100 °C in Ar for 2 days; $GaCl_3$/GaI_3 diglyme mixture added, heated from 0°C to RT to 111 °C for 2 days	6 -10	Kher & Welss, 1994
1995	InP, GaP, $GaInP_2$	Mixture of chloroindium/ gallium oxalate ($GaCl_3$ for GaP) and (TMS)3P in CH_3CN ; Co.sol: TOPO & TOP	270–360 °C at airless condition for 3 days; QDs dispersed in methanol	2.6–4.6 (InP), 3 (GaP), 6.5 (GaInP2)	Micic et al., 1995
1996	InP, InAs	InCl3, TOPO, $(TMS)_3P$/$(TMS)_3As$	$InCl_3$ & TOPO heat at 100 °C for 12 h, $(TMS)_3P$ added, after 3hr heated to 265 °C for 6 days	2-6	Guzelian et al., 1996 (a) ; Guzelian et al., 1996 (b)

Year	QDs	Precursors	Process parameter	Particles size (nm)	Refereances
1996	CdSe/ZnS	Me_2Cd,Me_2 Zn, Se, $(TMS)_2S$, Co.sol: TOPO, TOP	Single step synthesis Core: 350 °C at 1 atm at Ar, growth: 310 °C Shell: 300°C	2.7-4	Hines & Sionnest, 1996
1997	CdSe/ZnS	Me_2Cd, Me_2 Zn, Se, $(TMS)_2S$, Co.sol: TOPO, TOP	Two step synthesis (airless) Core growth: 290–300 °C Shell growth: 140 °C for 2.3 nm & 220°C for 5.5 nm	2.3–5.5	Dabbousi et al., 1997
1997	CdSe/CdS	Me_2Cd, Se, $(TMS)_2S$, Co.sol: TOPO, TBP	Two step process: Core: 300 °C; Shell: 100 °C	2.5-4	Peng et al., 1998
1998	ZnSe	Me_2Zn, Se, HDA, TOP	HDA dried and degassed at 150°C for hrs in vacuum and heated to 310 °C at 1 atm in Ar; Core growth with Zn & Se precursor at 270 °C.	4.3–6	Hines & Sionnest, 1998

Year	QDs	Precursors	Process parameter	Particles size (nm)	Refereances
1996–1999	InAs/InP InAs/CdSe	$(TMS)_3As$, Indium (III)chloride, TOP $(TMS)_3P$, Me_2Cd; TBPSe	Two-step Process (airless) Core growth: 260 °C; Shell: dropwise addition; 260 °C	2.5–6 (InAs); 1.7 (core/shell)	Core (Peng et al., 1998; Guzelian et al., 1996) Coore/shell (Cao & Banin, 1999)
2000	CdSe	Me_2Cd, Se, TBP, TOPO, HPA	TOPO (+HPA 1.5–3 wt%) degassed at 360 °C (or 310 °C, 280 °C); Core growth: 300 °C (or 280 °C or 250 °C)	~6	Peng et al., 2000; Manna et al., 2000
2001	ZnSe:Mn	Me_2Mn, Et_2Zn, TOP, Se, HDA	Dimethyl Mn, TOP, Se, Diethyl Zn mixture added to HDA at310 °C in N_2. Growth: 240–300 °C	2.7–6.3	Norris et al., 2001

Year	QDs	Precursors	Process parameter	Particles size (nm)	Refereances
2001-2003	CdSe/ZnS	Me_2Cd, Se, TOP, TOPO, HDA, $(TMS)_2S$, Me_2Zn	Two Step: Core: reaction & growth: 270–310 °C; Shell: slow addition of Zn & S precursor at 180–220 °C	4.5–5	Talapin et al., 2001; Hikmet et al., 2003
2001	CdSe	Scheme 1: $Cd(Ac)_2$, SA/ TOPO; 2: $Cd(Ac)_2$, SA; 3: $CdCO_3$, SA/TOPO; 4: $CdCO_3$, LA/TOPO; 5: CdO, SA/TOPO; 6: $Cd(Ac)_2$, tech TOPO; 7: CdO, TDPA/TOPO	Solvent & Cd-precursor heated to 250– 360 °C at Ar; TOP-Se or TBP-Se injected; Growth temp: 200–320 °C (if DDA involve, temp: ~220 °C	2–25	Qu et al., 2001

Year	QDs	Precursors	Process parameter	Particles size (nm)	Refereances
2001	CdS, CdSe, CdTe	CdO, TOPO, HPA/TDPA, S, Se, Te & TOP	One pot: CdO, HPA/TDPA heated 300 °C; Core with chalconide precursor: reaction: 270 °C, and growth 250 °C	2–8	Peng & Peng, 2001
2002	CdSe	CdO, Se, TOPO, TBP, HDA, ODA, SA	CdO & SA, heated to 150 °C in Ar; after CdO dissolution, cool to RT; TOPO and HAD added & heated to 320 °C in Ar; TBP-Se added, Growth 290 °C		Qu & Peng, 2002
2003	PbS	PbO, OA, $(TMS)_2S$, TOP	PbO dissolved in oleic acid at 150 °C in Ar; (TMS)2S & TOP injected	5	Bakueva et al., 2003

Year	QDs	Precursors	Process parameter	Particles size (nm)	Refereances
2003	CdSeS	CdO, OA, TOA, Se, S, TOP	CdO+ OA+TOA heated at 300 °C in N2, TOP-S, TOP-Se injected	~5	Jang et al., 2003
2005	PbSe	Pb-acetate trihydrate, OA, Se, TOP	Single Step: Pb acetate + Co.sol degassed at 100–120 °C at 300–500 mTorr for 2h; reaction and growth: 140 °C	5	Coe-Sullivan et al., 2005
2006	CdSe	CdO, OA, TOA, C_8SH or $C_{18}SH$	CdO + OA + TOA heated at 300 °C; TOA + C_8SH or $C_{18}SH$ injected	3-6	Shinae et al., 2006
2005-2011	CdSe	CdO, Se, OA, paraffin oil	Cd solution prepared by mixing CdO, OA & paraffin oil and heat to 160 ºC. Se solution prepared by dissolving Se in paraffin oil at 220 ºC. Cd solution injected to Se solution at 220 ºC	8-10	Deng et al., 2005; Hamizi & Johan, 2010

Hydrothermal synthesis approaches (Yang et al., 2008; Xie et al., 1996) and similar approach (Rogach et al., 1996) have been used to synthesis QDs. This synthesis approach involved the controlled of pressure and temperature during the crystallizations of aqueous inorganic salts. Lowering the temperature and/or pressure will generally caused the solubility of inorganic salts to dropped, results in formation of crystal precipitates (Yang et al., 2008; Xie et al., 1996). Tailored reactants, temperature, pressure, reaction and aging time can produce various sizes and shapes of QDs (Bera et al., 2010).

Vapor-phase methods are one or the bottom-up methods in producing QDs beside wet-chemical method. These methods begin with process of layers are grown in an atom-by-atom. Consequently, self-assembly of QDs occurs on a substrate without any patterning (Leonard et al., 1993; Swihart, 2003). Indium gallium arsenide (InGaAs) and aluminum indium arsenide (AlInAs) QDs are successfully synthesized using this vapor-phase method (Lobo & Leon, 1998). Despite produced QDs in inhomogeneous sizes, this synthesis approach effectively produced QDs arrays without template (Bera et al., 2010).

2.3 Materials in QDs

History of QDs begins when it was first discovered in glass crystals by Russian physicists, Ekimov and Onushchenko (1981) at early 1980`s (Ekimov & Onushchenko, 1981). Efficient advancement in the science and technology of QDs was driven after 1984, when Brus (1984) derived a relationship of size and bandgap for QD by applying a particle in a sphere model approximation to the wave function for bulk semiconductors (Brus, 1984; Brus 1986). However, it took nearly a decade for a new

encouragement in QD research until the successful synthesis of colloidal CdX (X = S, Se, Te) QDs with size-tunable band-edge absorption and emissions by Murray et al. (1993) (Murray et al., 1993). To this date, CdX is the most investigated QDs owing to it excellent optical and electrochemical properties. Realized of it high potential in biological applications, the toxicity of Cd ion in CdX was paid more and more attention (Bera et al., 2010).

For traditional QDs, Cd is the key element for their composition. However, major drawback to Cd based QDs potential in applications is the leaking of Cd ions which are culpits to the cytotoxicity problem. This is the main problem in it future in applications to cellular or in vivo study. Due to high demand in biocompatible QDs, the emphasis has shift toward the fabrication of Cd-free QDs such as silicon QDs (Si QDs), carbon dots (C-dots), graphene QDs (GQDs), Ag_2Se, Ag_2S, InP and $CuInS_2/ZnS$. Some of them are not new emerging member, such as Si QDs, which appeared even as early as 1990`s. In addition, this Cd free QDs reported to possesses excellent properties which promise a wide applications as luminescent probes for biosensing and bioimaging (Bera et al., 2010).

Si has been known to have indirect semiconductor band gap and poor optical properties for a long time. It was until the 1990`s when efficient light emission from Si was reported by Canham (Canham, 1990) and a year later, Lehman and Gosele (1991) proposed the explanations on the features of porous Si absorption spectra by using quantum confinement (Lehman & Gosele, 1991). This emerged the interest of researcher on Si QDs. There are three discrete photoluminescence bands for Si QDs, which is in the infrared, red and blue light range. The main advantage of Si QDs is their good biocompatibility. Si QDs were reported to be at least ten times safer than Cd-based

QDs under UV irradiation (Fujioka et al., 2008). Moreover, Canham (2007) proposed utilize of the nanoscale Si as a food additive (Canham, 2007). Till present, numerous methods have been reported to produce colloidally and optically stable, water-dispersible Si QDs, incorporating a range of bottom–up and top–down approaches (Bruhn, 2012). However, a main obstacle in bioimaging applications is their oxidative degradation in the biological environment. For a Si QDs in solution phase, surface modification is necessary. Erogbogbo et al. (2011) prepared Si QDs using a nanoparticle synthesis, surface functionalization, polyetylynglicol (PEG)ylated micelle encapsulation, and bioconjugation process. This surface modification process are reported to successfully produced Si QDs that has a high potentials in multiple cancer-related in vivo applications, including tumor vasculature targeting, sentinel lymph node mapping, and multicolor NIR imaging in live mice, which showed great potentials of Si QDs as biocompatible fluorescent probes for both in vitro and in vivo imaging (Erogbogbo et al., 2011).

Carbon dots (C-dots) are a new class of carbon nanomaterials with sizes below 10 nm, which were first reported to be successfully produced during purification of single-walled carbon nanotubes through preparative electrophoresis (Xu et al., 2004). Since the discovery of their outstanding optical property, C-dots have attracted wide attentions and shows great potentials in biological applications. C-dots has a unique optical property of excellent up-converted PL (UCPL) besides a normal or down-converted photoluminescence (PL). This enables the design of high-performance, complex catalyst systems based on C-dots for efficient exploitation of the full spectrum of sunlight (Shen et al., 2012; Cao et al., 2007; Li et al., 2012; Ming et al., 2012). In addition, C-dots can exhibit PL emission in the near infrared (NIR) spectral region under NIR light excitation, which is particularly significant for in vivo bio-

nanotechnology due to its low auto-fluorescence and high tissue transparency in the NIR region (Lim et al., 2006; Tang et al., 2012). Apart from its strong fluorescence, C-dots also shows distinct properties such as electrochemical luminescence (Ding et al., 2002; Zhu et al., 2009; Zhou et al., 2010 (a)), photo-induced electron transfer property (Zhang et al, 2012; Wang et al, 2009), photo-catalysis (Li et al., 2012), optoelectronics (Ponomarenko et al., 2008; Girit et al., 2009), which all extend their applications in various areas. Graphene QDs (GQDs) are one of the C-dots materials which have also attracted a lot of interest from researchers over the past few decades because of their fascinating optical and electronic properties. Graphene is a zero band gap material in principle, but the band gap of graphene can be tuned from 0 eV to that of benzene by varying their sizes (Yan et al., 2010; Shen et al., 2012). The one dimension graphene sheets could be converted into zero dimension GQDs, which assume to possess numerous novel chemical and physical properties due to the apparent quantum confinement and edge effects (Zhou et al., 2012 (b); Pan et al., 2010). Although GQDs are considered as a member of C-dot family, GQDs shows several distinctions features compared to general C-dots (Li et al., 2013). The C-dots are either amorphous or crystalline, while GQDs possess graphene lattices inside the dots, in spite of the dot sizes (Baker & Baker, 2010). Additionally, luminescent C-dots contain discrete, quasi-spherical carbon nanoparticles with sizes below 10 nm, while GQDs are always defined as the graphene sheets with lateral dimensions than 100 nm in either single, double, or a few (3 to <10) layers (Shen et al., 2012; Ponomarenko et al., 2008). In general, the average sizes of GQDs are mostly below 10 nm, and the largest diameter of GQDs reported is 60 nm, which is reliant on the preparation methods (Liu et al., 2011). In addition, GQDs shows properties of photoluminescence, good electron mobility and chemical stability, electrochemical luminescence, and photocatalyst which contributed to the fabrication of numerous sensors and bioimaging (Li et al., 2013; Shen et al.,

2012). Beside Si QDs, C-dots and GQDs, other kinds of Cd-free QDs have also been intensely developed due to their good biocompatibility and excellent optical properties. Examples of this others Cd-free QDs is InP (Yong et al., 2009), InP/ZnS (Tamang et al., 2011), $CuInS_2$/ZnS (Chen et al., 2013; Li et al., 2009), Ag_2Se (Gu et al., 2012), Ag_2S (Hong et al., 2012) which shows outstanding potentials in biological imaging applications (Chen et al., 2013; Li et al., 2009).

As an alternative to QDs, fluorescent metal nanoclusters which known to possess very small size, superior biocompatibility, and excellent photostability, have become a new class of fluorescent labels for biological applications. Among them, gold (Au) and silver (Ag) nanoclusters attract much more attentions. Initially, little attention was paid to this metal nanocluster due to extremely low quantum yield (QY) of 10^{-10} observed in PL from the noble metals. However, the enhancement on the QY up to 10^{-3} to 10^{-1} have been attracted interest among researchers (Mooradian, 1969). Until now, a lot of Au and Ag NCs stabilized with different scaffolds (protein, peptide, and oligonucleotide) have been developed and applied for the detection of thiol compounds (Huang et al., 2011), metal ions (Su et al., 2010; Lan et al., 2010), protein (Sharma et al., 2011; Li et al., 2012), deoxyribonucleic acid (DNA) (Yeh et al., 2012), ribonucleic acid (RNA) (Dong et al., 2012) as well as intracellular and in vivo bioimaging. Dickson and co-workers (2009) successfully transferred poly (acrylic acid)-stabilized Ag NCs (PA-SCs) to anti-actin Ab/C12 and anti-α-tubulin/C12 conjugates to get fluorogenic silver cluster biolabels for cell surface labeling (Yu et al., 2009). Wang et al. (2013) reported fluorescent Au NCs could be spontaneously biosynthesized by cancerous cell incubated with micromolar chloroauric acid solutions, a biocompatible molecular Au (III) species, which could not take place in noncancerous cells (Wang et al., 2013). They further realized in vivo self-bioimaging of tumors by subcutaneous injections of

millimolar chloroauric acid solution near xenograft tumors of the nude mouse model of hepatocellular carcinoma or chronic myeloid leukemia. This shows potential of fluorescent metal nanoclusters for in vivo bioimaging (Wang et al., 2013). Specially, DNA-stabilized Ag NCs possess apparent advantage in DNA biosensing because of the uncomplicated assembly of DNA sequence. Werner and colleagues designed a nanocluster beacon to detect a DNA series related to the human Braf oncogene based on an interesting phenomenon that the red fluorescence of DNA-stabilized Ag NCs could be improved 500-fold when placed in proximity to guanine-rich DNA sequences (Yeh et al., 2010).

2.4 Doping in QDs

Doping in QDs by intentionally incorporating impurities into the colloidal semiconductor is a noteworthy approach to modifying the electronic, optical and magnetic properties of the QDs (Stowell et al., 2003; Norris et al., 2008), especially for technological applications such as optoelectronic, magnetic, biological and spintronic applications (Bryan & Gamelin, 2005; Norris et al., 2008). These impurities will interrpt the band structures by producing local quantum states that lies inside the band gaps. Significantly, quantum confinement effect in QDs will permits the dopants to be auto-ionized without thermal activation. This auto-ionization takes place when quantum confinement energy exceeds Coulombic interaction between carrier (hole or electron) and impurity (n-type or p-type) (Bera et al., 2010).

Various transition elements such as, chromium (Cr) (Yu et al., 2007), manganese (Mn)(Beaulac et al., 2009), iron (Fe) (Rajabi et al., 2013), cobalt (Co) (Radovanovic & Gamelin, 2001), cooper (Cu) (Stouwda et al., 2009) and silver (Ag)

(Sethi et al., 2009), and other elements, such as, phosphorus (P) (Hao et al., 2009), boron (B) (Fan et al., 2014), sodium (Na) (Orlinskii et al., 2004) and litium (Li) (Orlinskii et al., 2004) were doped into QDs, for various applications. Optical properties of QDs can be tailor by changing the amounts (Yang et al., 2005) and the positions (Yang et al., 2006) of dopants in the QDs. In addition, doping QDs with transition metal ions such as Mn^{2+} induces diluted magnetic semiconductor phenomenon that can be useful in spintronic devices due to the effect of giant Zeeman splitting, which results from the exchange interaction between the transition metal ions and the electronic states of the QDs host (Yu et al., 2010; Efros et al., 2001).

Doped Mn into II-VI QDs has captured huge attention of scientists for more than a decade because of it good potential in improves the in solar cell and spintronic devices efficiency (Huynh et al., 2002; Awschalom & Kikkawa, 1999). Mn possesses paramagnetic properties that will provides a means of coupling the optical and magnetic properties of these materials via sp-d inter-band exchange interaction. Mn^{2+} acts as a paramagnetic centre (S=5/2) which will substitutes cation from group II cation in the semiconductor lattice (Oluwafemi et al., 2010). The interaction between the semiconductor host and the Mn, creates a new class of materials which will arise interesting magnetic and optical properties that are not possesses by either bulk diluted magnetic semiconductors (DMS) or pure QDs (Levy et al., 1996; Miculec et al., 2000; Norris et al., 2001). Mn reported to has been successfully doped into CdS, ZnS and ZnSe QDs that exhibits zinc-blende structure (Levy et al., 1996; Norris et al., 2001; Li et al., 2006). Despite, Mn doping into CdSe QDs has been highly restricted (Erwin et al., 2005; Kwak et al., 2007) due to intrinsic properties of CdSe, Mn adsorption binding energy and parasitic binding of Mn by strong surfactants (Oluwafemi et al., 2010).

Mikulec was first reported to has been successfully doped Mn into CdSe QDs using custom designed precursor via a high temperature pyrolysis (Mikulec et al., 2000). In this reaction, organometallic decomposition of $Mn_2(\mu\text{-}SeMe)_2(CO)_8$, trioctylphosphine selenides (TOPSe) and dimethyl cadmium ($CdMe_2$) in TOPO was use to produce zinc blende Mn-doped CdSe QDs. A number of attempts to use simpler precursors containing only manganese were not succeed (Oluwafemi et al., 2010).

Zinc blende CdSe was suggested to have higher banding energy of the {001} facet compare to any facets in wurtzite CdSe . This theory was proposed by Erwin et al., (1996) which is based on the density-functional theory (Erwin et al., 2005; Perdew et al., 1996). Thus, they suggested that it would be possible to dope zinc blende CdSe QDs with Mn compare to wurtzite CdSe QDs. Recently based on the Erwin et al. proposition, Kwak et al. successfully synthesized Mn-doped zinc-blende CdSe QDs via an inverse micelle technique and concluded that wurtzite CdSe cannot be doped with Mn due to self purification (Kwak et al., 2007). On the other hand, Erwin et al., try to solve this restriction and reported a synthesis of Mn-doped wurtzite CdSe by using a weak binding surfactant in 2005 (Erwin et al., 2005). However this reaction involves severe conditions such as injection of hazardous and toxic metal-alkyls. In addition, these metal-alkyls are easily volatile compound having a low boiling point, explosive at elevated temperature, and pyrophoric. Therefore this synthesis process requires standard airless techniques. Hence, it is agreeable that this method is for a research setting but undesirable for commercial exploitation (Oluwafemi et al., 2010).

2.5 Quantum Confinement Effect

In the early 1980s, Ekimov and Onushchenko (1981) at the Ioffe Physical-Technical Institute in St. Petersburg detected the unusual optical spectra from glass samples containing CdS and CdSe, this was first hints that quantum confinement in zero-dimentional was possible (Ekimov & Onushchenko, 1981). The samples were exposed to high temperatures which induced precipitates of the nanocrystallites on the glass. The quantum confinement of electrons in these crystallites shows the uncommon optical behaviour (Ekimov & Onushchenko, 1981; Reed, 1993).

For better understanding about quantum confinement effect, imagine an electron trapped in a box. Quantum mechanics states that the electron has wave properties, like the ripples on water or the vibrations of a violin string. Similar to a violin string tied down at both ends, the electron wave is bounded by the walls of the box. The wavelength of the string's vibrations (or the electron's) must fit within these confines. In the case of the violin string, the point at which it is tied down changes as the violinist's finger slides up the fingerboard. The length of the allowed waveform shortens, and the frequency of the string's vibrations increases, as does that of all its harmonic overtones. If the size of an electron's confining box is made smaller, the electron's lowest energy level (the analogue of the fundamental pitch of the violin) will increase (Reed, 1993).

For semiconductor nanocrystallites, the fundamental "pitch" is the threshold energy for optical absorption, and the harmonic overtones correspond to new absorption features at higher energies. In a vacuum, the effects of confinement will begin to occur when the electron is trapped in a volume about 10 Å across. This size implies an

electron wavelength of 20 Å and therefore energy of about one fortieth of an electron volt (eV). In this case, semiconductor physics is an aid for the nanotechnologist. The wavelength of an electron depends on its energy and it's mass. For a given wavelength, the smaller the mass, the larger the energy, and the easier it is to observe the energy shift which causes confinement. The electrostatic potentials of the atoms in the crystalline lattice are superimposed to provide a medium in which the electron waves propagate with less inertia than they do in the free space. The "effective mass" of the electron is thus less than its actual mass (Takagahara & Takeda, 1992; Reed, 1993).

In GaAs the effective mass is about 7 % of its effective mass in a vacuum, whereas the effective mass is 14 % in a Silicon. Consequently, quantum confinement in semiconductors occurs in a volume about 100 Å. The threshold of optical absorption for nanocrystallites shifts to higher energies, away from the red end of the spectrum, as the crystallite becomes smaller. This effect appears most significantly in CdSe clusters, which is the progression from deep red to orange to yellow (Reed, 1993).

Quantum confinement generally results in a band gap widening as a function of size of the QDs decrement. The band gap in a material is the energy necessary to form an electron and a hole at rest (i.e., with zero kinetic energy) at a distance far enough apart that their Coulombic attraction is negligible. If one carrier approaches the other, they might form a bound electron-hole pair such as exciton, which energy is a few meV lower than the band gap. This exciton behaves similar to a hydrogen atom, except that a hole, not a proton, forms the nucleus. Apparently, the mass of a hole is much smaller than that of a proton, which affects the solutions to the Schrödinger wave equation. The distance between the electron and hole is called the exciton Bohr radius (r_B). If m_e and m_h are the effective masses of electrons and holes, respectively, the exciton Bohr radius

for bulk semiconductor can be expressed by Eq. (2.2), where ε, ħ, and e are the optical dielectric constant, reduced Planck's constant and the charge of an electron, respectively (Bera et al., 2010).

$$r_B = \frac{\hbar^2 \varepsilon}{e^2} \left(\frac{1}{m_e} + \frac{1}{m_h} \right) \tag{2.2}$$

If the radius (r_{dot}) of a QDs approaches r_B (i.e., $r_{dot} \approx r_B$, or $r_{dot} < r_B$), the motion of the electrons and holes are confined spatially to dimension of the QDs which causes an increase of the excitonic transition energy and the shows blue shift in the QDs band gap and luminescence. The exciton Bohr radius is a threshold value, and the confinement effect becomes significant when the QDs radius is smaller. For small QDs, the exciton binding energy and biexciton binding energy (exciton-exciton interaction energy) is much larger that for bulk materials (Klimov, 2006). Note that for a material with a relatively higher ε or smaller m_e and m_h, the r_B is larger. Two detailed theoretical approaches are used to intensely studies the exciton properties, which is the effective mass approximation (EMA) model and linear combination of atomic orbital (LCAO) theory (Bera et al., 2010).

This approach, based on the 'Particle-in-Box Model', is typycally used model to predict quantum confinement. It was first proposed by Efros and Efros (Efros & Efros, 1982) in 1982 and later modified by Brus (Brus, 1983). It believes that a particle in a potential well with an infinite potential barrier at the particle boundary. For a particle free to assume any position in the box the relationship between its energy (E) and wave vector (ƙ) is given by Eq. (2.3) where m* is a constant (effective mass) (Brus, 1983; Bera et al., 2010).

$$E = \frac{\hbar^2 \mathrm{k}^2}{2\, m^*} \tag{2.3}$$

In the EMA model, this relationship shows in Eq (2.3) and assumed to hold for an electron or hole in the semiconductor, therefore the energy band is parabolic near the band-edge. The shift of band gap energy (ΔEg) due to confinement of the exciton in a QDs with a diameter r_{dot} can be expressed as in Eq. (2.4), where, μ is the reduced mass of an electron-hole pair and E^*_{Ry} is Rydberg energy (Brus, 1983; Bera et al., 2010).

$$\Delta E = \frac{\hbar^2 \pi^2}{2\mu r_{dot}^2} - \frac{1.8e^2}{\varepsilon r_{dot}} = \frac{\hbar^2 \pi^2}{2r_{dot}^2}\left(\frac{1}{m_e} + \frac{1}{m_h}\right) - \frac{1.7e^2}{\varepsilon r_{dot}} - 0.248E_{Ry}^* \tag{2.4}$$

The first expression of the Eq (2.4) represents a relation between 'particle-in-a-box' quantum localization energy or confinement energy and the radius of the QDs (r_{dot}) whereas the second expression shows the Columbic interaction energy with a r_{dot}^{-1} dependence. The Rydberg energy term is size independent and is usually insignificant and negligible, except for semiconductors with small dielectric constant (Wang & Herron, 1991). Based on Eq. (2.4), the first excitonic transition (i.e., the band-gap) increases as the r_{dot} decreases (quantum localization term shifts to higher energy with lower r_{dot} value (r_{dot}^{-2}) and Columbic terms shifts excited electronic state to lower value (r_{dot}^{-1}). However, the EMA model breaks down in the small QDs regime (Murray et al., 1993; Wang & Herron, 1991) because the *E-k* relationship can no longer be approximated as parabolic. (Bera et al., 2010).

A model based on a linear combination of atomic orbitals–molecular orbitals (LCAO-MO) offers more detailed basis for predicting the evolution of the electronic structure of clusters from atoms and/or molecules to QDs to bulk materials, and

predicting the dependence of band gap on size of the crystals. As the number of atoms increase, the discrete energy band structure change from large steps to small energy steps, i.e., to a more continuous energy band. The occupied (bonding) molecular orbital quantum states (equivalent to the valence band) are called the highest occupied molecular orbital (HOMO) levels. The unoccupied anti-bonding orbitals (equivalent to the conduction band) are called the lowest unoccupied molecular orbital (LUMO) levels. The energy difference between the top of the HOMO and bottom of the LUMO (equal to the band-gap) increases and the bands split into discrete energy levels reduced mixing of atomic orbitals for a small number of atoms. Therefore, the small size of the QDs results in quantized electronic band structures intermediate between the atomic/molecular and bulk crystalline molecular orbitals (Bera et al., 2010).

Compared to the effective mass approximation, the LCAO-MO model provides a methodology to calculate the electronic structure of much smaller QDs. In contrast, this method cannot be used to calculate the energy levels of large QDs due to mathematical complexity and limitations of the computing systems. Nevertheless, the degree of quantum confinement is determined by the ratio of the radius of a QDs to bulk excitonic Bohr radius (r_B). At crystal sizes greater than the excitonic Bohr diameter ($2r_B$), semiconductor crystals exhibit translational motion confinement of the fully coupled exciton due to a strong Coulombic interaction between the electron and holes, i.e., exhibits singleparticle confinement behavior (sometimes called the strong confinement regime). In the intermediate size range ($R \leq r_B$), the transition energies of photoexcited carriers in the crystal are determined by the relative strengths of the kinetic energy of confinement and the electron-hole interaction (Bera et al., 2010).

Band-gap of QDs can be determined by electrochemical measurement using Qdots films. Cyclic voltametry (CV) are often employed (Ogawa et al., 1997; Inamdar et al., 2008) to determine the oxidation and reduction potential of the film of QDs to be measured using a standard three-electrode cell. CV is a dynamic electrochemical method in which current-potential curves are traced at a pre-defined scan rates. QDs coated gold plate, platinum wire or indium tin oxide film on glass substrates are often used as working electrodes and platinum electrode acts as a counter electrode. The cell potential is generally normalized to reference electrode using Fc/Fc^{+} couple (Bera et al., 2010).

2.6 Synthesis of Mn-doped CdSe QDs

Mn-doped CdSe QDs can be obtained from a variety of Cd and Mn precursors, including Cd and Mn salts, combined with a Se precursor, which is usually prepared from Se powder dissolved in trioctylphosphine (TOP) or tributylphosphine (TBP) (Peng et al., 2001; Yu et al., 2003; Qu et al., 2001; Yordanov et al., 2005). The first hot-matrix method used to synthesis Mn-doped CdSe QDs was from Cadmium Oxide (CdO) (Peng et al., 2001) which utilized Cd (II) alkylphosphonate salts. Various fatty acids (such as stearic acid), applied as ligands for Cd, yield relatively faster particle growth (Yu et al., 2003; Qu et al., 2001; Yordanov & Minkova, 2005). Although the fatty acids are compatible with Cd precursors, they are most suited for growth of larger QDs (4 – 5nm). The Cd precursor is typically dissolved in stearic acid (SA) at moderate temperatures (100 – 150 °C), converting the precursor to Cd (II) stearate. Complex solvent systems of mixed amphiphiles as ligands (Han et al., 2006) usually produce QDs possessing high quantum yields of emission and monodisperse sizes (Yordanov & Minkova, 2005).

However, the effects of each ligand could not be easily distinguished. For this purpose, one should first investigate various mixtures of the precursor with non-polar and non-coordinating solvents such as octadecene (Yu et al., 2003) and liquid paraffin (Deng et al., 2005; Yordanov et al., 2005). As coordinating solvents, they form complexes with Cd (II), which develop a capping layer on the nanocrystals' surface (e.g. hexadecylamine or trioctylphosphine oxide, TOPO). Liquid paraffin is defined as a non-coordinating solvent because it is a mixture of saturated hydrocarbons without functional groups capable of coordination with Cd (II). It is possible that the coordinating solvents may alter the reactivity of the Cd precursor by coordinating the Cd (II) ions to form the respective complexes. The altered reactivity of Cd (II) precursors and the capping of nanocrystals with coordinating molecules may result in different rates of nanocrystal nucleation and growth in different (coordinating and non-coordinating) solvents (Yordanov et al., 2005).

Peng's group (Yu et al., 2003) noticed that the concentration of oleic acid in octadecene strongly affects the so-called phosphine-free synthesis of Cadmium Sulfide (CdS) nanocrystals. However, stearic acid is expected to be more stable than oleic acid, because of the lack of double bonds, which could be oxidized easily. Stearic acid was found to be better than oleic acid for the synthesis of CdSe QDs in liquid paraffin. Moreover, the growth kinetics of CdSe QDs was found to be different in paraffin with either stearic or oleic acid (Yordanov et al., 2005). Embden and Mulvaney (2005) studied the synthesis of CdSe QDs from Cadmium Oleate and trioctylphosphine selenide (TOP-Se) in Octadecene (ODE). The CdSe QDs contained another coordinating amphiphile namely: bis-(2,2,4-trimethylpentyl) phosphinic acid (TMPPA), which was injected together with tributylphosphine selenide (TBP-Se). They classified oleic acid as a "ripening agent", because it accelerates the ripening processes. Increasing

its concentration led to the formation of larger particles at lower particle concentration (Embden & Mulvaney, 2005).

A synthetic route for preparing high-quality CdSe QDs in an aqueous solution was reported by Xianfeng Chen's group from Oxford University (Chen et al., 2009). When sodium selenide is used to synthesise CdSe QDs in the presence of 3-MPA, the formation of QDs can only happen slowly during refluxing at certain temperatures (above room temperature). Therefore, 3-MPA can form a dense layer on CdSe QDs and synthesise extremely small CdSe QDs having higher luminescence in aqueous solutions (Chen et al., 2009).

However, CdSe QDs produced by chemical synthesis that using trioctylphosphine (TOP) (Murray et al., 1993) are most common. This is due to the fact that TOP based routes produce high-quality wurtzite CdSe QDs, which are stable in atmosphere. This is negated by the fact that TOP solvent is expensive and not environment-friendly. This leads to the introduction of a new non-TOP based route, which is greener and cost-effective (Deng et al., 2005). Both methods utilize Selenium (Se) and Cadmium Oxide (CdO) powders as starting materials. Cadmium (Cd) is a toxic heavy metal and Se is toxic in excessive amounts (Peng, 2002). Therefore, appropriate precautions should be taken when handling these materials. For example, the experiment should be conducted in a fume hood and the user should wear chemical gloves and a face mask (Gerion et al., 2001).

Non-TOP based route (Inverse Micelle) is the synthesis of CdSe QDs by injecting Cd oleic acid (Cd-OA) or Cd complex into a Se solution without using TOP (Peng et al., 2001). This synthesis route is much greener than TOP based routes because it uses

oleic acid and paraffin oil, which are natural products without toxicity (Yu et al., 2003). Therefore, this method is beneficial for scientific research and industrial sectors. This method produces CdSe QDs with zinc blende structures (Danek et al., 1996). On the other hand, TOP based route also produces CdSe with wurtzite structures (Trindade et al., 2000). This leads to a new investigation since CdSe QDs possess different properties between zinc blende cubic and wurtzite hexagonal structures (Sharma et al., 2003).

2.7 Mechanism in Synthesizing Mn-doped CdSe QDs

The Mn-doped mechanism is tailored from the synthesized of CdSe QDs (Hamizi & Johan, 2010). There are two possible methods in synthesizing the CdSe QDs. The trioctylphosphine (TOP) based method (Murray et al., 1993) and the new convenient and greener non-TOP based route (Deng et al., 2005). Non-TOP based method and TOP based method will be elaborated in Chapter Three of this report. Both methods were using selenium (Se) and cadmium oxide (CdO) powders as part of the starting materials. Cadmium (Cd) is a toxic heavy metal and Se is toxic in too large amounts (Peng, 2002). Therefore, appropriate precautions should be taken when handling them, such as, the experiment should be held in the fume hood and wearing chemical gloves and face mask (Gerion et al., 2001).

Non-TOP based route is the synthesis of CdSe QDs by injection of Cd oleic acid (Cd-OA) or Cd complex into a Se solution without using TOP (Peng et al., 2001). This synthesis route is much greener than TOP based route because it using oleic acid and paraffin oil which both are natural products without toxicity (Yu et al., 2003). This synthesis route is less cost since TOP is too expensive. This will give great a benefit for the scientific research and industrial sectors.

The mechanism in producing CdSe QDs using non-TOP based route involved redox reaction. Eqs. (2.5-2.8) show the possible chemical reactions involved in the formation of CdSe QDs. Eq. (2.5) demonstrates the CdO reacts with oleic acid to generate Cd-OA solution. This reduction process in producing Cd-OA involved the used of paraffin oil as a solvent but it doesn't involved in this chemical reaction (Deng et al., 2005).

$$CdO + Oleic\ acid \xrightarrow{\triangle} Cd\text{-}OA \qquad (2.5)$$

Eq. (2.6) is a process of dissolving Se powder into the paraffin oil and a dehydrogenation reaction to generate H_2Se gas in situ. Under the heating process, Se is reduced to H_2Se gas, while the long alkane chains are oxidized to the long alkene chains. There are three reasons which may play the important roles in the formation of stable homogenous Se solution. The melting point of Se powder is 221 ºC, thus the liquid state of Se can be formed at a temperature of near or above 221 ºC in the paraffin oil. This liquid state then can be well dispersed in the paraffin oil that has long alkane chains. The reaction will produced H_2Se that can be decomposed to Se reversibly at the present temperatures. However, if the temperature were rose to 300 ºC, the H_2Se gas will released immediately. Thus, the moderate temperature is favorable for the formation of Se solution. Eq. (2.7) is a general equation to produce CdSe QDs (Deng et al., 2005).

$$n/4Se + R\text{-}CH_2(CH_2)_nCH_3 \xrightarrow[\text{(Paraffin oil)}]{\triangle} R\text{-}CH_2(CH_2CH{=}CHCH_2)NCH_3 + n/4H_2S \qquad (2.6)$$

$$H_2Se + Cd\text{-}complex \xrightarrow{\triangle} CdSe \qquad (2.7)$$

Eq. (2.8) summarizes the general redox reaction for the formation of CdSe QDs, where Se acts as oxidant and CdSe as the reduction product. While the carbon atom in long alkane chains acts as the reducing agent and the long alkene chains should be the oxidation product (Deng et al., 2005).

$$CdO + Oleic\ acid + Se\ (oxidant) \xrightarrow[\triangle]{} CdSe + Oxided\ products \qquad (2.8)$$

TOP based route is an established CdSe synthesizing method that been used by researchers from all over the world since long time ago. Hundreds and hundreds of papers have already been published based on this route (Deng et al., 2005). However, only little knowledge has been obtained for the mechanism of the formation of the CdSe QDs through this route. In particular, no chemical reaction equations on TOP based route have been discussed in literature. Furthermore, the cost is high because the using of expensively TOP (Yang et al., 2007). TOP is a coordinating solvent for Se that will stabilize the nanoparticles against flocculation during synthesis. After synthesizing the CdSe QDs, TOP will coats the nanoparticles to provide the electronic insulation and passivating of the nanoparticles surface. The cost aspect has to be considered, especially in the larger scale production. In addition, TOP is hazardous, unstable and not environmental friendly solvent (Wang et al., 2009).

Several researches had come up with the theory of CdSe QDs formation in TOP based route based on the study of Electron Diffraction X-Ray (EDX) and FTIR of CdSe QDs (Kotkata et al., 2009). Eq. (2.9) is the possible chemical reaction in producing CdSe QDs by introducing alkylcadmium (Me_2Cd) and trioctylphosphine selenide (TOPSe) precursor into a heated solvent under controlled conditions (Manna et al., 2000).

$$Me_2Cd + TOPSe \longrightarrow CdSe + Byproducts \quad (2.9)$$

2.8 Strain in QDs

Lattice strain or microstrain can be generally defined as the deformation lattice divided by their ideal lengths which can presence in two types which is uniform and un-uniform strain. Uniform strain causes the lattice parameter to expand or contract in an isotropic direction which simply leads to a change in the lattice parameter and shift of peaks. There is no broadening associated with this type of strain. Non-uniform strain generates systematic shifts of atoms from their ideal positions and results in peak broadening. Non-uniform strain is induced by numerous factors such as point defects (i.e. vacancies and site-disorder), plastic deformation and poor crystallinity (Delhez et al., 1993). The atomistic strain in QDs is usually on the order of 10% (Ameen et al., 2014). The electronic band structure is changed by the lattice strain significantly in nano-scale materials (Ameen et al., 2014).

Scherrer (1918) was first to observe that small crystallite size could increases line broadening and derived it's well known Scherrer formula (Scherrer, 1918). Scherrer's formula (Eq. (2.10)) is the commonly use formula to calculate crystallite size (L) using the data extract from XRD spectra (Langford & Wilson, 1978).

$$L = \frac{k\,\lambda}{\beta\,cos\theta} \quad (2.10)$$

Where, k is the Scherrer's constant of the order of unity for normal crystals, taking a value of 0.9 which is specifically for full-width at half maximum (FWHM) of spherical crystals with a cubic symmetry. FWHM of analyzed data was used instead of

integral breadth since it is more precise by taking the consideration of the highly noise diffraction peak. The X-ray wavelength is represented by λ, with a value of 1.5406 Å. β is the full width at half maximum (FWHM) or the broadening of the peak and θ is the Bragg`s diffraction angle (Langford & Wilson, 1978).

Stokes and Wilson (1944) first discovered that strained crystals containing line broadening of a different type compared to the broadening that induced by the small crystallite size. Therefore, size and strain broadening shows difference Bragg`s angle (θ) dependence (Stokes & Wilson, 1944) with derived as Eq. (2.11). Williamson and Hall (1953) proposed a method for deconvolution size and strain broadening by considering at the peak width as a function of 2θ as shown in the equation below (Williamson & Hall, 1953).

$$\beta_o = \beta_i + \beta_r \tag{2.11}$$

$$\beta_r = \beta_c + \beta_s = \frac{k\lambda}{L\ cos\,\theta} + \eta tan\theta \tag{2.12}$$

Where β_o is an observed broadening of the peak, β_i is the broadening by instrument factor, β_r is the broadening induced by crystallite size and strain and β_c is broadening by crystallite size. By rearrange Eq. (2.12), to form a general equation for straight line (Eq. (2.13)) where kλ/L is the intercept of graph line with y-axis and slope of the graph is the strain as illustrated in Figure 2.1.

$$\beta_r\ cos\,\theta\ = \frac{k\lambda}{L} + \eta\, cos\,\theta \tag{2.13}$$

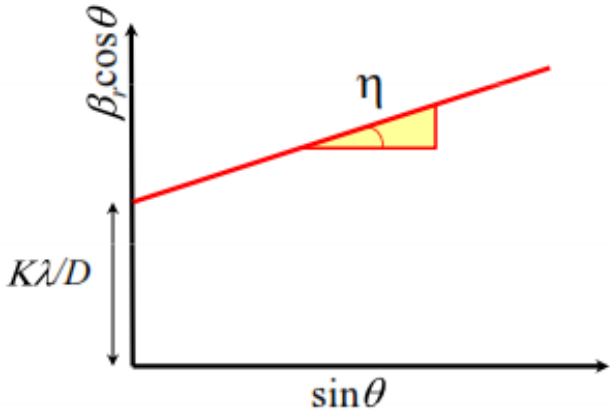

Figure 2.1: The general Williamson-Hall plot

Compared to Williamson-Hall analysis, Lorentzian and Gaussian term in the Thompson-Cox-Hasting pseudo-voigt (TCH) function shows that the size and strain parameters can be extracted from the refined profile parameters. Eq. (2.14) shows the TCH function in Lorentzian (Γ_L) term and Eq. (2.15) shows the TCH function in Gaussian (Γ_G) term (Karen & Woodward, 1998).

$$\Gamma_L = \frac{X}{cos\theta} + Ytan\theta \tag{2.14}$$

$$\Gamma_G = Utan^2\theta + Vtan\theta + W + \frac{P}{cos\theta} \tag{2.15}$$

The Fourier Methods is reported to be the most accurate way of extracting size and strain information is to analyze the entire shape of several reflections in the pattern, ideally higher order reflections of the same type. This method developed by Warren and Averbach (1950) can be done using the step by step procedure as following (Warren & Averbach, 1950):

1. Fit each reflection of interest with a Fourier series.
2. Repeat this procedure for a pattern of a sample which gives no broadening, in order to determine the instrumental contribution to broadening
3. Use these results to deconvolute the sample broadening from the instrumental broadening, via a Stokes Fourier deconvolution.
4. Extract information regarding the size distribution and strain profile by analyzing the theta dependence of the cosine Fourier coefficients (which describe the symmetric broadening)

Compared to Williamson-Hall intergral breadth method, Fourier methods give a distribution of crystallite sizes instead of an average value. In addition, the correction for instrumental broadening is more rigorous when the peak shape is not purely Gaussian or Lorenztian. However, this method prone to error if peak tails are not accurately modeled. This makes it difficult to use when peak overlap is significant. Furthermore, Fourier decomposition is not always very stable (Warren & Averbach, 1950).

Moreover, there are several differences between Fourier and Integral Breadth Methods which is the crystallite size determined from Integral Breadth methods is a volume weighted average (D_V), whereas the Fourier methods return an area weighted average (D_A). By assuming spherical particles all of the same size the sphere diameter (d), it is related to the size by Eq. (2.16), Therefore $D_V = (9/8)D_A$ (Warren & Averbach, 1950).

$$d = (4/3)D_V = (3/2)D_A \qquad (2.16)$$

Double Voigt methods of analyzing peak broadening was first introduced by Langford (1980) and developed by Balzar (1999). This methods gave the similar information that one could obtain from the Fourier methods (Langford, 1980; Balzar, 1999). The double Voigt method proceeds along the following lines where peaks are fitted analytically using a Voigt function (can be extended to Pseudo-voigt and Split Pearson functions), so that the Lorentzian breadth (β_L) and Gaussian breadth (β_G) of each peak can be determined. Then the integral breadths are corrected for instrumental broadening by Eqs. (2.17) and (2.18). Williamson-Hall plots are constructed from for both the Lorentzian and Gaussian peak widths. The crystallite size is extracted from the Lorentzian Williamson-Hall plot and the strain is taken to be a combination of the Lorentzian and Gaussian strain terms (Langford, 1980; Balzar, 1999).

$$\beta_{L(sample)} = \beta_{L(fit)} - \beta_{L(instrument)} \quad (2.17)$$

$$\beta_{G(sample)}^{2} = \beta_{G(fit)}^{2} - \beta_{G(instrument)}^{2} \quad (2.18)$$

.

Double-Voigt method have some advantages compared to the integral Breadth and Fourier methods. Despite of the sensitive to accurate fitting of the peak tails of Lorentzian and Gaussian mixing parameter, this method is more robust than the Fourier methods to the errors associated with peak overlap. Unlike the Williamson-Hall approach Double Voigt methods can be used when the peak shape is neither pure Lorentzian nor pure Gaussian. In addition, crystallite size distributions can be obtained (Balzar, 1999).

CHAPTER THREE

METHODOLOGY

This chapter describes the materials used to synthesize Mn-doped CdSe QDs via inverse Micelle technique and details of the synthesis process, followed by the characterization studies that have been done using several equipments.

3.1 Materials

Mn-doped CdSe QDs were prepared using cadmium oxide (CdO) powder, Manganese (Mn) acetate, selenium (Se) powder, paraffin oil and oleic acid. Methanol and distilled water were used in the final stage of filtering and washing the final products. Details of the chemical used were tabulated in Table 3.1.

Table 3.1: Details of chemical materials used in synthesis of Mn-doped CdSe QDs samples

Chemical	Brand	Chemical formula	Molecular weight (g/mol)	Density (g/ml)
Cadmium oxide (≥ 99.00 %)	Sigma-Aldrich®	CdO	128.41	-
Selenium (≥ 99.99 %)	Sigma-Aldrich®	Se	78.96	-
Manganese (II) acetate (98%)	Sigma-Aldrich®	$(CH_3CO_2)_2Mn$	173.03	1.59
Paraffin oil	Sigma-Aldrich®	C_nH_{2n+2}	-	0.827 – 0.890 at 20 ºC
Oleic acid (90 %)	Sigma-Aldrich®	$CH_3(CH_2)_7CH=CH(CH_2)_7COOH$	282.46	-
Methanol	Sigma-Aldrich®	CH_3OH	32.04	-

3.2 Samples Preparation

Mn-doped CdSe QDs are synthesized by mixing two solutions precursor which is Cd-Mn solution and Se solution. The synthesized processes are done under an argon gas environment in the glove box. Cd-Mn solutions are prepared using 0.5 g of CdO, 0.5 g Mn acetate, 25 ml of paraffin oil and 15 ml of oleic acid which are loaded into a three necks round bottom flask. The solution heated and stirred to 160 °C using heating mantle until the CdO and Mn acetate were completely dissolve. Then, Se solution were prepared by heated mixture of 0.079 g of Se powder and 50 ml of paraffin oil to 220 °C with rapid stirring in another three necks round bottom flask. When the Se powder are completely dissolved at temperature 220 °C, about 5 ml of Cd-Mn solution are swiftly injected into Se solution with rapid stirring. For immediate sample (0 min), the heating process was immediately stopped just after the Cd-Mn solution injection had been done. For others samples, the temperature dropped to 210 °C immediately after the injection of Cd-Mn solution then rose back to 220 °C. The final temperature was maintained at 220 °C. The time was count immediately after the Cd-Mn solution injection for 0.2 min (12 sec). The same procedure repeated at different time interval, i.e. 0.5, 1, 5, 16, 46 and 90 mins. Finally, the precipitates were isolated from solvents and unreacted reagent via centrifugation. After been washed with methanol and distilled water consecutively, it was dried at 50 °C in vacuum oven.

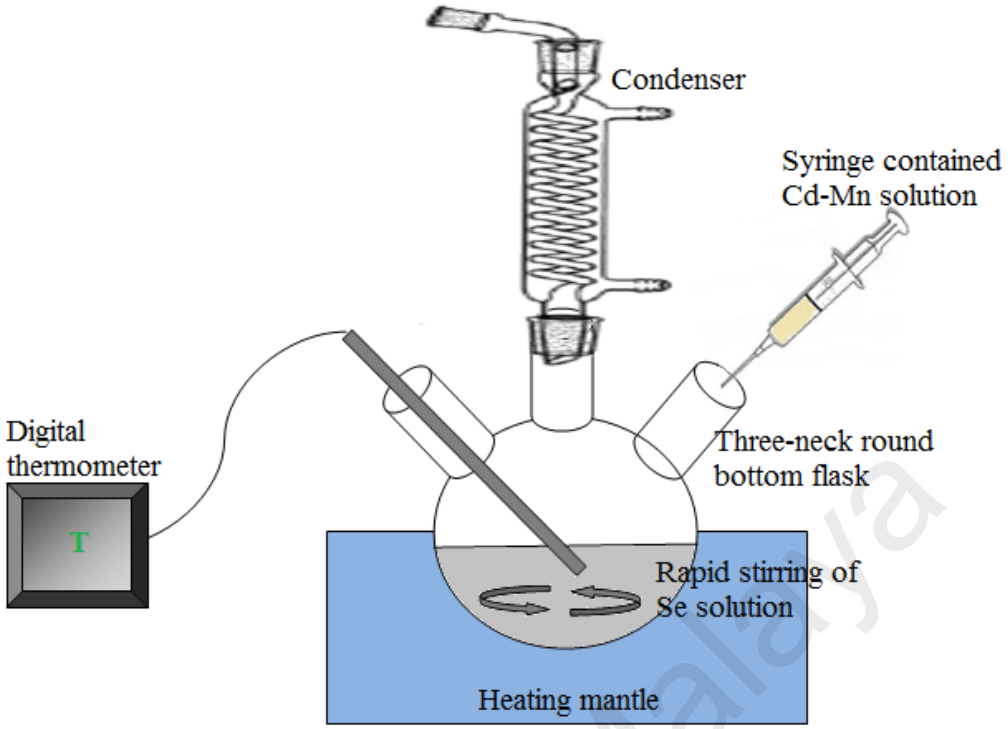

Figure 3.1: The experimental setup for Mn-doped CdSe QDs sample upon Cd-Mn solution injection into Se solution

3.3 Characterizations

The particles size determination of Mn-doped CdSe QDs was performed using High-resolution Transmission Electron Microscope (HRTEM) LEO LIBRA instrument operating at 120 kV. Powder formed samples of Mn-doped CdSe QDs are processed and dripped onto the Cu grid for HRTEM viewing. Using micrographs and atomic scale images of selected area are captured, the particles size and lattice parameter are measured accordingly.

The structural studies of Mn-doped CdSe QDs samples are performed using Panalytical Empyrean X-ray Diffractometer equipped with graphite monochromatized Cu Kα radiation (λ= 1.54060 Å) irradiated with a scanning rate of $0.02°s^{-1}$ and usable

range of 2º - 80º (2θ). This characterization required solid form samples that are securely tight in the sample holder to ensure the significant high intensity in XRD pattern produce. This is a crucial step because loose solid or powder may produce poor intensity which is undesirable.

The optical characterization studies of Mn-doped CdSe QDs samples are perfomed using UVIKON 923 Double Beam UV-vis spectrophotometer to obtain absorption spectra's and Pelkin Elmer LS55 Series PL with Xenon discharge lamp as it light source to obtain emission spectra's. Both equipments required a liquid samples Mn-doped CdSe QDs that are contained in the glass cuvette with 10 mm pathlength. Further Homogeneous dilution of all samples solution is required since spectra's shows supersaturated peaks especially for 16, 46 and 90 mins.

Infrared spectra of Mn-doped CdSe QDs samples are taken using a Perkin Elmer 2000 Fourier Transform Infrared spectroscopy (FTIR) wavenumber region between 4000 and 400 cm^{-1}. This FTIR are equipped with both solution and solid samples holder and tip. For this analysis purpose, the solution samples were used.

The raman scattering behavior will be observed using Horiba Scientific Xplora Micro-raman Spectroscopy with 532 nm laser source wavelength. The solid samples of Mn-doped CdSe QDs are observed under a microscope and the selected areas are targeted with laser.

The elemental compositions and chemical bonding states of solid Mn-doped CdSe QDs samples are observed using Axis Ultra DLD/Kratos/2009 X-ray Photoelectron Spectrometer (XPS) with 0.1 to 1 atomic % detection limit and 0.5 nm

depth profiles (Under argon gas environment). Figure 3.2 shows the overall synthesis and characterizations process of Mn-doped CdSe QDs.

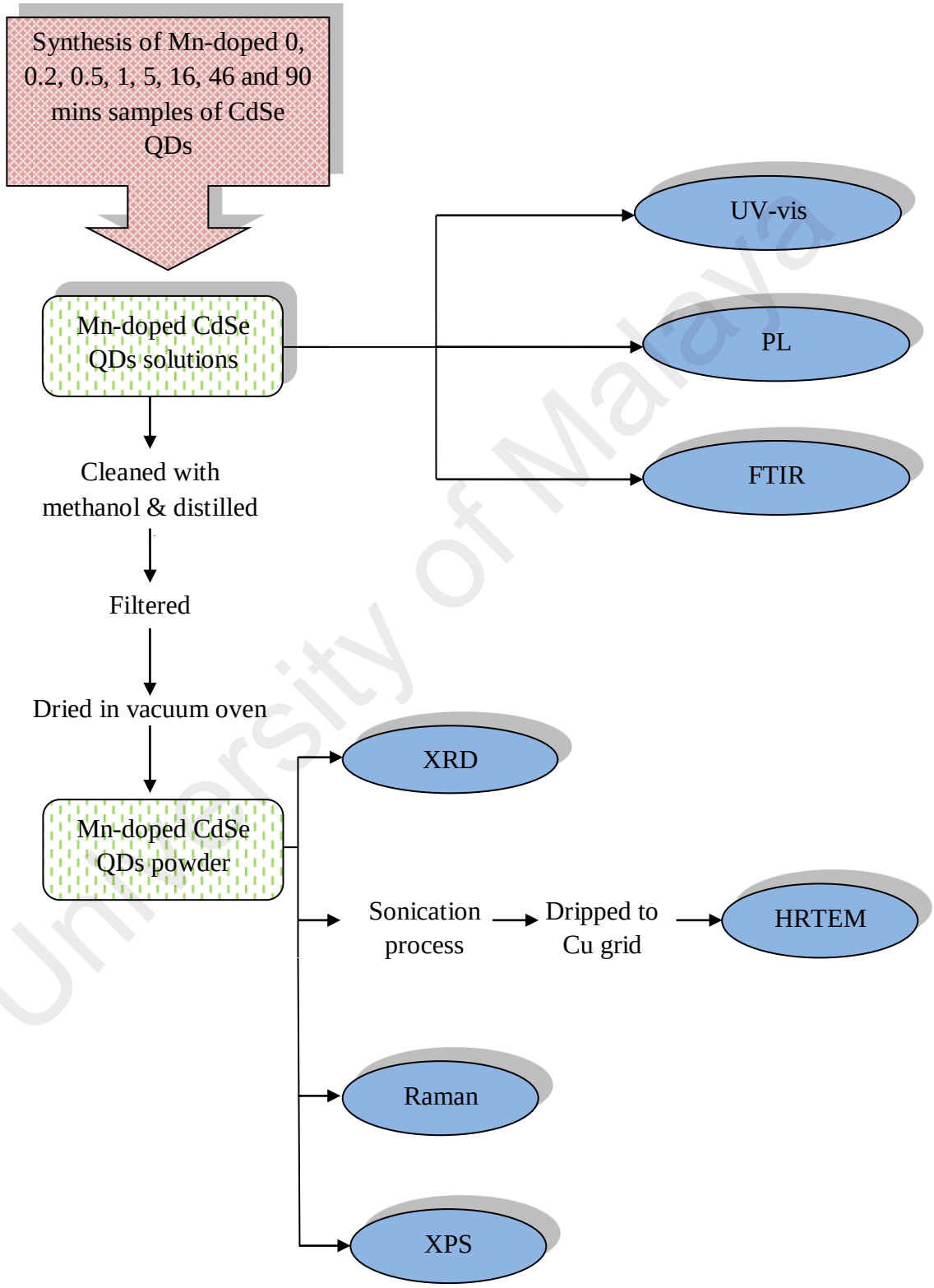

Figure 3.2: Flow chart of synthesis and characterization of Mn-doped CdSe QD

CHAPTER FOUR

RESULTS AND DISCUSSION

In this chapter, the results are thoroughly discussed and compared with the published literatures.

4.1 Physical Observations

Figure 4.1 shows vials containing solution of Mn-doped CdSe QDs. The variation in color was influenced by the sized change of Mn-doped CdSe QDs as a function of reaction time. The observed colours are due to of the strong photon absorption by the Mn-doped CdSe QDs at specific frequency. Sample with the immediate reaction time (0 min) exhibits a light orange colour. While sample with 0.2 min reaction times shows a more concentrated orange colour. The sample appears red at a reaction time of 0.5 and 1 mins. As the reaction times increases (16-90 mins), the color turn to dark brown, as in the Fig. 4.1, the solution appeared as light brown solution since the dark brown precipitates settled down on the bottom of the containers.

The variations in colour are attributed to the difference in QDs' sizes due to quantum confinement effect. Larger QDs emit longer wavelength and smaller QDs emit shorter wavelength resulting a different colour emission (Hamizi and Rafie, 2011). The sizes of the QDs were estimated from the absorption and photoluminescence spectra, and confirmed by HRTEM images.

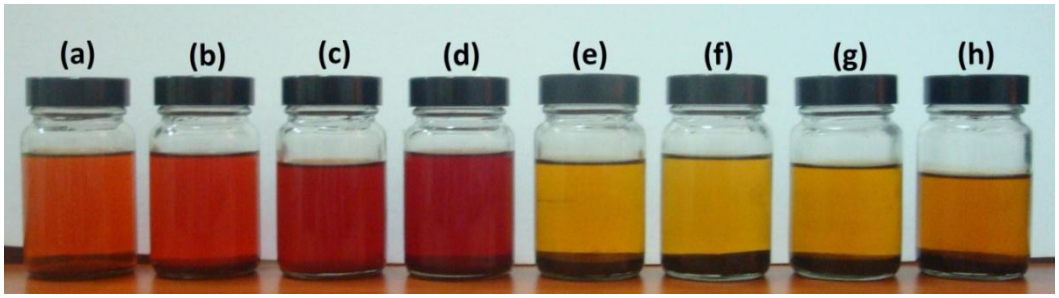

Figure 4.1: Mn-doped CdSe QDs samples with various colours at different reaction times: (a) 0 , (b) 0.2, (c) 0.5, (d) 1, (e) 5, (f) 16, (g) 46 and (h) 90 mins

4.2 High Resolution Transmission Electron Microscopy (HRTEM) Analysis

Figures 4.2- 4.9 show the typical HRTEM images for all Mn-doped CdSe QDs samples. The HRTEM images reveal that Mn-doped CdSe QDs posses a quasi-sphere shape for all reaction times. The dark area formed in the image due to the high density of particles.

The QDs mean size and distributions are measured of one hundred particles as plotted in histogram (insert) in respective figures. The average physical sizes of the Mn-doped CdSe QDs are range from 3 to 14 nm (± 0.1 – 0.9) for 0 to 90 mins reaction time, respectively. This results shows that Mn-doped CdSe QDs shows a slight increment in QDs physical size as compared to pure CdSe QDs (Hamizi & Johan, 2010). Kwak et al. (2007) reported the significantly larger size of Mn-doped CdSe QDs produced compared to pure CdSe QDs which can be due to the contribution of Mn which shelled the CdSe QDs core (Kwak et al., 2007).

The growth of QDs is a function of the reaction time as proved in Figure 4.1. The nucleation process of Mn-doped CdSe was occcured immediately after the injection of Mn-Cd complex into Se solution. The rapid growth of QDs may not occur immediately (0 min), but started at a few seconds later after the heating process was stopped. This is because of the solvent temperature are not immediately dropped after stopping the heating process were stop.

Figure 4.10 shows the relationship of QDs growth with reaction time. The growth of QDs is very significant at the early reaction time (0 to 0.5 mins). The growth most rapidly occur was from 0.2 to 0.5 min transition time, since the high energy surface was

largely used to initiate the nucleation of Mn-doped CdSe QDs at the initial stage (0 – 0.2 mins). However, as the reaction time is increased, the growth becoming less prominent, especially from 0.5 to 90 min. This is due to the ionic concentration reduction of the chemical precursor in the solution as the time become longer (Sung et al., 2008, Jiang & Muscat, 2012).

In addition, narrow particles size distribution was observed in each sample. Despite the narrow size distribution, the overall size distribution seem to shows a slight increment over the reaction time. This due to the particles agglomeration creates a larger size of QDs. Simultaneously, the growth of intrinsic QDs is still ongoing due to the chemical precursor residue. This will create a wide QDs size distribution. The tendency of agglomeration may due to the excessive high surface energy on the QDs surface compare to the core or bulk of QDs throughout the heating process which favorable to the built-up of surface or shell of QDs. Meaning that, as long as the heating is exist, the QDs have the tendency to growth. Despite this, the concentration of chemical precursors such as Cd, Se and Mn are dropped as the reaction time increases. This will retard the creation of QDs surfaces. Hence, instead of creating a QDs, the excessive surface energy would increase the propensity of QDs agglomeration (Sung et al., 2008).

Another essential point of QDs agglomeration is the reduction of surfactant concentration in proportion to the increasing reaction time, since oleic acid is the crucial chemical to create oleate shell (Mn-oleate and Cd-Oleate) on the surface of QDs (Jiang & Muscat, 2012).

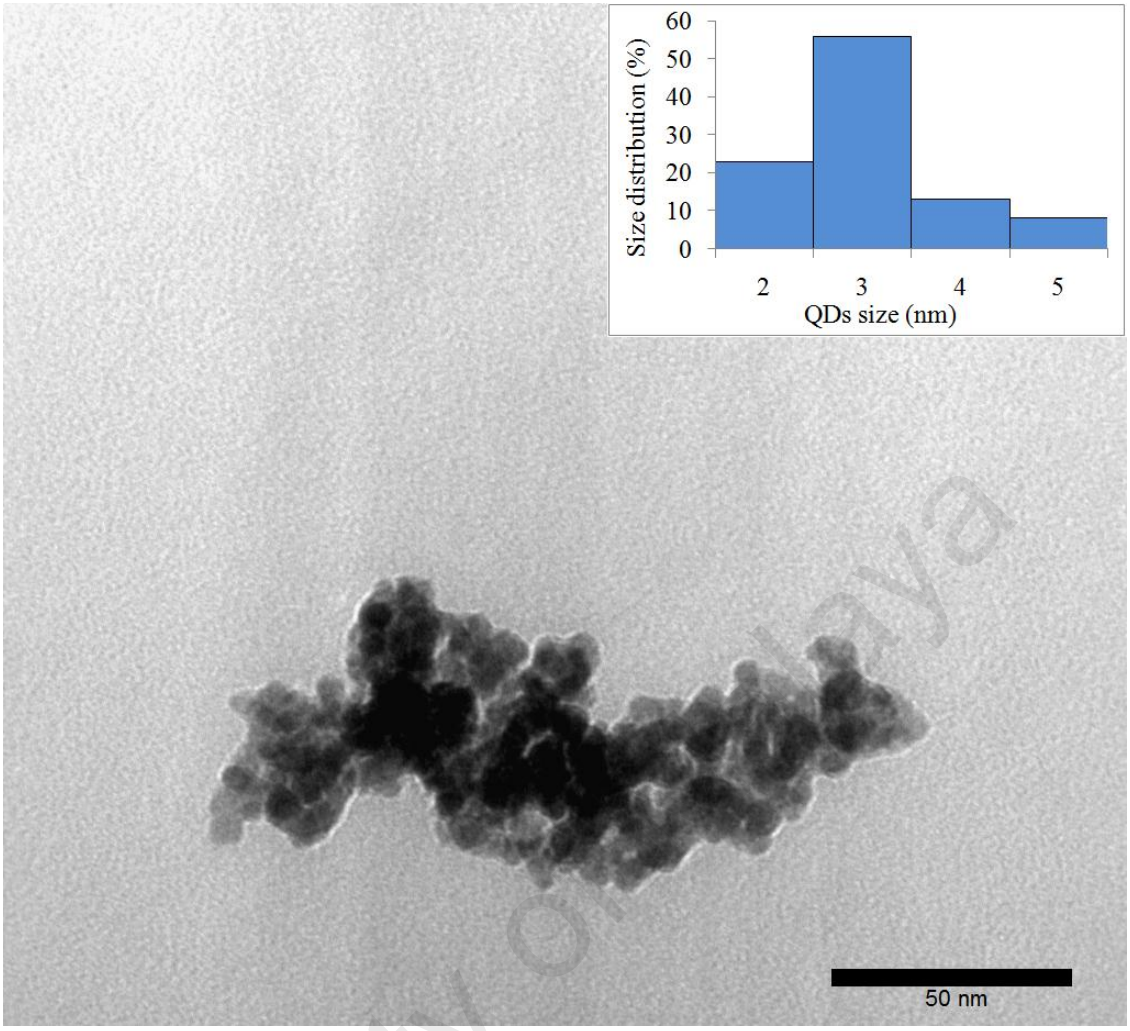

Figure 4.2: HRTEM image of Mn-doped CdSe QDs with QDs size distribution (insert) at 0 min reaction time

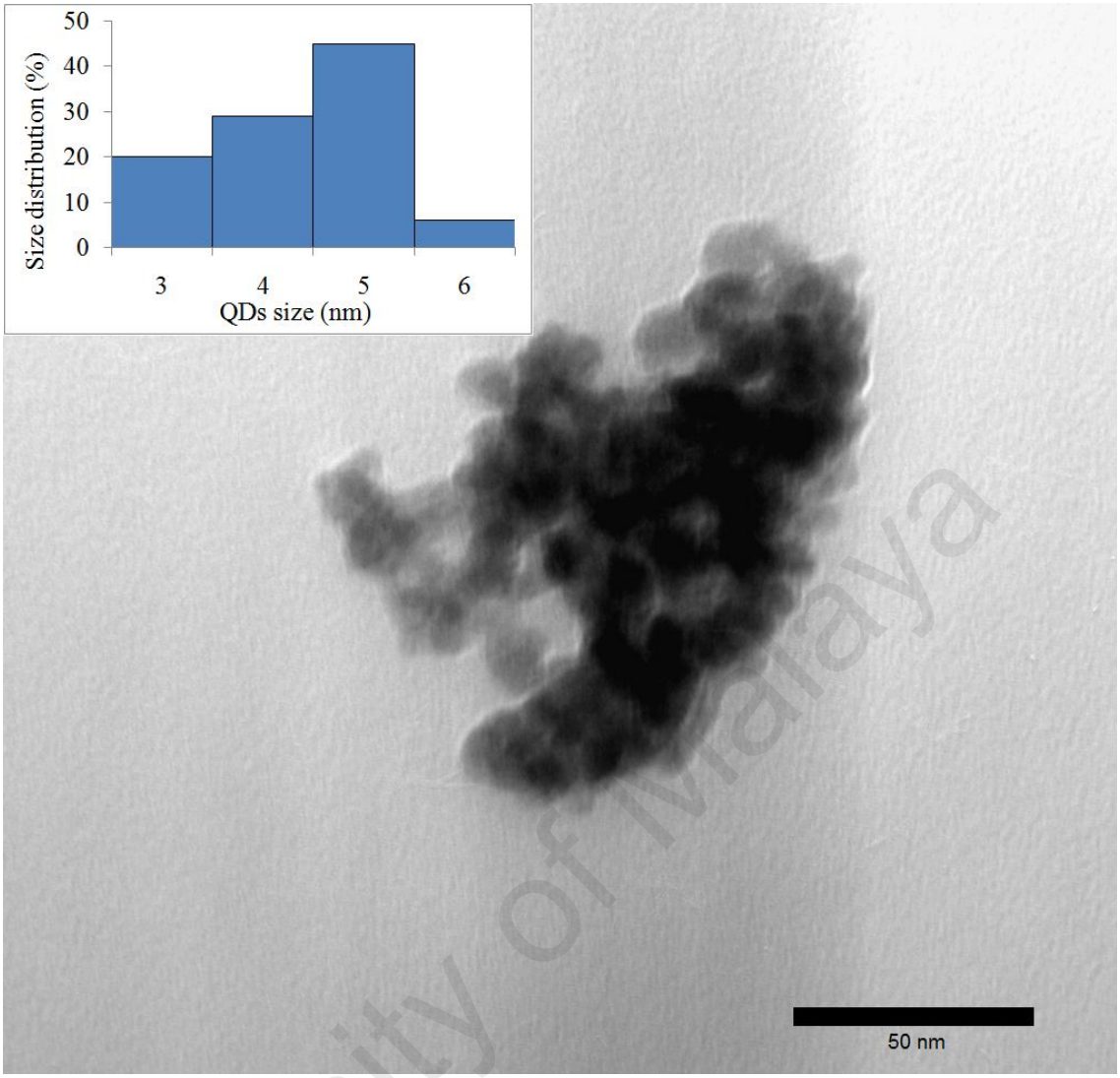

Figure 4.3: HRTEM image of Mn-doped CdSe QDs with QDs size distribution (insert) at 0.2 min reaction time

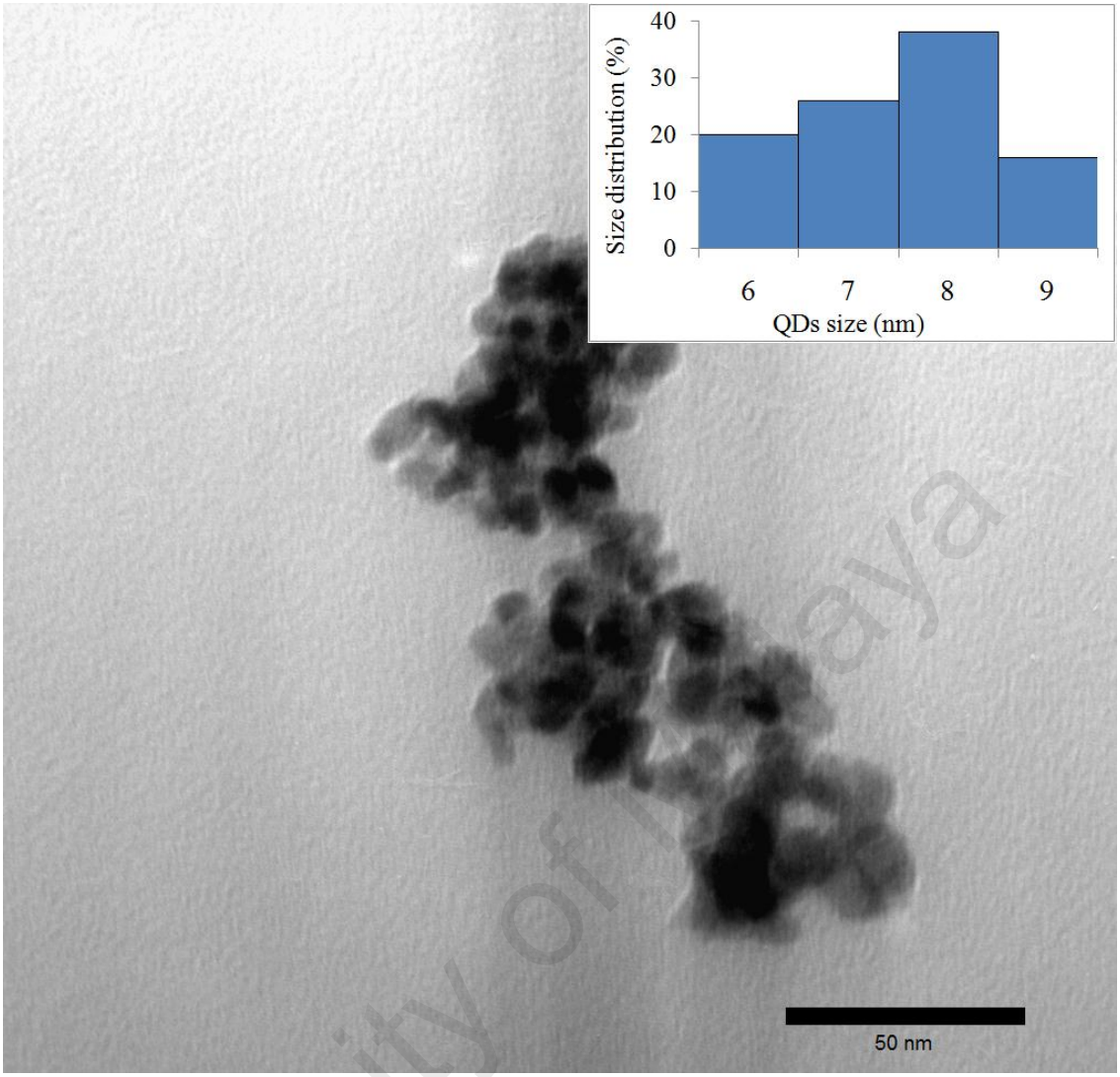

Figure 4.4: HRTEM image of Mn-doped CdSe QDs with QDs size distribution (insert) at 0.5 min reaction time

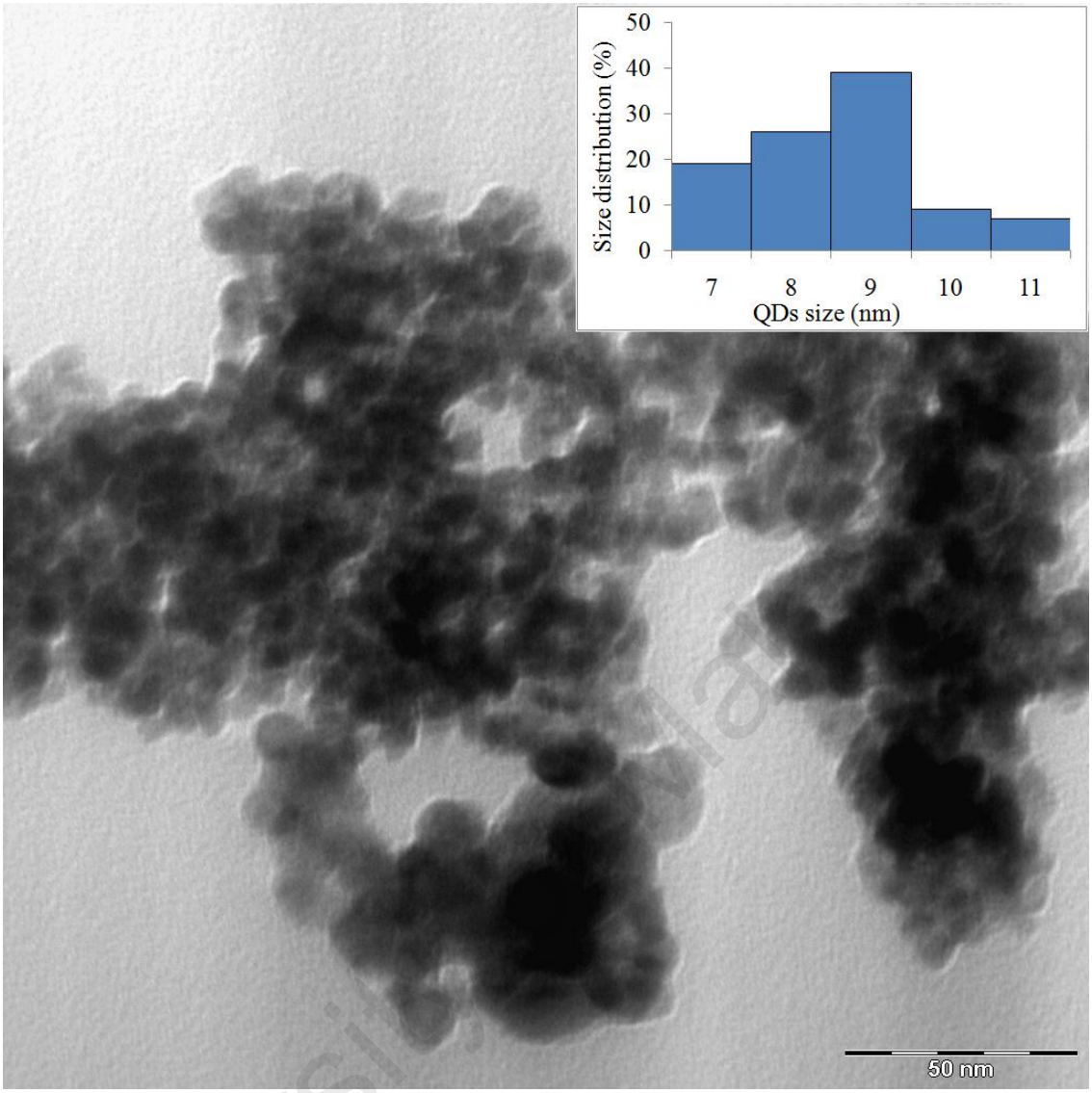

Figure 4.5: HRTEM image of Mn-doped CdSe QDs with QDs size distribution (insert) at 1 min reaction time

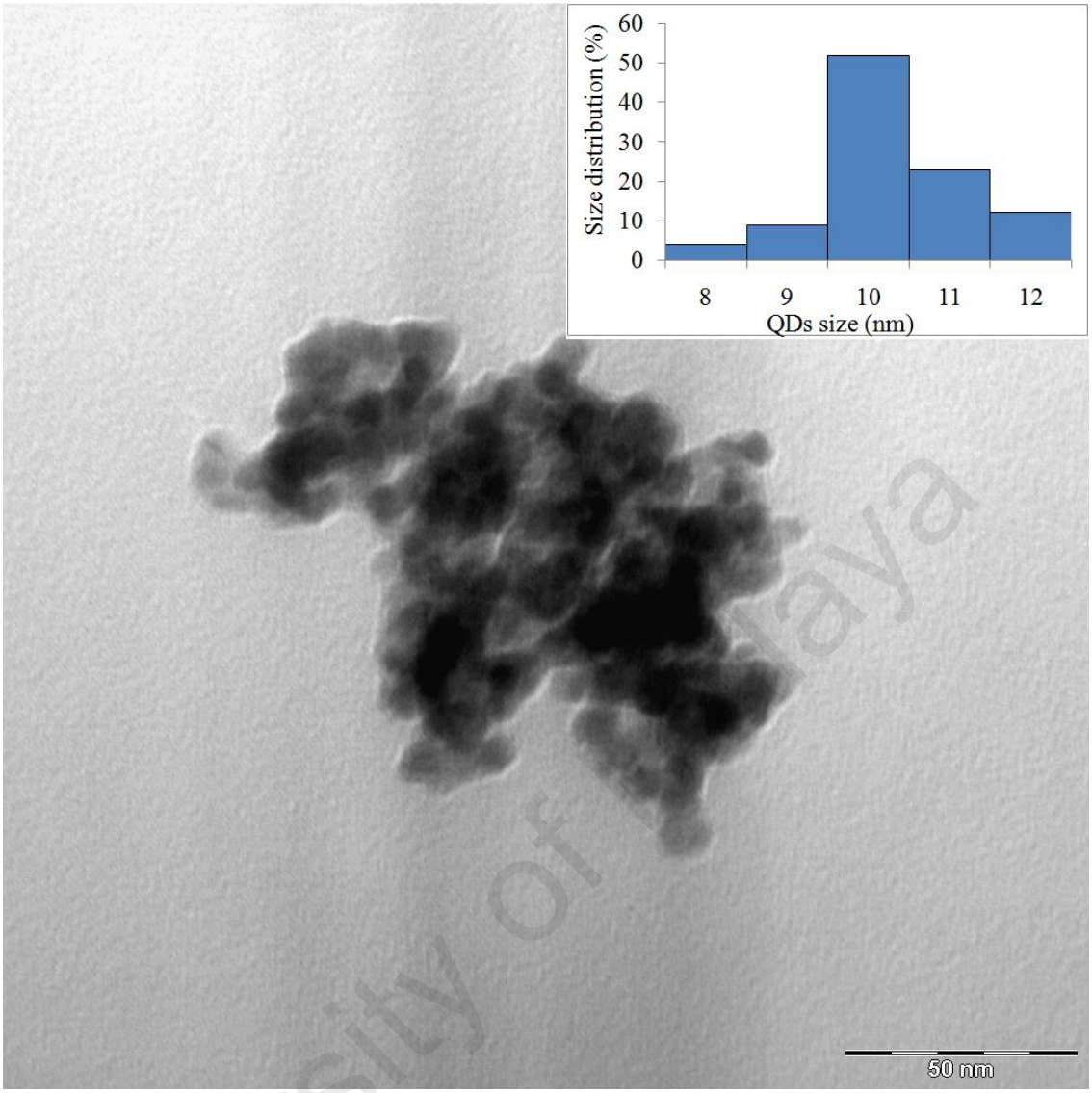

Figure 4.6: HRTEM image of Mn-doped CdSe QDs with QDs size distribution (insert) at 5 min reaction time

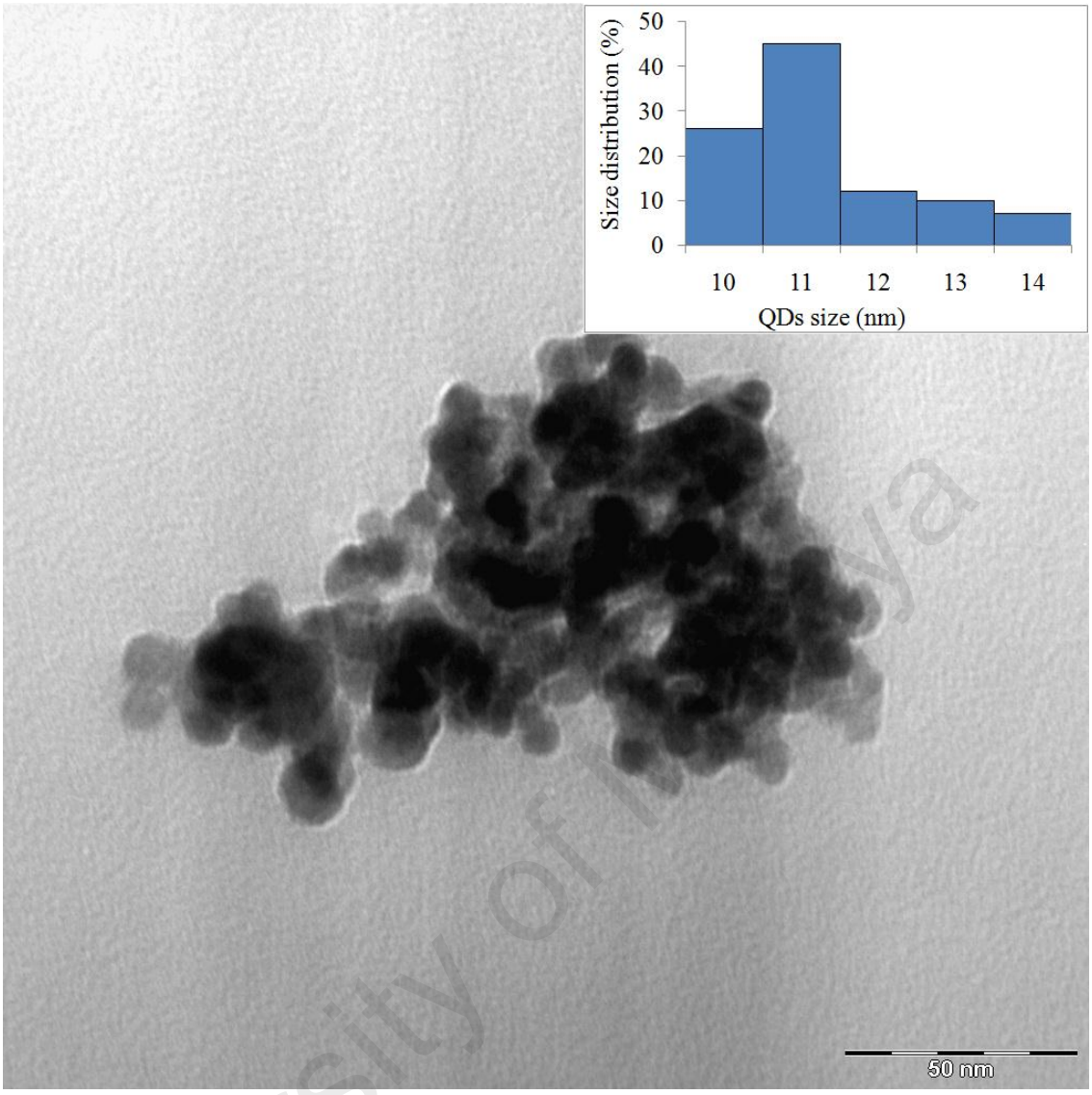

Figure 4.7: HRTEM image of Mn-doped CdSe QDs with QDs size distribution (insert) at 16 min reaction time

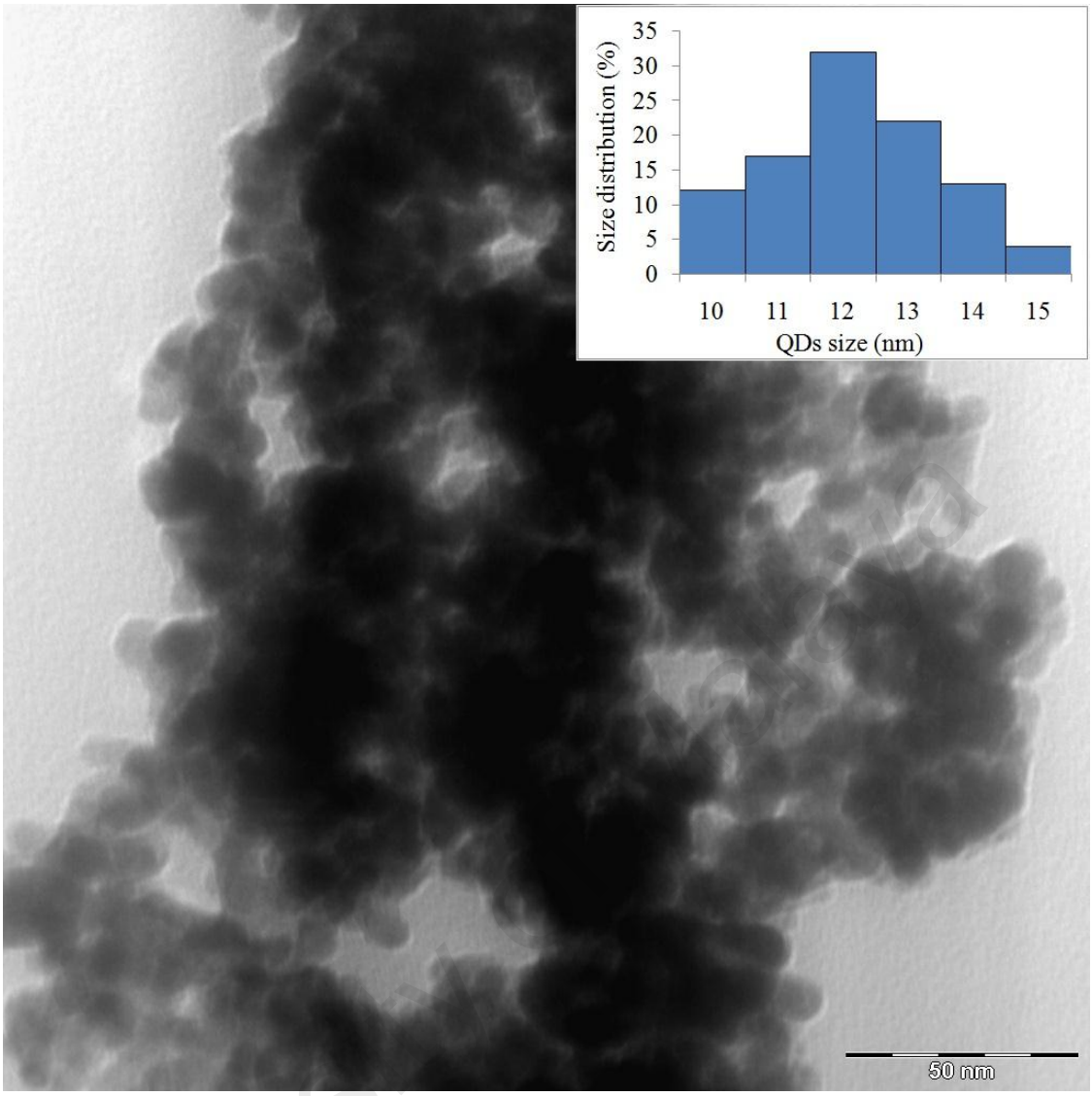

Figure 4.8: HRTEM image of Mn-doped CdSe QDs with QDs size distribution (insert) at 46 min reaction time

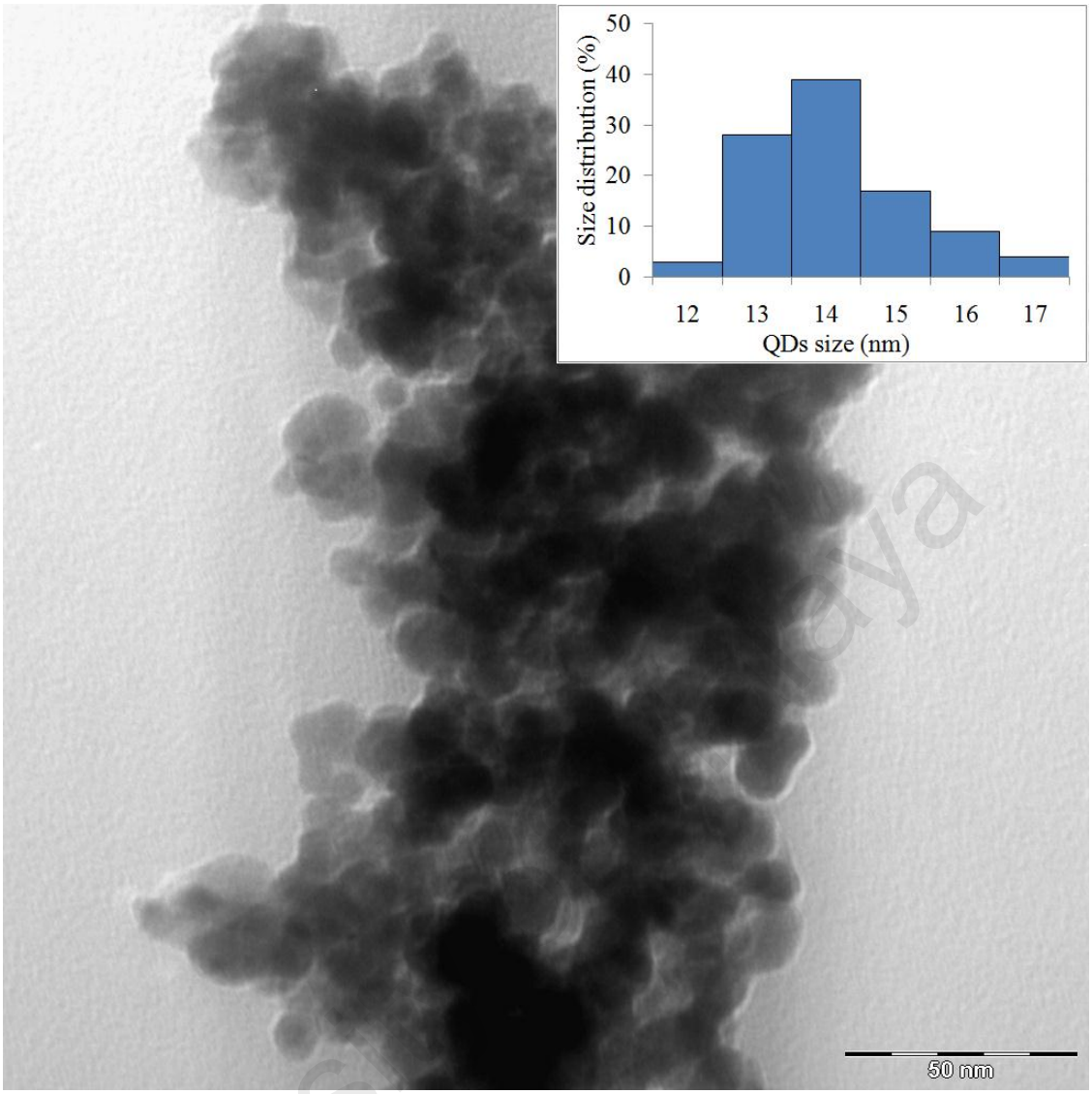

Figure 4.9: HRTEM image of Mn-doped CdSe QDs with QDs size distribution (insert) at 90 min reaction time

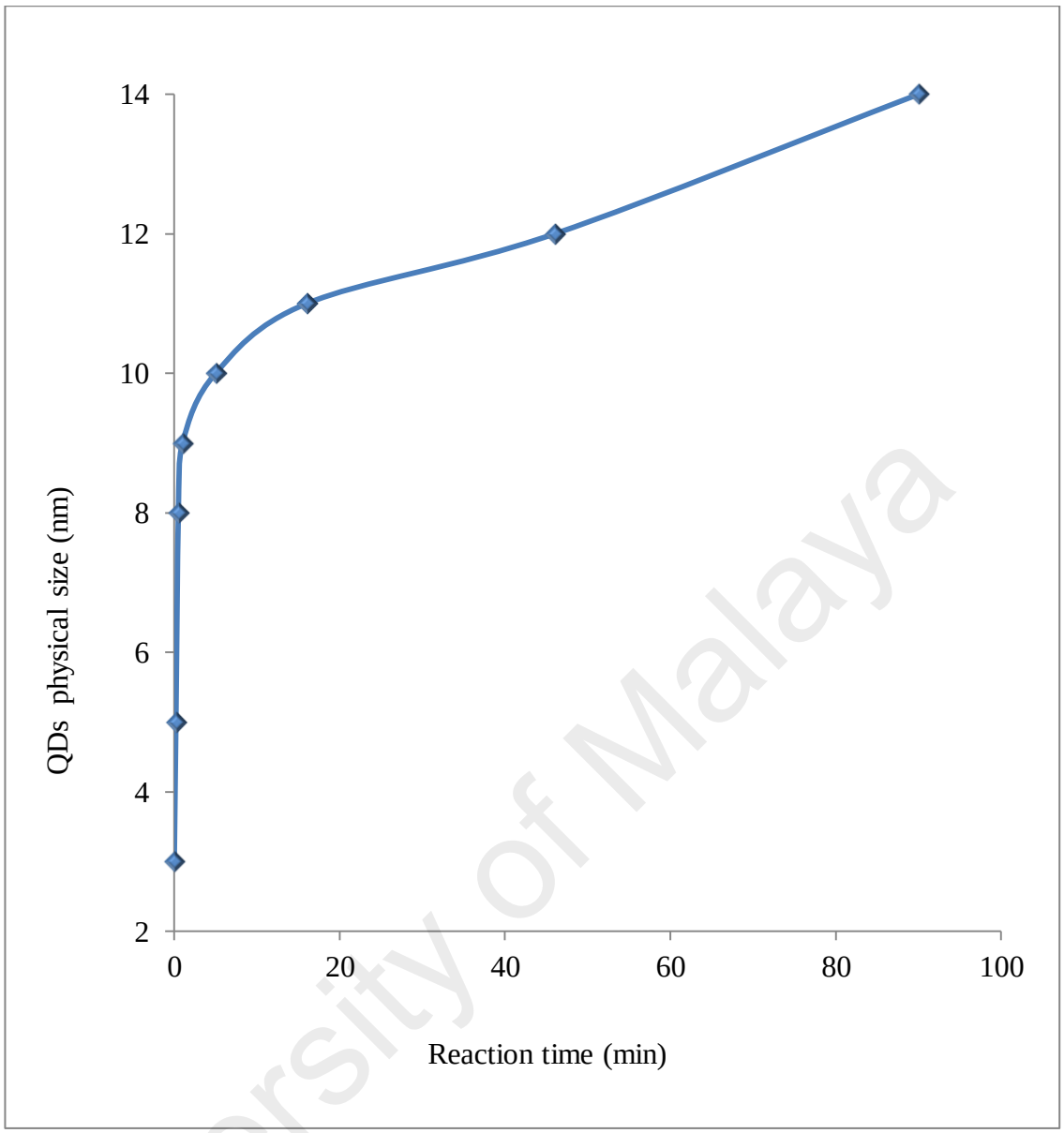

Figure 4.10: The growth of QDs with reaction times

The lattice structures of Mn-doped CdSe QDs samples are shown in Figures 4.11- 4.19. Lattice distance or lattice parameter (*a*) at twenty isolated area are measured and the average value are tabulated in Table 4.1. From the HRTEM results, Mn-doped CdSe QDs have small lattice parameter ranging from 1.8 to 3.9 Å compared to bulk CdSe (300K) with 6.050 Å lattice parameter (Hotje et al., 2003). The introduction of smaller Mn^{2+} ion (~0.8 Å) into CdSe QDs core resulting in significant lattice straining through compression. This lattice parameter compression was also observed in Mn-doped into CdS and ZnS (Bryan & Gamelin, 2005). The shrink in lattice parameters in

Mn-doped CdSe QDs system also shows in the XRD analysis where the value is range from 4.5 to 4.6 Å. The QDs shows strong lattice strain impact on it lattice parameter compare to the bulk QDs because of its significantly small size and doping of ion on the surface of the QDs (Bryan & Gamelin, 2005).

As tabulated in Table 4.1, the lattice strain density increases with decreases of QDs size. This may due to the rise of quantum confinement effect in smaller QDs which allows the stress induced by the lattice mismatched to be scattered on the QDs surface. In addition, the large surface area and curve surfaces of smaller QDs permitted stress to be widely distributed intensively to the constituent atoms on the QDs surfaces. On the other hand, for larger QDs or bulk, the epitaxial stress tends to form a strain relaxing crystalline defect despite homogeneous strain. This is because of the large overall number of atoms on the surface but only small amount of constituents atoms are enclose by the epitaxial stress. The lattice strain phenomenon caused the significant change in band gap energy, which is essential for Mn-doped CdSe QDs optical property (Chen et al., 2012, Smith & Nie, 2009; Smith et al., 2009).

Chen et al. (2012) reported the influence of Mn^{2+} dopant to the local lattice strain in the Mn-doped CdS/ZnS nanocrystals surface. The introduction of Mn dopant, increase the density of lattice strain at the shell of the QDs (Chen et al., 2012). Thus, in Mn-doped CdSe QDs the lattice structure and spatial may reduce because of the Mn doping.

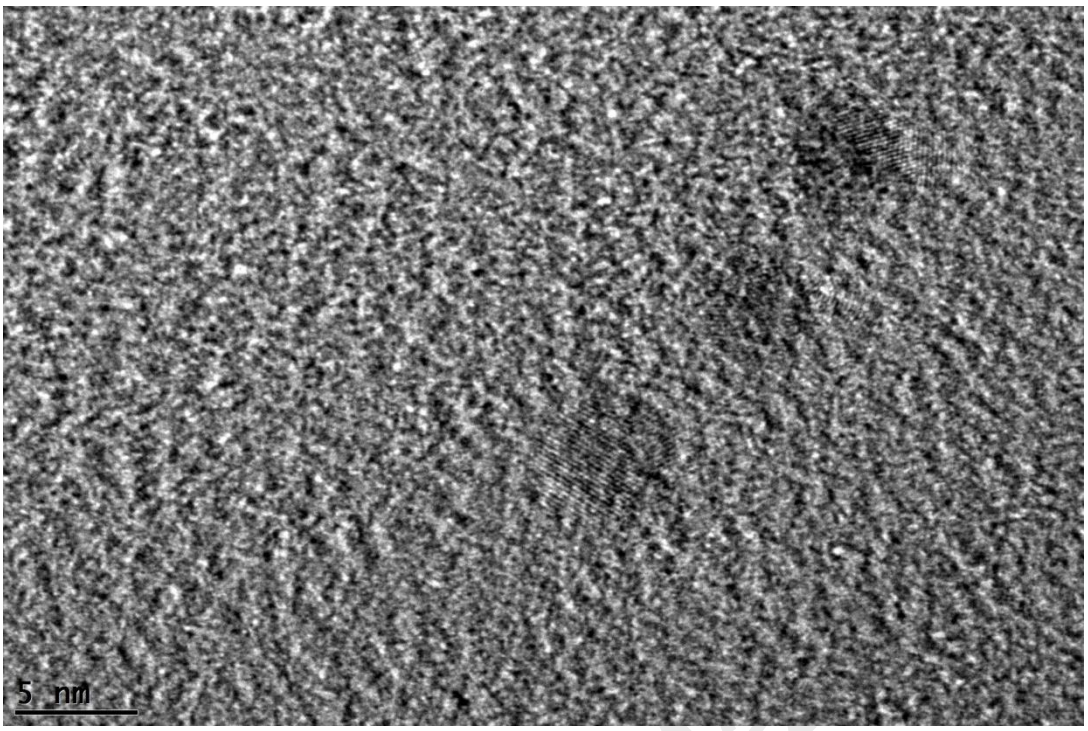

Figure 4.11: HRTEM image of Mn-doped CdSe QDs lattice of 0 min sample

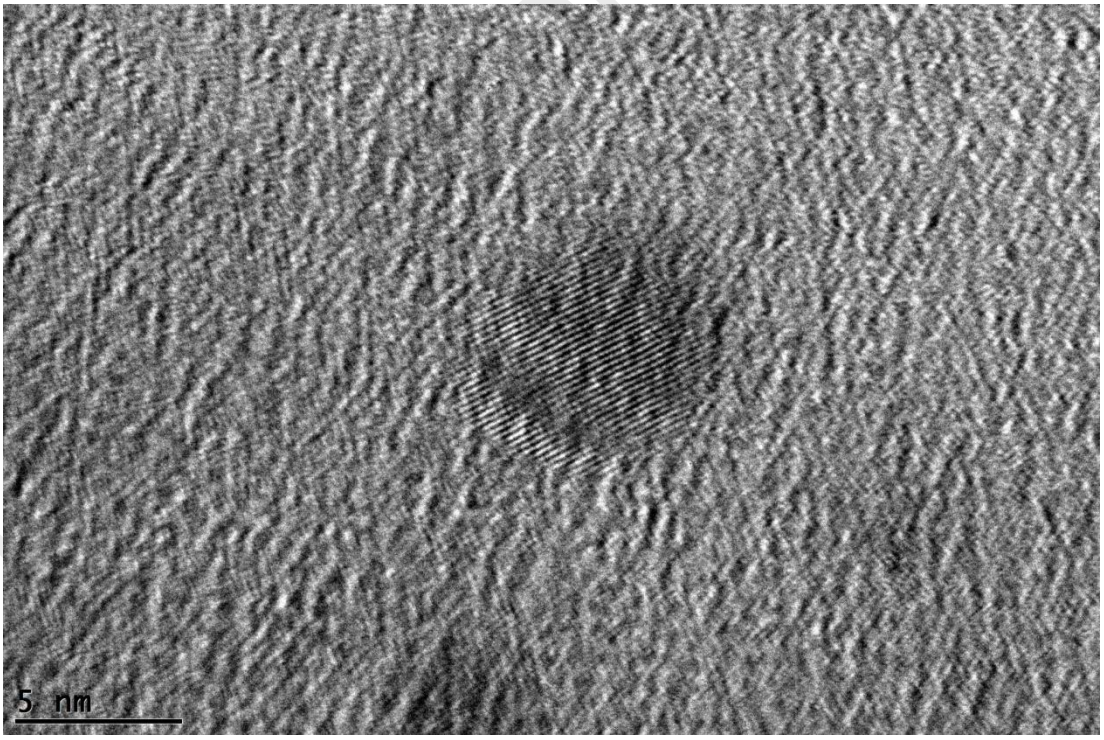

Figure 4.12: HRTEM image of Mn-doped CdSe QDs lattice of 0.2 min sample

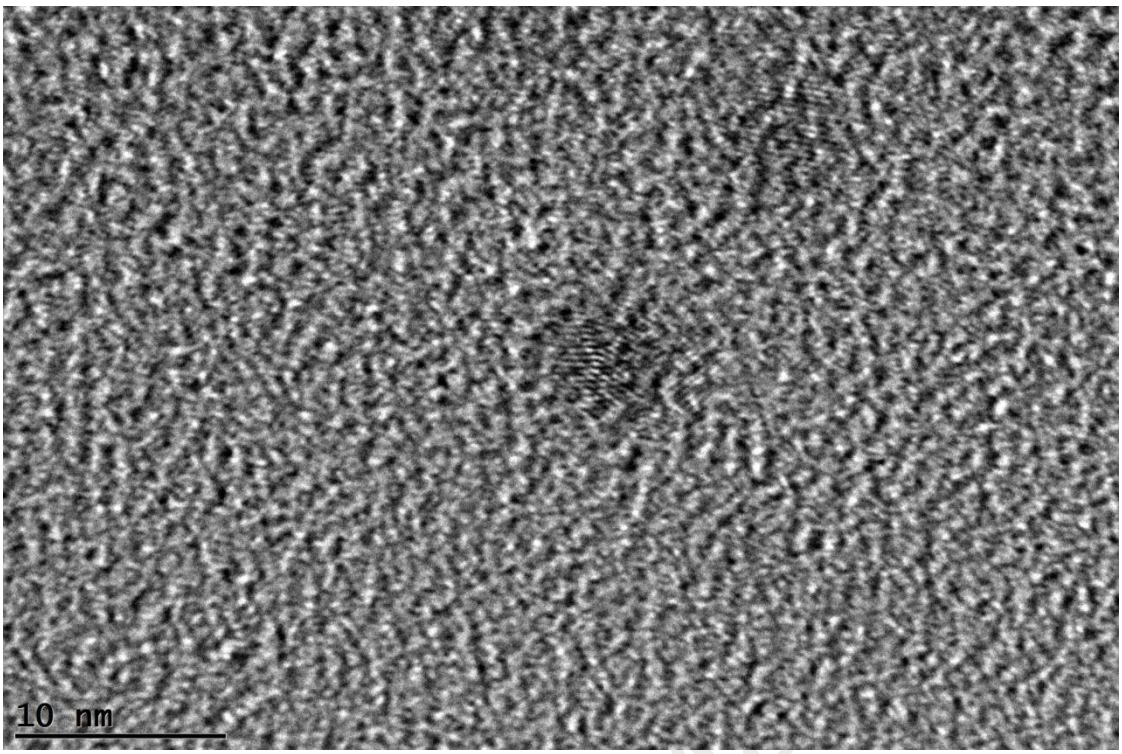

Figure 4.13: HRTEM image of Mn-doped CdSe QDs lattice of 0.5 min sample

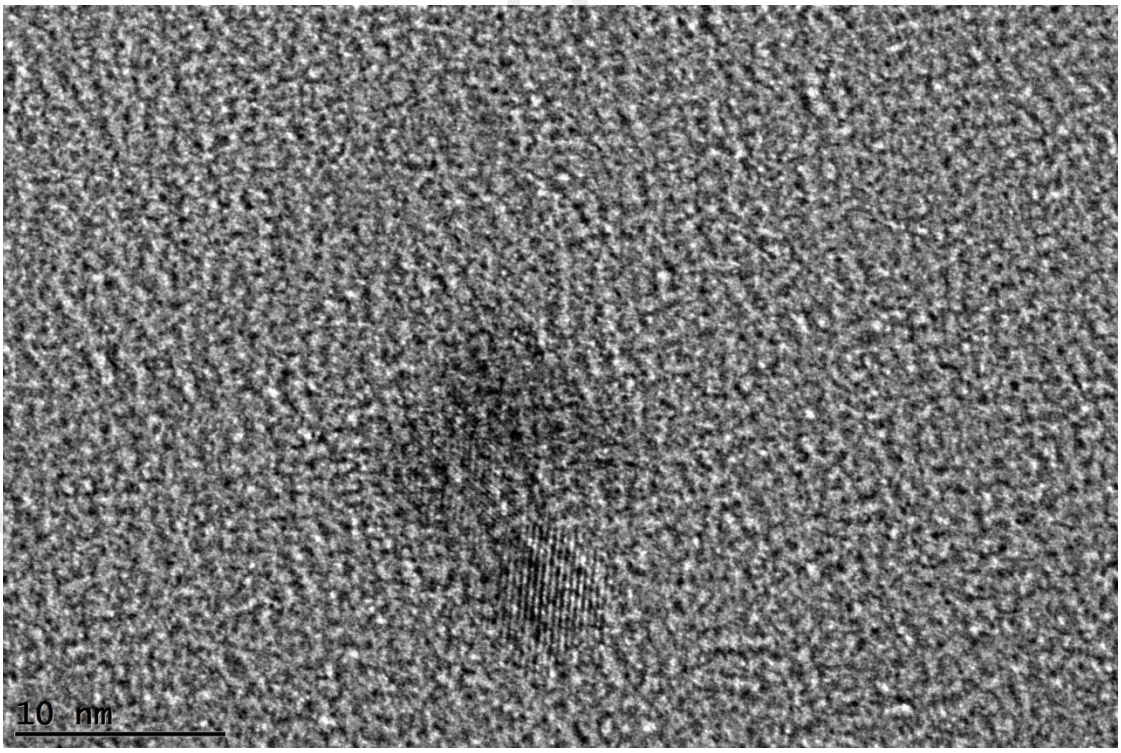

Figure 4.14: HRTEM image of Mn-doped CdSe QDs lattice of 1 min sample

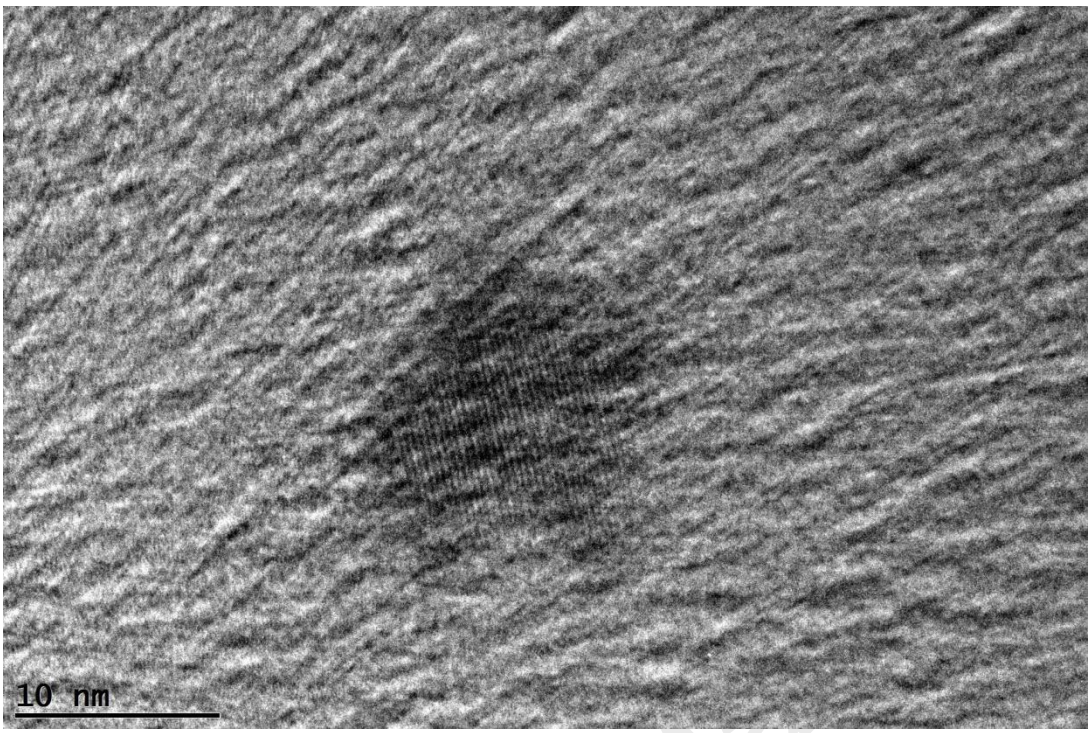

Figure 4.15: HRTEM image of Mn-doped CdSe QDs lattice of 5 min sample

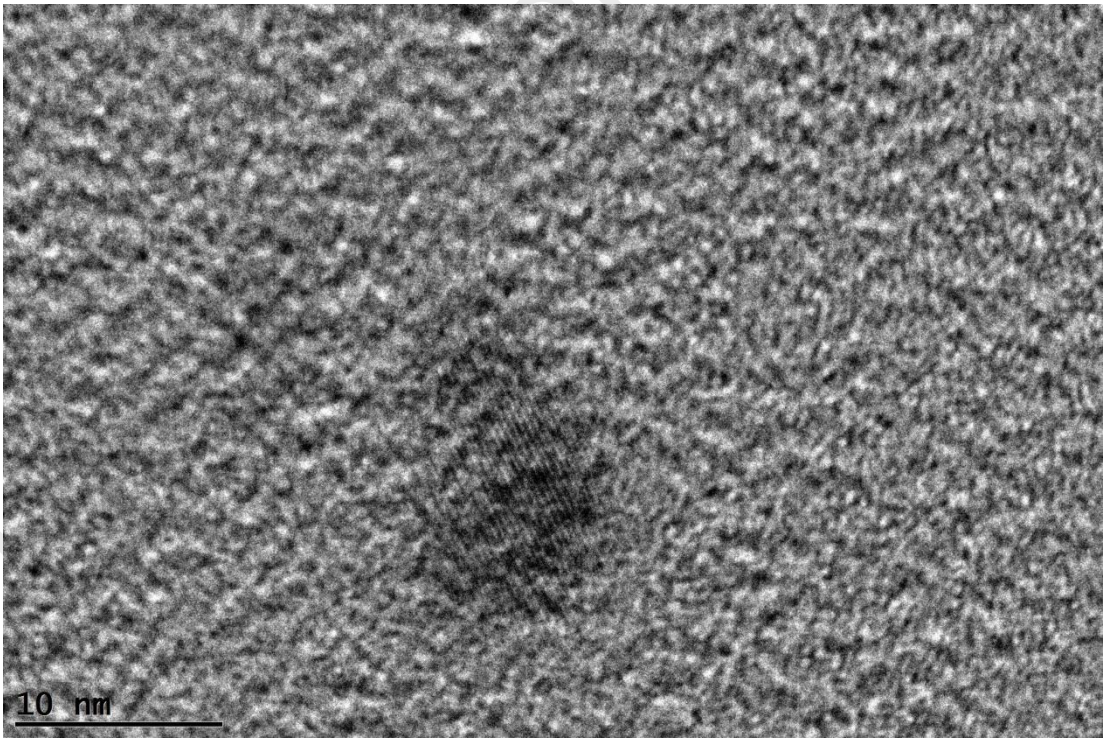

Figure 4.16: HRTEM image of Mn-doped CdSe QDs lattice of 16 min sample

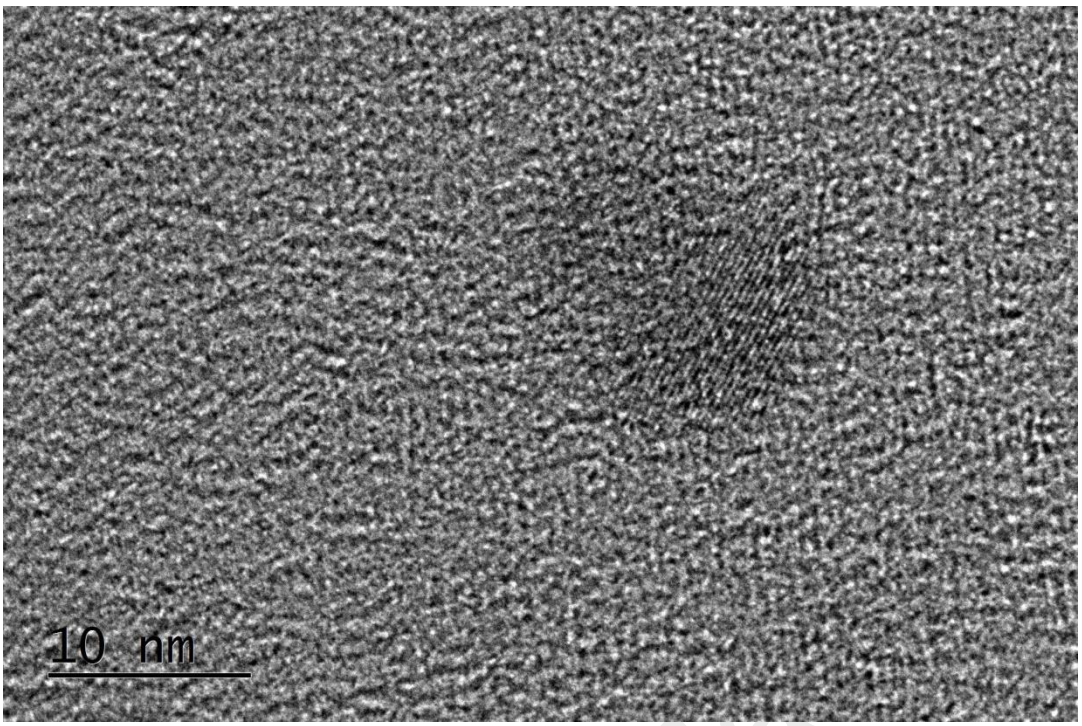

Figure 4.17: HRTEM image of Mn-doped CdSe QDs lattice of 46 min sample

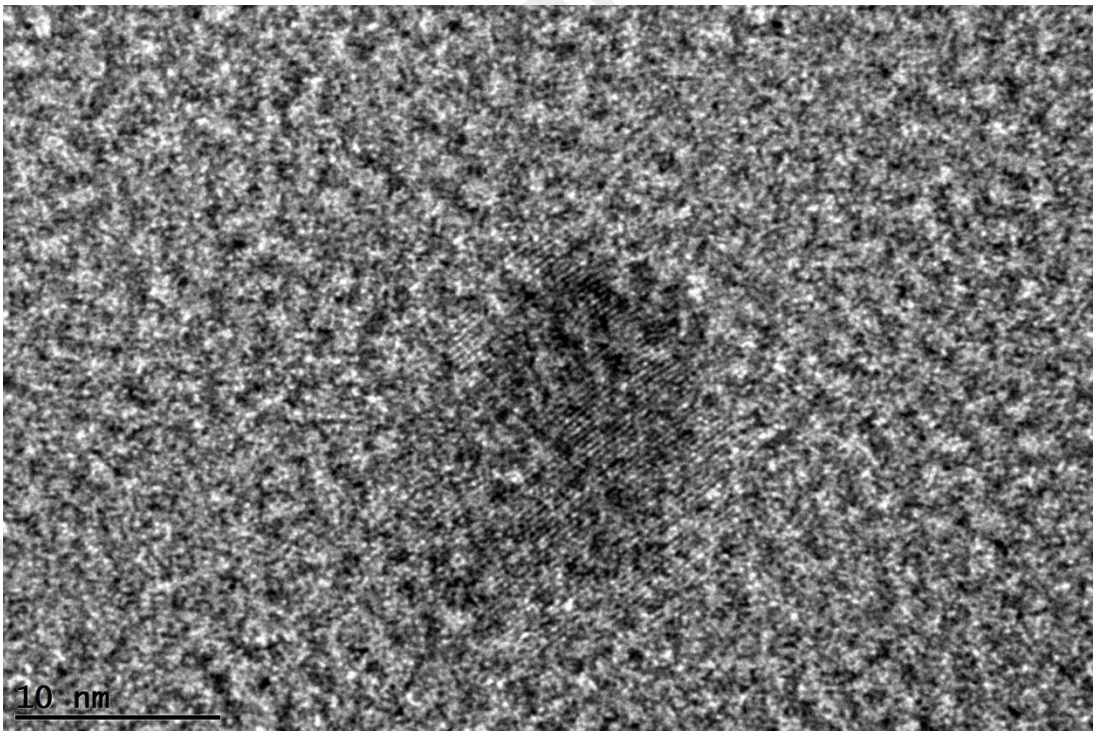

Figure 4.18: HRTEM image of Mn-doped CdSe QDs lattice of 90 min sample

Table 4.1: Lattice parameter of Mn-doped CdSe QDs for all samples

QDs size (nm)	Latice parameter, *a* (Å)	
	HRTEM	XRD
3	1.8	2.09
5	1.9	2.13
8	1.9	2.14
9	2	2.16
10	2.1	2.24
11	3.1	2.29
12	3.6	2.37
14	3.9	2.56

4.3 X-Ray Diffraction (XRD) Analysis

The crystal structure of Mn-doped CdSe QDs was determined by XRD diffraction pattern as shown in Figure 4.19. Three well-defined peaks were observed at 2θ = 24.7 º, 41.6 º and 49.3 º correspond to (111), (220) and (311) planes respectively. This is in good agreement with Kwak et al. (2007), with an extremely small shift (~0.02 º - 0.04 º) (Kwak et al, 2007). Furthermore, this XRD pattern shows that as-synthesized Mn-doped CdSe QDs formed the zinc blende structure due to the low synthesis temperature (220 ºC). In other chemical synthesis process, like TOP based route produced wurtzite structure due to high synthesis temperature reach up to 300 ºC (Dongzhi et al., 2007). The long and complex molecular chains of oleic acid that acted as a surfactant may also contribute to the formation of zinc blend structure at {100} planes which have higher binding energy in Mn-doped CdSe QDs system (Kwak et al., 2007).

Peaks are shifted slightly in the XRD pattern as compared to pure CdSe QDs which located at 2θ = 25.9 º, 42.5 º and 50.3 º (Hamizi & Johan, 2010). This shifting trend toward the lower angle (~ 0.9 º to 1.2 º) may correspond to the filled of Mn ion in the interstitial site in the {001} planes face centered cubic lattice. Mn^{2+} ion has high tendency to fill the interstitial site of CdSe QDs lattice due to a typically small size of Mn^{2+} ion (~0.8 Å) compare to Cd^{2+} ion (~0.95 Å) (Bryan & Gamelin, 2012; Kwak et al., 2007) . This interstitial phenomenon of Mn into CdSe QDs lattice can contribute to the lattice microstrain that results in expansion or compression of CdSe core lattice (Kwak et al., 2007).

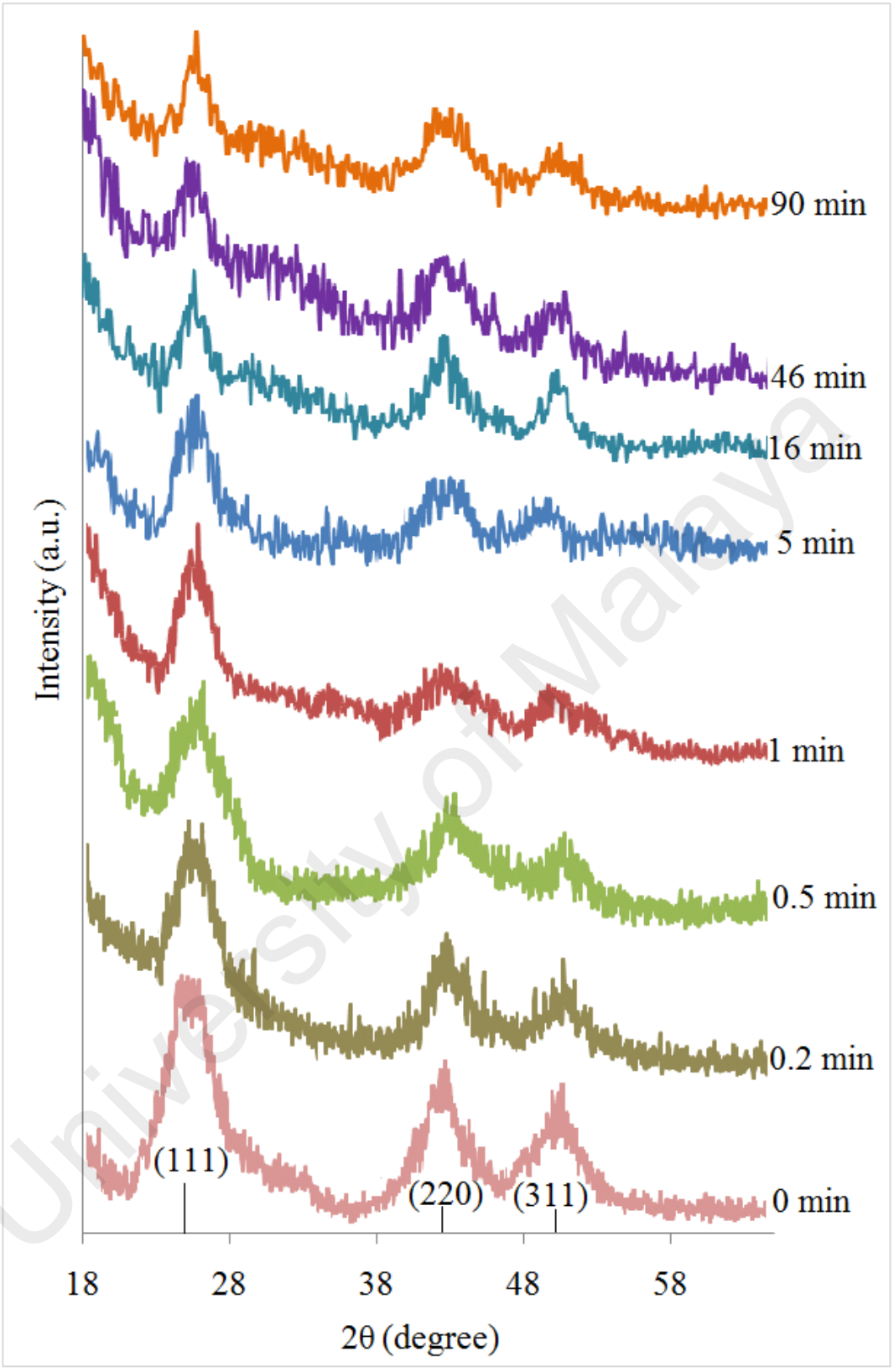

Figure 4.19: XRD patterns of Mn-doped CdSe QDs samples at various reaction times

Table 4.2: FWHM of (111) XRD peaks and the calculated crystallite sizes of Mn-doped CdSe QDs at various reaction times

Reaction time (min)	FWHM (radian)	Crystallite size (nm)
0	0.058	2.46
0.2	0.049	2.90
0.5	0.035	4.06
1	0.034	4.18
5	0.033	4.30
16	0.029	4.93
46	0.027	5.20
90	0.026	5.46

Table 4.2 shows the full-width of half maximum (FWHM) of peak correspond to (111) plane. The peak was broaden as the reaction time decreases. The crystallite sizes were calculated using Scherrer`s formula through the obtained FWHM values. As shown in the table, the crystallite size shows increment trend as a function of reaction times. This is in good agreement with results of physical size in HRTEM images (Figures 4.2 – 4.9). The crystallite size is most likely smaller than particles size because it has small degree of nanostrustural lattice coherence compared to particle size. In elaboration, crystallite sizes are notable to be similar to grain size of a single crystal. Likewise particles size is a size of a single crystal or the agglomeration of several crystals (Hamizi & Johan, 2010).

Table 4.3: FWHM of XRD diffraction peaks of Mn-doped CdSe QDs correspond to (111), (220) and (311) planes

Reaction time	FWHM (radian)		
(min)	(111)	(220)	(311)
0	0.058	0.035	0.029
0.2	0.049	0.029	0.029
0.5	0.035	0.029	0.012
1	0.034	0.052	0.029
5	0.033	0.058	0.035
16	0.029	0.029	0.029
46	0.027	0.046	0.029
90	0.026	0.052	0.029

XRD peak broadening feature not only limited to the QDs size reduction, but also on the anistropic peak broadening. Table 4.3 tabulated the individual FWHM diffraction peak correspond to (111), (220) and (311) planes. The (111) peak shows wider FWHM compared to (220) and (311) peaks for 0, 0.2 and 0.5 mins samples. This indicates that the QDs dimension is reducing dominantly in perpendicular to (111) planes direction where the unit cell *h*, *k*, and *l* were not equal to zero (Smith et al., 2008). On the other hand, for 1, 5, 46 and 90 mins samples, the (220) diffraction peaks shows wide FWHM in comparison with (111) and (311) peaks. This may correspond to the QDs dimension is decrease priory in perpendicular to (220) particular planes direction which the unit cell *l* is equal to zero. Dispites, 16 min samples diffraction peak FWHM remained constant for each peak. The anisotropic broadening in Mn-doped

CdSe QDs shows to be less dependent on the size of the QDs (Thanikaikarasan et al., 2011, Smith et al., 2009, Devi et al., 2014).

The lattice parameter analyzed from XRD analysis (Table 4.1) shows increment pattern as a function of QDs sizes. This indicate that the lattice is experience compression or expansion strain which independent from the of QDs sizes (Thanikaikarasan et la., 2011).

The pure CdSe QDs reported to have broader XRD diffraction peak (111) compared to Mn-doped CdSe QDs, since the crystallite size reported to be in a range of ~2 to 4 nm (Hamizi & Johan, 2010). This narrowing diffraction peak in Mn-doped CdSe QDs may caused by the lattice strain phenomenon, which also called microstrain since it occasionally happen in the nanocrystalline materials. The interstitial of Mn^{2+} ion into the CdSe QDs lattice introduced microstain to the unit cells that can cause by the un-uniform lattice distortion (Chen et al., 2012). It can be assume that the strain introduced to the CdSe QDs lattice induced the compression towards lattice parameter as results of the Mn^{2+} interstitials, since lattice parameter recorded in Table 4.1 are smaller in comparison which pure CdSe QDs (Hamizi & Johan, 2010).

The contribution of crystallite size and microstrain to the broadening of XRD peak can be exploited for the determination of the strain which dominantly to lattice strain, since both parameters are changing with Bragg angle. Graph of $\beta_r cos\theta$ versus $sin\theta$ are plotted by taking the consideration of zero instruments effect (β_i) on XRD peaks broadening since the value is extremely small. The plots in Figures 4.20 - 4.27 shown inconsistence straight line which may due to the anistropic broadening effect (Smith et al., 2009). Since Eq. (2.13) is generally form of a straight line, all potential

slope are taking into consideration. Slope of the graphs obtained are equal to the lattice strain (η), observed to change in fluctuate pattern as a function of QDs size. More than one lattice strain value observed in for 0.5, 1, 5, 46 and 90 mins samples which may prior to anistropic broadening of XRD peaks and inhomogeneous lattice straining. The inhomogeneous lattice strain may relate to the inhomogeneous of Mn^{2+} in cooperation on the CdSe QDs particles interfacial (Smith et al., 2009).

Smith et al. (2009) comparing the strain parameter (percentage of lattice mismatch) of CdTe/ZnSe (core/shell) QDs and CdSe/ZnS (core/shell). CdSe/ZnS QDs shows higher percentage of lattice mismatch. They suggested due to the inhomogenity of the lattice strain since the inability of CdSe and ZnS to withstand strain without forming defects. In addition, CdSe and ZnS QDs lattice are considered less elastic compares to the CdTe and ZnSe QDs lattice when subjected to stress (Smith et al., 2009). This may add additional point to the the strain inhomogenity shown in Figures 4.20 – 4.27. In addition, interstitial of Mn^{2+} into the CdSe QDs lattice induced either compressive or/and expansion stress to the lattice, may also resulting in strain inhomogeneous in Mn-doped CdSe QDs (Devi et al., 2014).

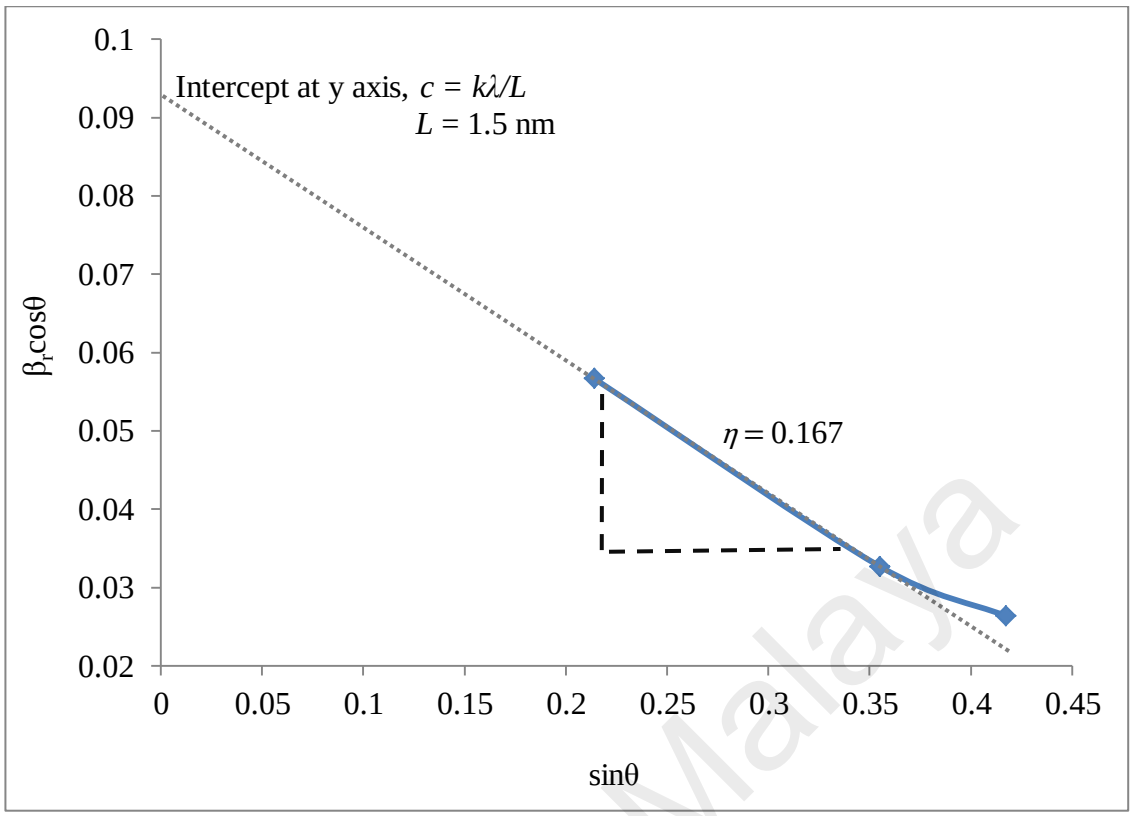

Figure 4.20: Plot of $\beta_r cos\theta$ versus $sin\theta$ from XRD data of 0 min sample

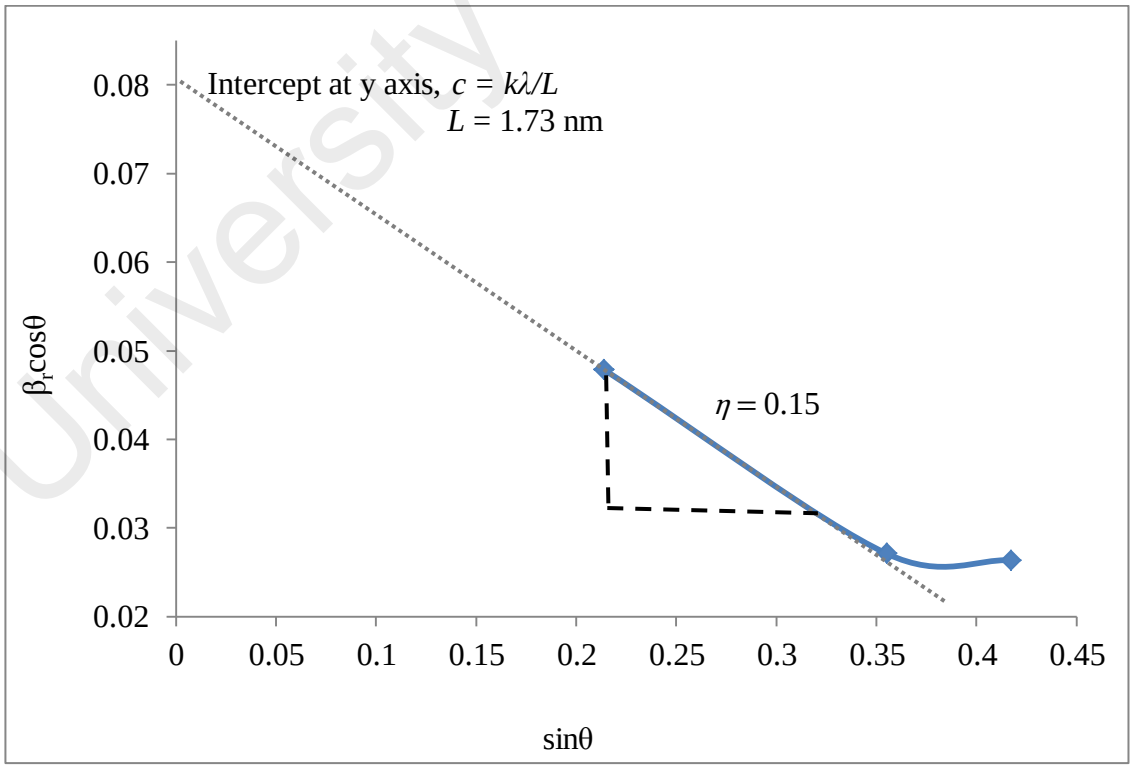

Figure 4.21: Plot of $\beta_r cos\theta$ versus $sin\theta$ from XRD data of 0.2 min sample

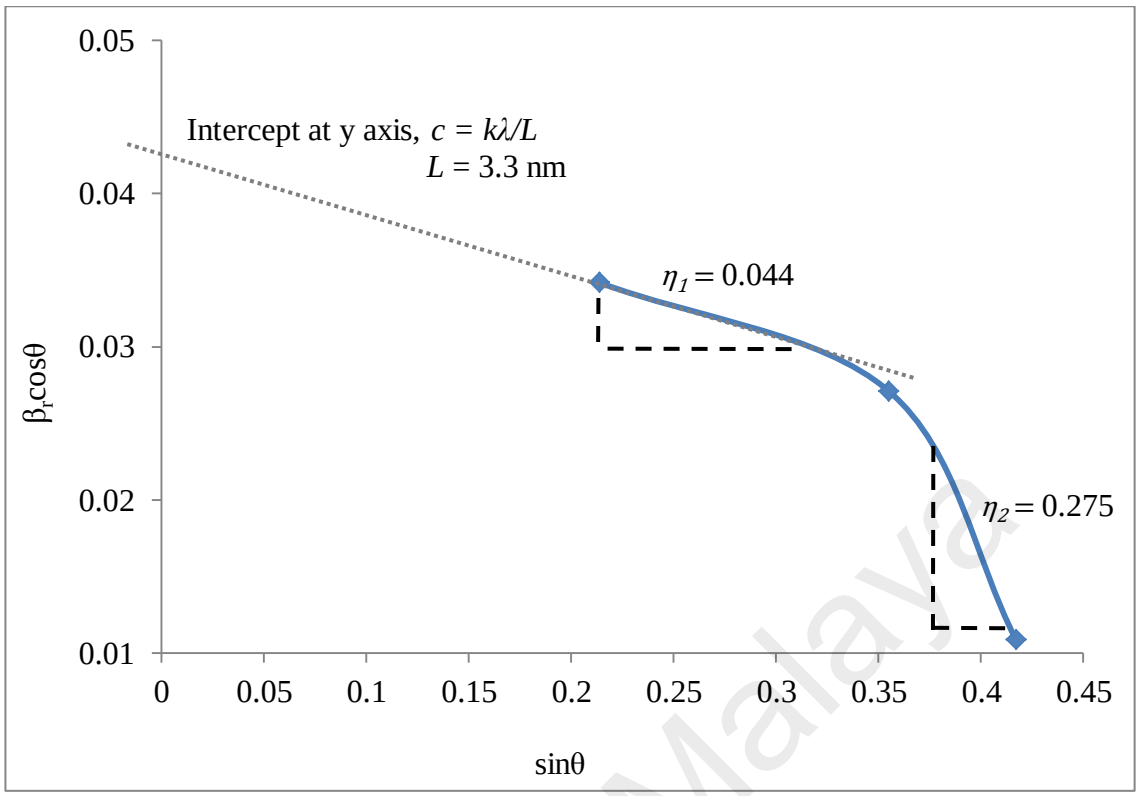

Figure 4.22: Plot of $\beta_r cos\theta$ versus $sin\theta$ from XRD data of 0.5 min sample

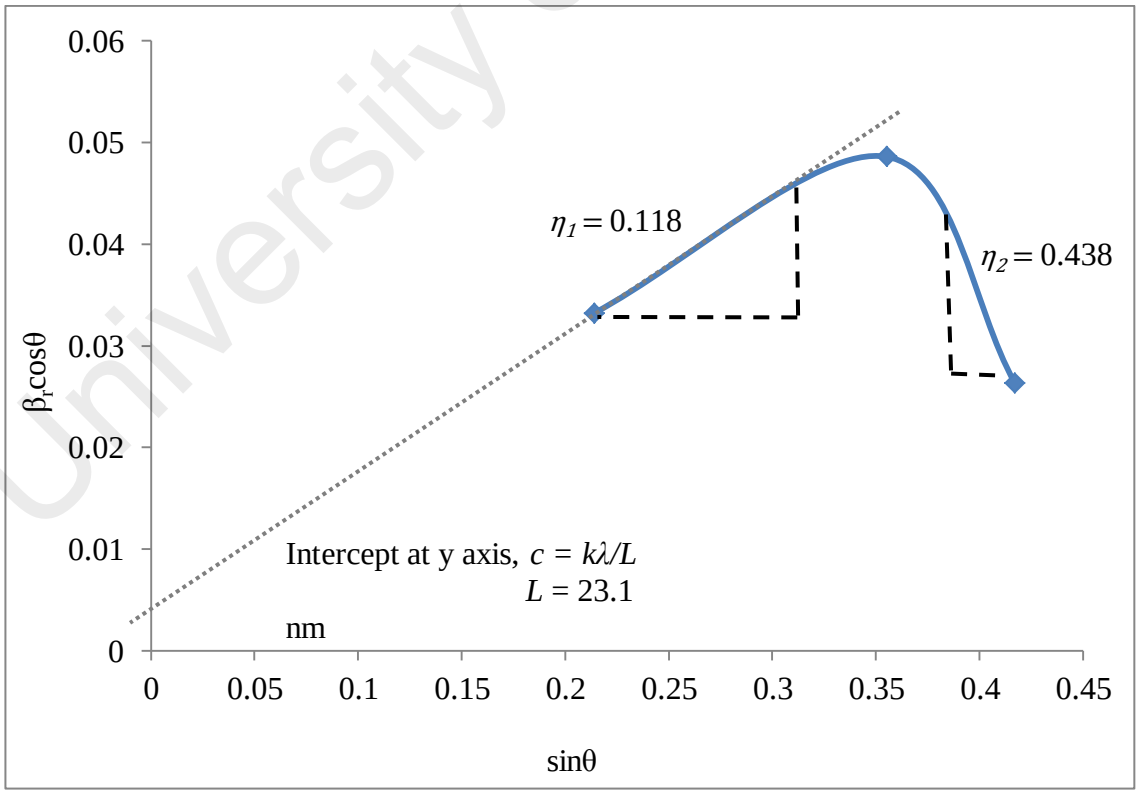

Figure 4.23: Plot of $\beta_r cos\theta$ versus $sin\theta$ from XRD data of 1 min sample

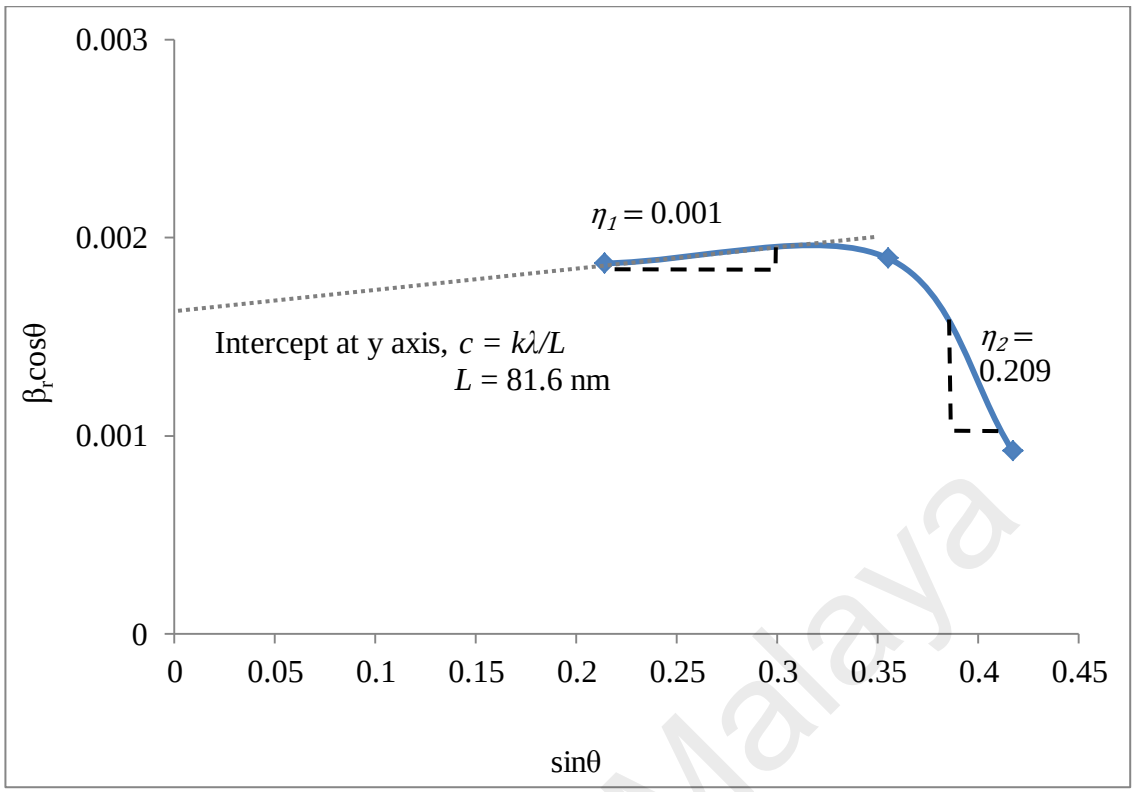

Figure 4.24: Plot of $\beta_r cos\theta$ versus $sin\theta$ from XRD data of 5 min sample

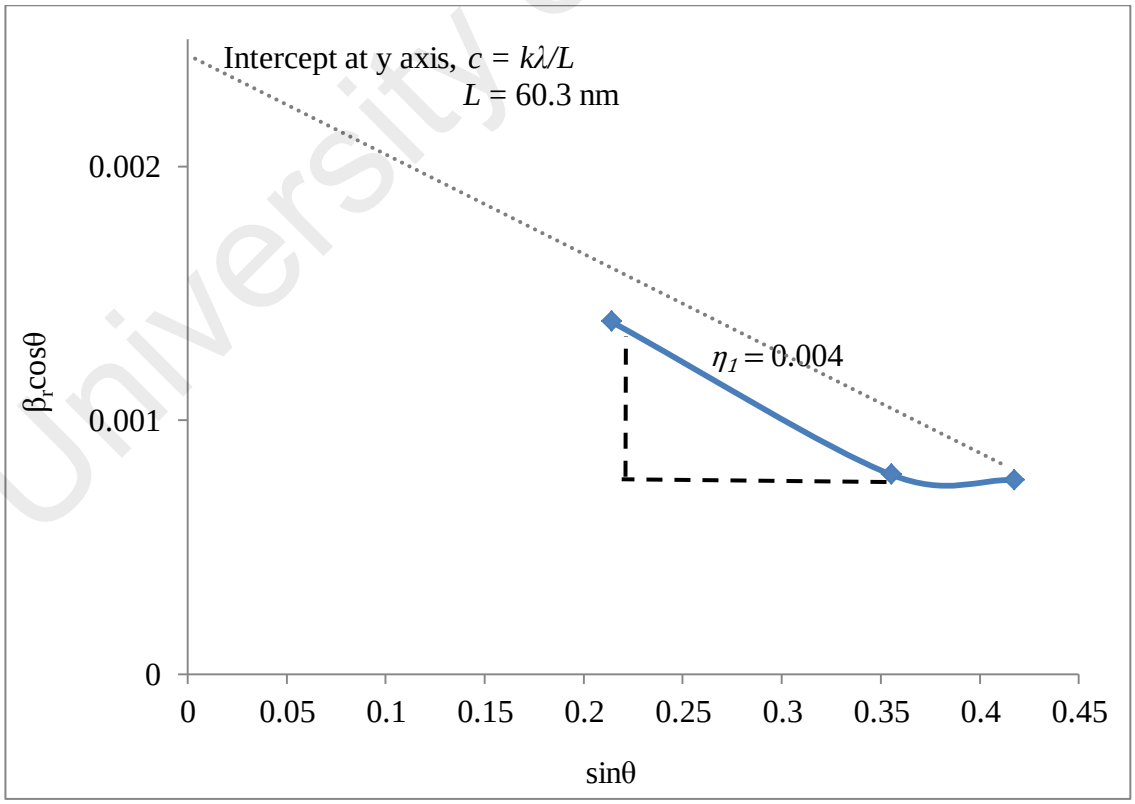

Figure 4.25: Plot of $\beta_r cos\theta$ versus $sin\theta$ from XRD data of 16 min sample

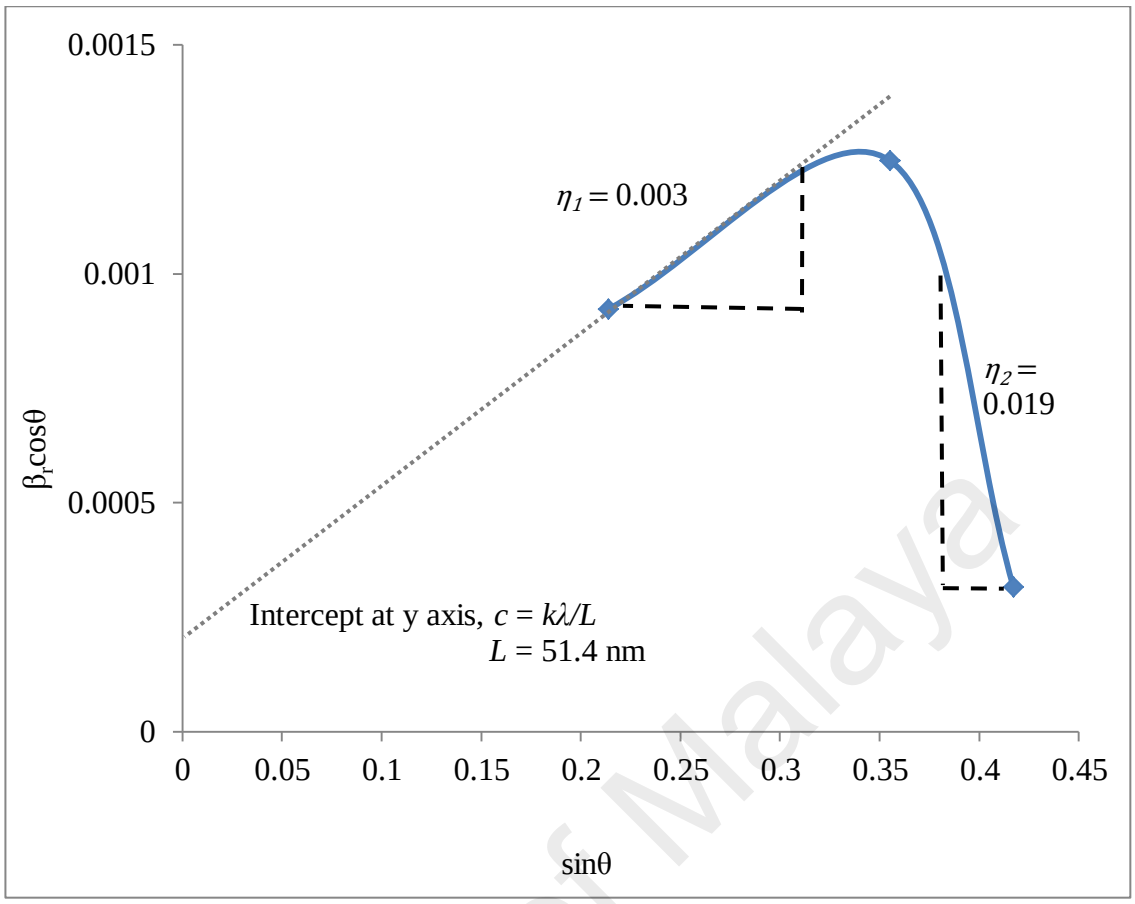

Figure 4.26: Plot of $\beta_r cos\theta$ versus $sin\theta$ from XRD data of 46 min sample

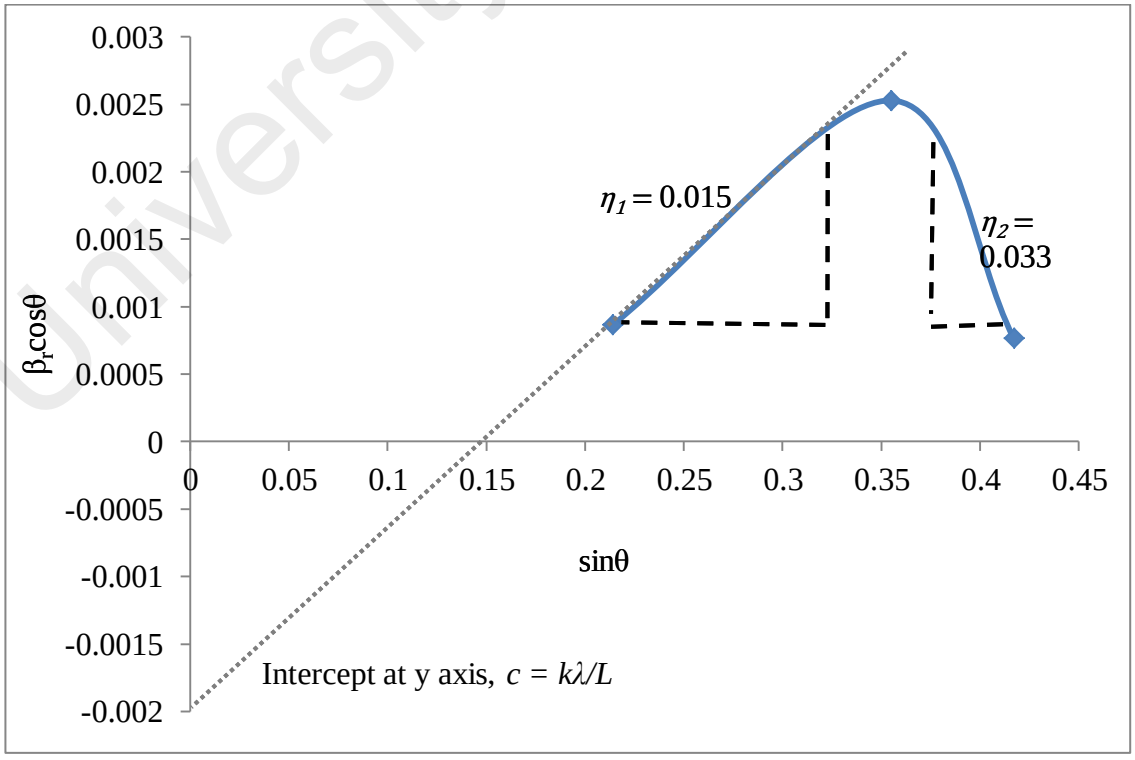

Figure 4.27: Plot of $\beta_r cos\theta$ versus $sin\theta$ from XRD data of 90 min sample

The overall lattice strain (η_1) in Figure 4.28 shows decreases patent with growth of Mn-doped CdSe QDs. The strain effect on Mn-doped CdSe QDs lattice became less prominent with QDs growth. The larger QDs required larger strain energy density to allow the lattice to be compress by stress. The strain energy density depends on the size of the QDs and the thickness of the doped shell (Gong & Kelley, 2015). CdS/CdSe (core/shell) QDs reported to possess insufficient lattice strain as the size of core CdSe increase and will reach a critical size where the uniform CdS shell growth as strain inducer are unfavorable (Gong & Kelley, 2015). In addition, Meulenberg et al., (2004) reported that ZnS shell induced large strain to significantly small CdSe core (particles size ~1.9 nm) which is nearly 1 GPa of compressive stress. This may due to the larger surface reconstruction possesses by small QDs from the strong phosphine-surface interaction (Meulenberg et al., 2004). For Mn-doped CdSe QDs system, the smaller QDs may possess larger surface reconstruction by the influence of strong surface interaction of oleate-ligand and so forth induced larger strain on the interfacial of QDs.

Despite this, the implication of strain to the Mn-doped CdSe QDs properties may not significantly affected by the value of strain since there are several other factor have to be considered, such as type of strain (compression or/and expansion), anistropic strain and Poison effect (Chen et al., 2012,; Chen et al., 2003; Jiang 2012; Thanh et al., 2014).

Crystallite size (L) values are calculated by taking the intercept value (graph tangent line and y-axis) and shows to be irrelevance to this discussion. In addition, the tangent line of 90 min samples intercept at negative value of $\beta_r cos\theta$ which prohibited the calculation of crystallite size value for this samples. Hence, this shows the

broadening of XRD peak are prominent to strain and anistropic broadening rather than crystallite size broadening which in particular to QDs size growth.

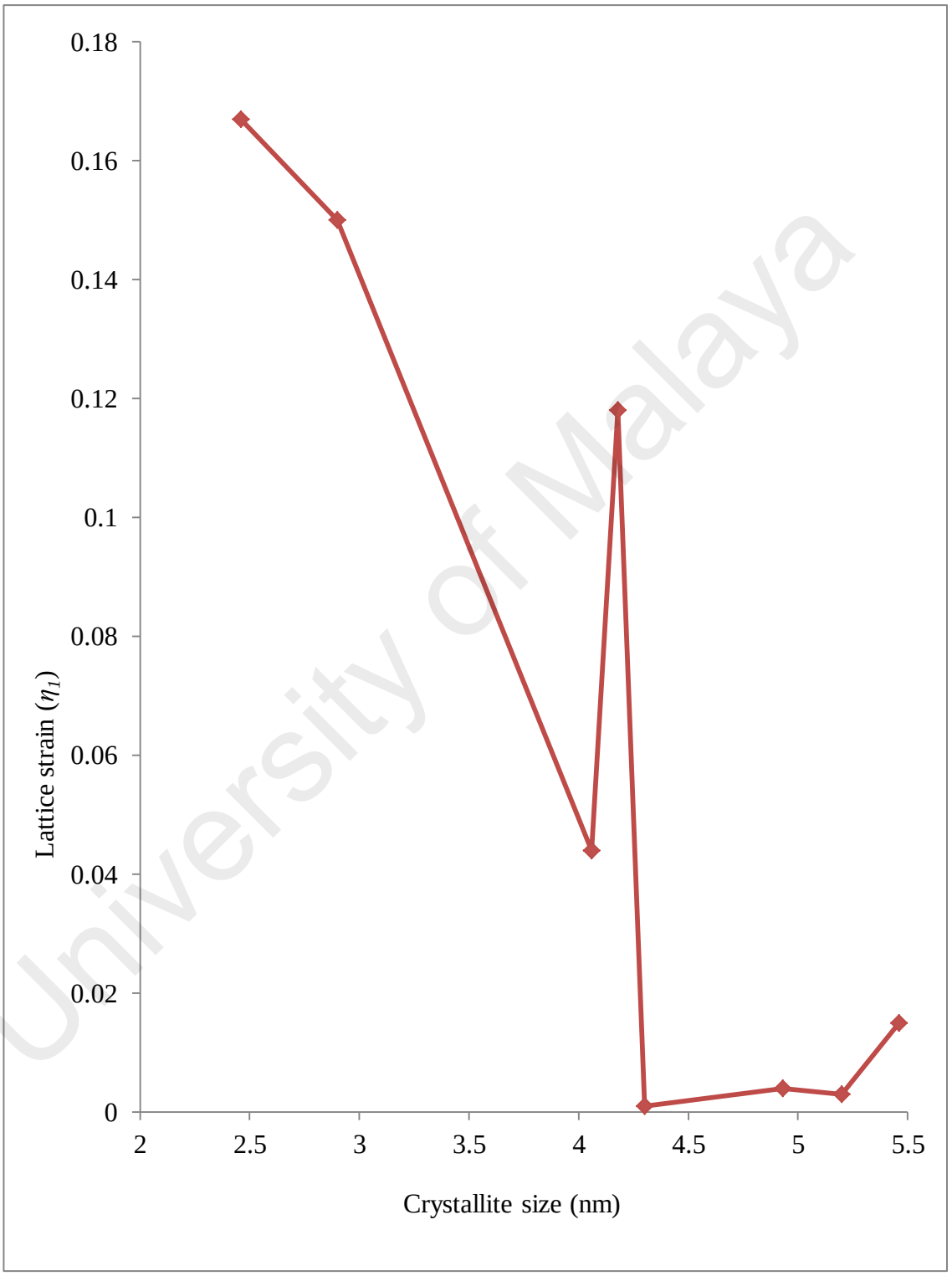

Figure 4.28: Lattice strain effect with growth of Mn-doped CdSe QDs crystallite size

Another interesting feature of XRD diffraction peak was the maximum peak intensity (I_{max}) that can be expressed in very complex equation (Jian & Hejing, 2003). In addition, I_{max} of XRD diffraction peak (Figure 4.19) is observed to be increase with QDs size decreases. This can indicate that the decrease in QDs size give essential effect on the crystal structure and phase diffraction feature such absorption of the Mn-doped CdSe QDs in a specific pattern. Other influences such instrument factor, environment and diffraction angle also contribute to the changes in I_{max} but not critical to the QDs size reduction (Jian & Hejing, 2003) . Eq. (4.1) expressed I_{max} in much more simple derivation.

$$I_{max} = |S(hkl)|^2 \times M_{hkl} \times LP(\theta) \times TF(\theta) \quad (4.1)$$

where, $S(hkl)$ is a structural factor, M_{hkl} is a multiplicity, $LP(\theta)$ is Lorentz and polarization factors and $TF(\theta)$ is the temperature factor which is precisely referred to displacement parameter (Jian & Hejing, 2003).

4.4 Ultraviolet Visible (UV-vis) Analysis

The optical properties of Mn-doped CdSe QDs are partially studied by using UV-visible spectroscopy. The absorption spectra of liquid Mn-doped CdSe QDs samples at various reaction times are illustrated in Figure 4.29. The maximum height of absorption peaks are located at wavelengths of 489, 514, 518, 528, 533, 545, 565 and 568 nm. Significant quantum confinement effect was observed through the red-shift behavior of maximum absorption peaks as the of QDs sizes change.

There is interesting to note that Mn-doped CdSe QDs shows a slight blue-shift behavior as compared with pure CdSe QDs (Hamizi & Johan, 2010), despite of it significantly larger QDs size. This may due to the doped of Mn^{2+} which leads to the introduction of lattice strain into the core (CdSe QDs) and shell (Mn-doped) interfacial. Complementary to this, the present of strain in QDs lattice can tailor the molecular band gap structure by positive strain (expansion) or negative strain (compression). The positive and negative axial strain can occur in the heterostructure of valence and conduction bands (Chen et al., 2003).

Furthermore, Mn-doped CdSe QDs were excited at significantly smaller wavelength margin (~54 nm) as compared to pure CdSe QDs (~130 nm) for 0.2 to 90 min reaction times (Hamizi & Johan 2010). This is further discussed by observing the evolution patent of excitionic energy with Mn-doped CdSe QDs size.

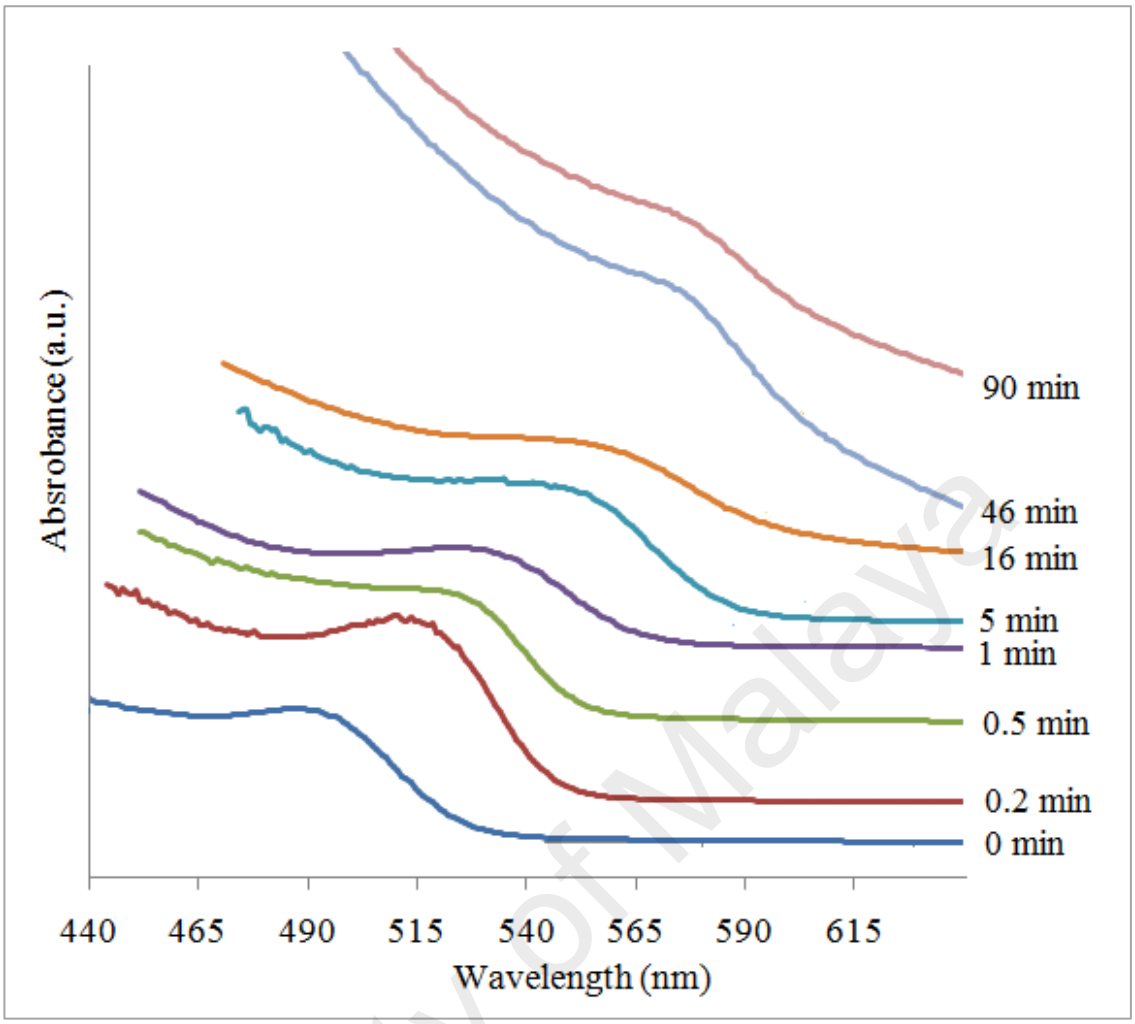

Figure 4.29: Temporal evolution of UV-vis absorption spectra for the as-synthesized Mn-doped CdSe QDs at different reaction times

This absorption peaks are result of the measured energy absorbed at certain wavelength by the excited electron to the higher energy state under the UV-visible radiation. This exciton energy has to match the energy gap between the lower and higher energy state. Tauc`s plot is used to determine the exciton energy of Mn-doped CdSe QDs by exploiting the data from absorption line obtained in Figure 4.29. The Tauc`s plot are simply derive from Eq. (4.2) (Hamizi & Johan, 2010).

$$\alpha h\upsilon = A\left(h\upsilon - E_{\mathrm{g}}\right)^{n} \tag{4.2}$$

where A is a constant, n = 1/2 for direct and n = 2 for indirect allowed transition, α is the absorption intensity and $h\upsilon = hc/\lambda$ (Mehta *et al*, 2008). The plot of $(\alpha h\upsilon)^{2/n}$ versus $h\upsilon$ shows in Figure 4.30 allowed the analysis of exicton energy evolution as a function of Mn-doped CdSe QDs sizes variation.

The exciton energy is determined by taking the intercept ion values between tangent line of Tauc`s graphs with x-axis ($h\upsilon$). The exciton energies are 2.48, 2.37, 2.35, 2.22, 2.18, 2.09, 2.05 and 2.01 eV with respect to 0 to 90 min samples. This shows the expansion of band gap energy of Mn-doped CdSe QDs in comparison with the pure CdSe QDs reported to have exciton energy ranging from 2.28 to 1.83 eV respectively for 0.2 to 90 mins samples (Hamizi & Johan, 2010). This can be another critical discussion on the lattice strain influence on the band gap structure modification in Mn-doped CdSe QDs optical and electronic properties. The lattice strain results in large lattice mismatch (%) which caused the elastic deformation by expansion of the optical band gap of Mn-doped CdSe QDs (Alahmed, 2013). Peng et al., (1997) reported a wurtzite CdSe/CdS core/shell QDs has a 3.4% bulk lattice mismatch and Talapin et al (2004) reported CdSe/ZnS core/shell QDs has a 12% lattice mismatch which in both report shows the enhancement of the the photoluminescence quantum yield and photostability up to 50% compare to the pure QDs (Peng et al., 1997; Talapin et al., 2004).

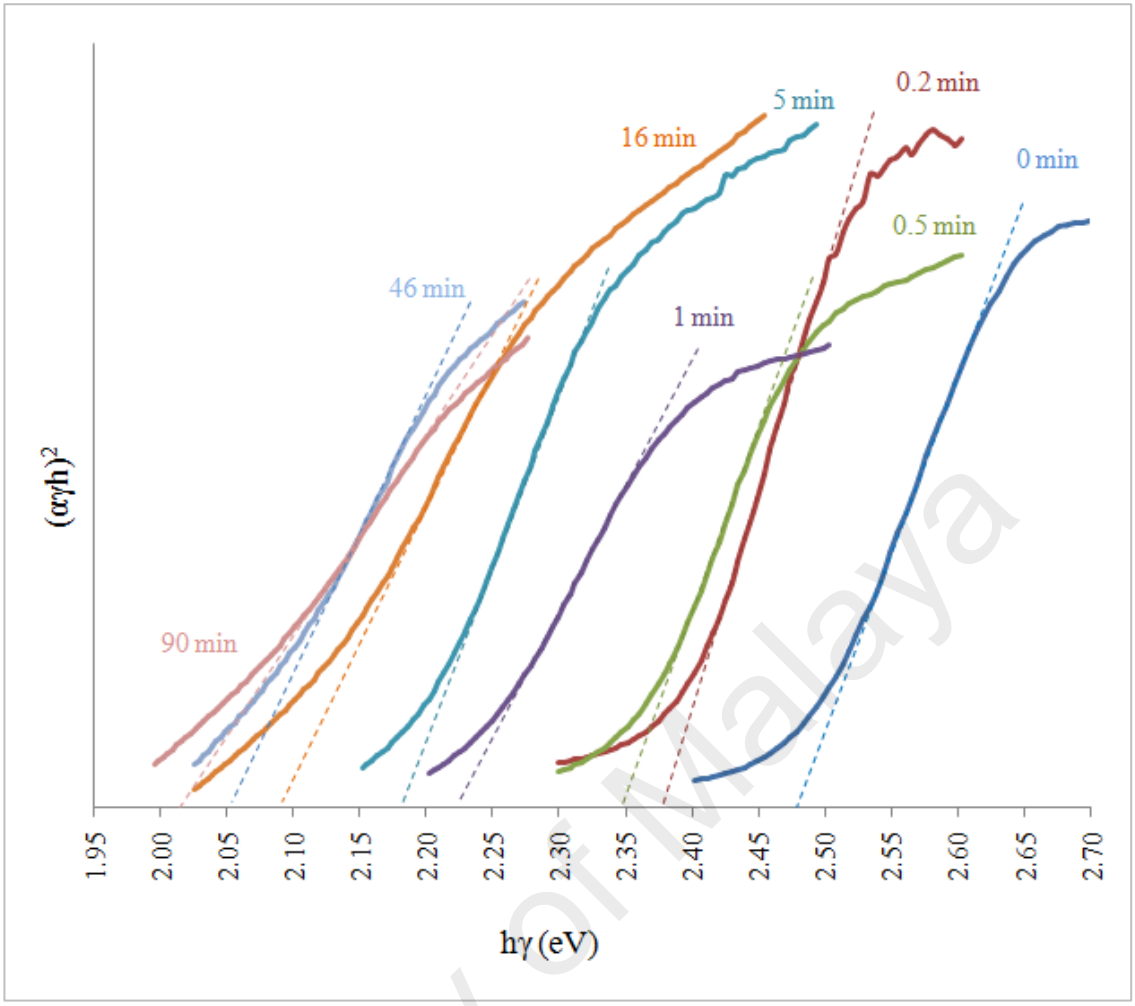

Figure 4.30: The Tauc`s plot of Mn-doped Cdse QDs at various reaction times

Moreover, Mn-doped CdSe QDs exciton energy was observed to evolve in a smaller margin (~0.35 eV) compared to pure CdSe QDs (0.45 eV) (Hamizi & Johan, 2010). As discussed earlier, the strong energy quantization can be elaborated on this narrowed exciton energy margin in the different size of Mn-doped CdSe QDs (Ren et al., 1994).

Exciton energy is a energy gap threshold of the electron and hole pair which are not physically bound but yet electrically attracted to each other which also known as electric or transport gap. While, optical band gap energy is the threshold for photons to be obsorbed (Knox, 1963). Inorganic semiconductor materials such as Mn-doped CdSe

QDs known to have small exciton binding energy which result from the insignificant interaction between electron and holes. Hence, the distinction between optical and exciton band gap theoretically small (Liang, 1970).

Thus, as an extension to the exciton energy analysis, the optical band gap energy as a function of QDs sizes are analyzed using the strong confinement model of a spherical QD given by the following equation (Gaponenko, 1998):

$$E_{1s1s} = E_g + \pi^2 \left(\frac{r_B}{r_{dot}}\right)^2 R_y^* - 1.786 \left(\frac{r_B}{r_{dot}}\right) R_y^* - 0.248 R_y^* \quad (4.3)$$

Here, r_B is the Bohr radius (CdSe QDs) = 4.9 nm, r_{dot} is the CdSe QDs crystallite radius obtained from XRD analysis, E_g is the band gap energy of bulk CdSe QDs and R_y^* is the exciton Ryberg for CdSe = 0.016 eV. Eq. (4.3) can only be applied when r_{dot} is extremely small from r_B.

The optical calculated band gap has values of 4.13, 3.44, 2.59, 2.54, 2.49, 2.30, 2.24 and 2.19 eV for 0 to 90 min samples, respectively. A broaden in optical band gap was observed compared to exciton energy. Figure 4.31 shows that the temporal evolution of exciton energy (Tauc`s plot) and optical band gap. The optical band gap behaves negatively exponential to the growth of QDs size, where as the exciton energy shows typical approximate linear relationship. The lattice strain shows crucial effect on the exciton band gap compare to optical band gap may due to the changes in the hierarchy of the ground hole state and the first excited hole states in such way that both states cross each other resulting in narrowing in exciton band gap (Phadnis et al., 2015). This wave function overlapping behavior is intensely due to the implication of strain effect on the CdS/ZnS core/shell QDs. The separation between inter-band $1s_{3/2}{}^h$ and

$1s_{1/2}{}^{h}$ decreases while for $1p_{3/2}{}^{h}$ and $1p_{1/2}{}^{h}$ increases due to shell ZnS formation. However, the $1s_{1/2}{}^{h}$ and $1p_{1/2}{}^{h}$ are crossed each induced by strain introduced by the ZnS shell. In addition, strain also induced the downward transition of $1p_{3/2}{}^{h}$ inter-band to $1s_{3/2}{}^{h}$ (Phadnis et al., 2015). This inter-band alteration induced by the lattice strain may explain the narrowing in carrier transition energy in Mn-doped CdSe QDs which results in the narrow exciton band energy.

The optical band gap of Mn-doped CdSe QDs samples possess a significantly higher energy band gap (3.44 - 2.19 eV) compared to pure CdSe QDs (2.28 - 1.83 eV) (Table 4.4). Doping of Mn into CdSe QDs increased the overall optical band gap values due to the compression of lattice parameter (table 4.1) induced by microstrain results from the incorporation of Mn^{2+} ion in CdSe QDs lattice, since lattice parameter are inversely proportional to the energy band gap value (Smith et al., 2009).

Then again, this lattice strain also may effectively increases the energy quantization in Mn-doped CdSe QDs samples which explained the small margin of band gap energy (~1.25 eV) at different QDs sizes compared to un-doped CdSe QDs (~0.45 eV) (Ren et al., 1994).

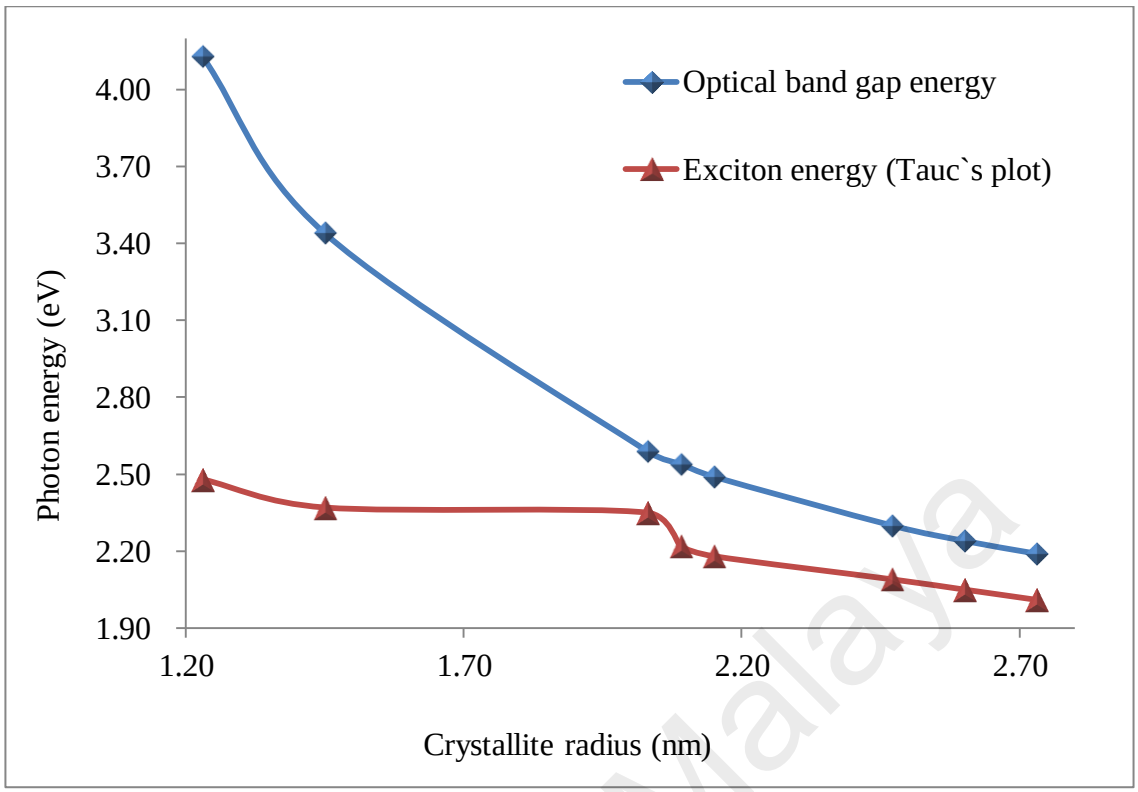

Figure 4.31: Temporal evolution of Mn-doped CdSe QD optical band gap and exciton energy against their crystallite radius

Table 4.4: The optical and exciton energy of Mn-doped CdSe QDs changes with crystallite size

Crystallite size (nm)	Optical band gap (eV)	Exciton energy
2.35	4.13	2.48
2.27	3.44	2.37
2.22	2.59	2.35
2.2	2.54	2.22
2.16	2.49	2.18
2.157	2.30	2.09
2.14	2.24	2.05
2.13	2.19	2.01

4.5 Photoluminescence (PL) Analysis

Another essential optical study of Mn-doped CdSe QDs is the PL emission spectra. Figure 4.32 shows the emission spectra of Mn-doped CdSe QDs liquid samples at various reaction times. The overall emission peaks were experienced red-shifted from 527, 546, 559, 565, 574, 575, 579 and 582 nm for 0 to 90 mins reaction times shows prominent quantum confinement effect. As predicted, Mn-doped CdSe QDs decay to lower energy level with shorter wavelength and with narrow emission wavelength margin (~ 36 nm) comparable to pure CdSe QDs with emitted with wavelength range from 546 to 719 nm for 0.2 to 90 mins with wider emission wavelength margin (~173 nm) (Hamizi & Johan, 2010). Similar phenomenon was observed in previous discussion of of blue-shifted of absorption wavelengths experienced by Mn-doped CdSe QDs samples as compared to pure CdSe QDs. This shows essential association of lattice strain to the excited and decay carrier behavior of Mn-doped CdSe QDs. The lattice strain induced by the incorporation of Mn^{2+} to the CdSe QDs lattice altered the carrier band structure by compressive stress towards its (Choi et al., 2009). This lattice strain may induced the fluorescent recombination in CdSe QDs core which the electron are delocalized throughout the QDs while the hole is confined to the core (Steiner et al., 2008; Peng et al., 1997). Choi et al., (2009) reported that the zinc blende CdSe/CdS core/shell QDs observed to have blue-shifted of PL peak induced by the strain similarly to Mn-doped CdSe QDs which may due to the increase in conduction band energy and resulting in large wavefunction overlapping (Choi et al., 2009; Wei & Zunger, 1999).

The narrow emission wavelength margin with Mn-doped CdSe QDs growth compared to pure CdSe QDs may due to the strong size and lateral quantization effect induced by the lattice strain resulting in the quantization of carrier change energy.

Hence, the band gap energy shows a typically small broadening compared to un-strained QDs (Pejova & Abay, 2011).

The increase in PL quantum efficiency is presented in terms of an increase in the PL intensity (Biju et al., 2007). The PL intensity shows fluctuated values which 1 min samples possess the higher intensity. On the other hand, the PL peaks height observed to be increase significantly with growth of Mn-doped CdSe QDs sizes. However, the PL peak height is insufficient for this discussion due to the change in FHWM of the PL peaks. Thus, PL quantum efficiency does not change will QDs growth.

The width of the PL peaks shows gradually decrease with growth of the Mn-doped CdSe QDs. The FWHM of PL peaks is 30, 25, 23, 21, 17, 8, 8 and 8 nm approximately. The particles size distribution can be express by the PL peaks width which is predicted to be broad at smaller QDs and gradually narrow down. The growth of the QDs is predicted to be in relaxation states starting at 16 to 90 min samples since there is no change in FWHM of the peak. This may due to the large total free energy posses by Mn-doped CdSe particles at the early stage and reduces gradually with reaction times. The total free energy of the QDs is induced thermodynamically and highly dependent on the saturation of ion of chemical precursor (i.e. Mn, Cd and Se) and the molar volume (Thanh et al., 2014).

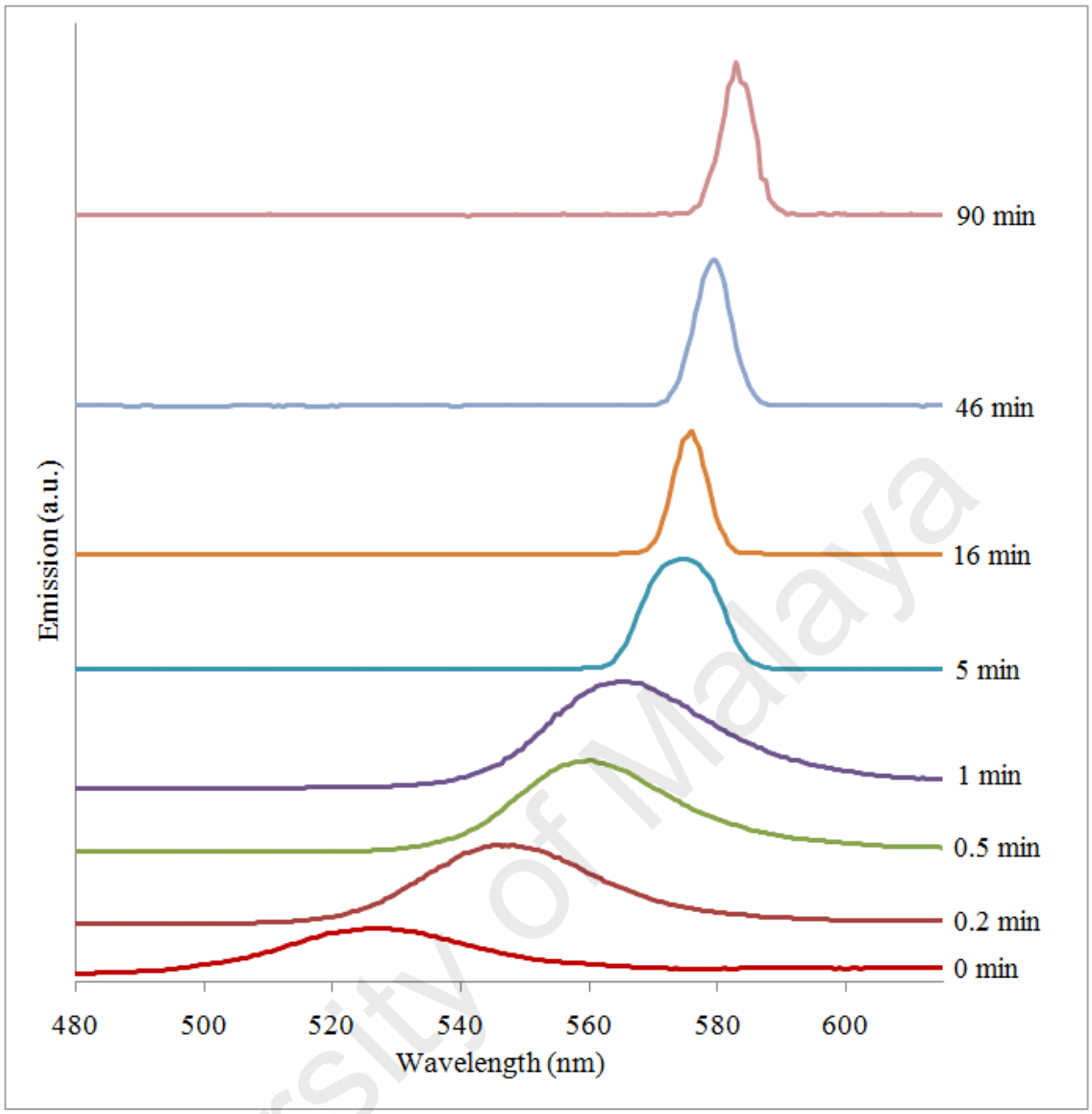

Figure 4.32: PL emission spectra of Mn-doped CdSe QDs samples

As comparison analysis, emission energy of Mn-doped Cdse QDs liquid samples were calculated using the classical energy equation (Eq. (4.4)). In this particular analysis, E is the emission energy and λ is the wavelength of maximum emission peak height. The h and c both are notable plank`s constant and light velocity constant.

$$E = \frac{hc}{\lambda} \tag{4.4}$$

Figure 4.33 shows the evolution of emission and exciton energy of Mn-doped CdSe QDs size. Neither exciton and emission energy have the exponential nor strong linear relation with QDs sizes growth. Both evolved in distinctly unique patent with QDs sizes growth. Nevertheless, exciton and emission energies typically reduced with QDs sizes growth due to a quantum confinement effect. In extent, the influence of lattice strain may induce this change in energy band structure since it shows unique evolution patent (Figure 4.34). It is ambiguous to prove which type of strain (expansion or compression) experience by lower and higher state of electron transition at this point of analysis. It has been reported that nearly all zinc blende II-VI and III-V semiconductor, introducing of compressive force will increase the electronic band gap (Maki et al., 2007), vice versa by the introduction of tensile strain which is represent by a negative deformation potential, $a < 0$ (Eq. (4.5)). Here, ΔE_{g_o} is the unstrained semiconductor band gap and $\Delta(lnV)$ is the fractional volume change (Maki et al., 2007; Persson et al., 2005).

$$a = \Delta E_{g_o} \Delta(lnV) \tag{4.5}$$

Since lattice strain induces the change in conduction band in larger degree compared to valence band (Wei & Zunger, 1999), the CdSe QDs core may experience compressive deformation as the effect of Mn-doped shell growth with reaction time that rise the energy level of conduction band. At the same time, Mn shell may experience tensile strain which leads to decrease in conduction band energy level. This double strain effect at both CdSe QDs core conduction band and Mn-doped shell conduction band respectively, results the formation of band gap heterostructures in Mn-doped CdSe QDs. This was similarly discussed by Smith et al., (2009) for CdTe-ZnSe core-shell QDs (Smith et al., 2009).

Figure 4.33 shows obvious Stoke`s shift (~0.10 – 0.13 eV) observed in 1.23 to 2.03 QDs crystallite radius. As the QDs size increases to 2.09 and 2.15, the Stoke`s shift (0.02 eV) became less prominent and observed to have nearly Rayleigh scattering. Anti-Stoke`s shift shows significant effect as the QDs size growth from 2.47 to 2.74 nm. The energy reduction rate of the conduction band became slower compared to the reduction rate of valence band energy as the size increase from 2.09 to 2.74 nm of crystallite radius which finally created anti-Stoke`s shift effect (Kmmell et al., 1998; Thanikaikarasan et al., 2011). This the modification on the energy band structure of doped QDs can be tailor by the double straining (compression or/and expansion) induced by doping of Mn^{2+} and weaken the quantum confinement effect with growth of QDs sizes (Phadnis et al., 2015; Gong et al., 2015; Chen et al., 2012).

Approximate photon energy structure of Mn-doped CdSe and pure CdSe QDs are illustrated in Figures 4.34 and 4.35. Pure CdSe QDs in overall shows Stokes effect at smaller QDs and anti-stokes effect in larger QDs which nearly similar to those observed in Mn-doped CdSe QDs. Distinctly, 90 min samples of pure CdSe QDs shows strong Stokes shift (Hamizi & Johan, 2010). Quantum confinement effect plays an important role in creating this intermediate energy states. In Mn-doped CdSe QDs system, Mn dopants provided extra carriers into the core CdSe QDs which will results in creation of this intermediate energy states as illustrated in Figure 2.24 (Huang et al., 2013).

Mn-doped CdSe QDs shows slightly larger Stokes shift (0.1 and 0.13 eV) for 0.2 and 0.5 mins samples compared to pure CdSe QDs (0.01 and 0.09 eV) (Hamizi & Johan, 2010). This may due to the zero self-quenching and ability of doped QDs to eliminate the re-absorption phenomenon which enlarging the Stokes shift compared to

pure QDs (Huang et al., 2013; Peng, 2010). Same phenomenon reported by Huang et al., (2013) which compared stokes shift of Ag-doped CdSe QDs and pure CdSe QDs (Huang et al., 2013). Interestingly, 1 and 5 mins samples of Mn-doped CdSe QDs shows reduction of Stokes shift compared to pure CdSe QDs which particularly near Rayleigh scattering and assume to be an intermediate modification of energy transition band structure from Stokes shift to anti-stokes shift.

Many reported that the anti-stokes shift affected by non-linear phenomenon of photon energy generation such as Auger or two-photon processes. They also reported that the anti-stokes PL intensity increase linearly with the excitation intensity (Yamamoto et al., 2003; Poles et al., 1999; Paskov et al., 2000; Kammerer et al., 2001; Ignatiev et al., 1999; Edamatsu et al., 2001). This linear change of intensity of both emission and excitation are also observed in 16, 46 and 90 mins samples of Mn-doped CdSe QDs significantly, which shows anti-stokes effect (Figures 4.33 and 4.34). Ignatiev et al. (1999) and Edamatsu et al, (2001) reported that the anti-stokes effect observed in self-assemble QDs (InP and GaAs) and they both assumed that holes are generated due to optical transition into deep level while electron are expose to external filed such as electric current (Ignatiev et al., 1999; Edamatsu et al., 2001).

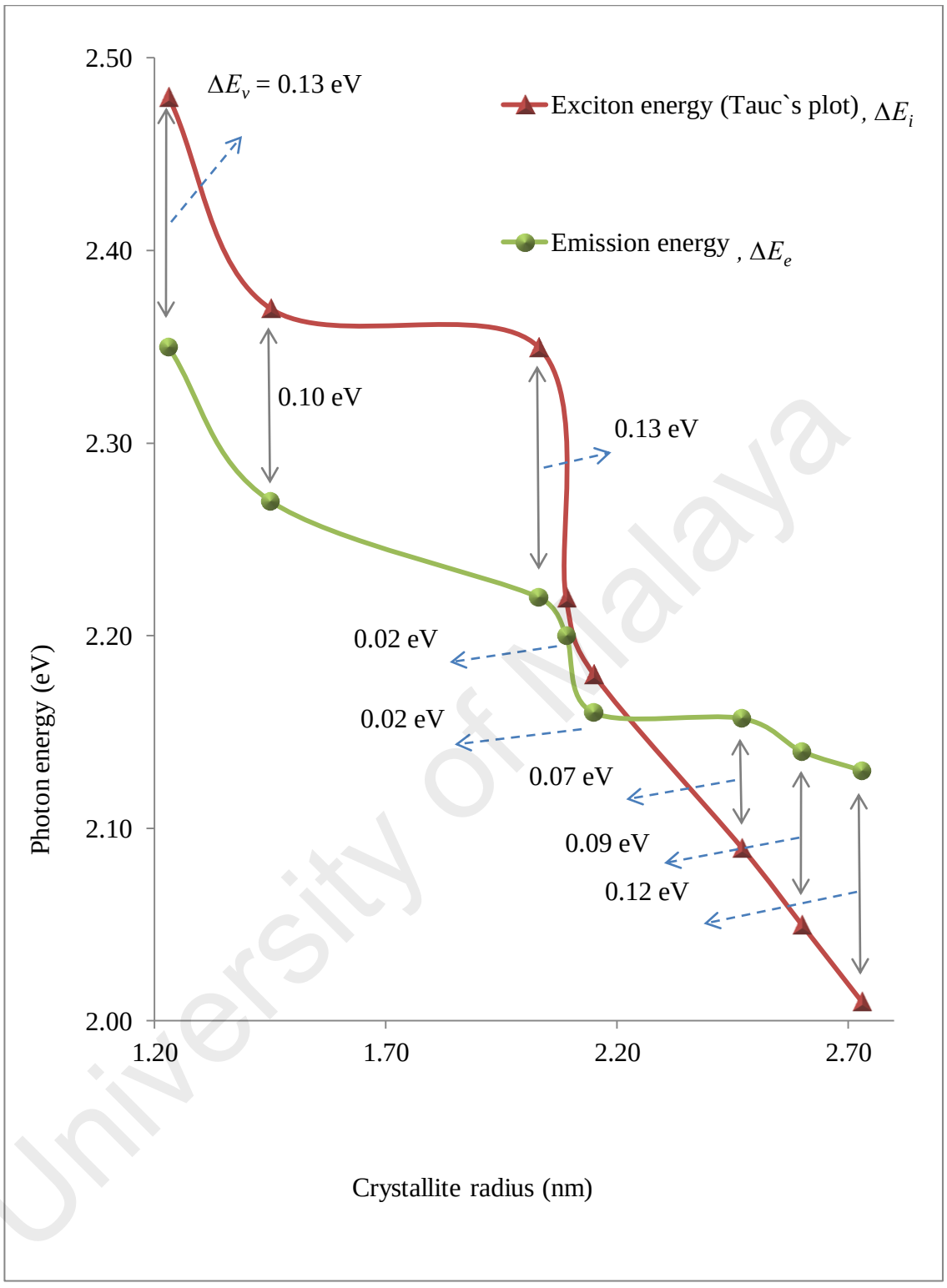

Figure 4.33: The evolution of exciton and emission energy of Mn-doped CdSe QDs various sizes

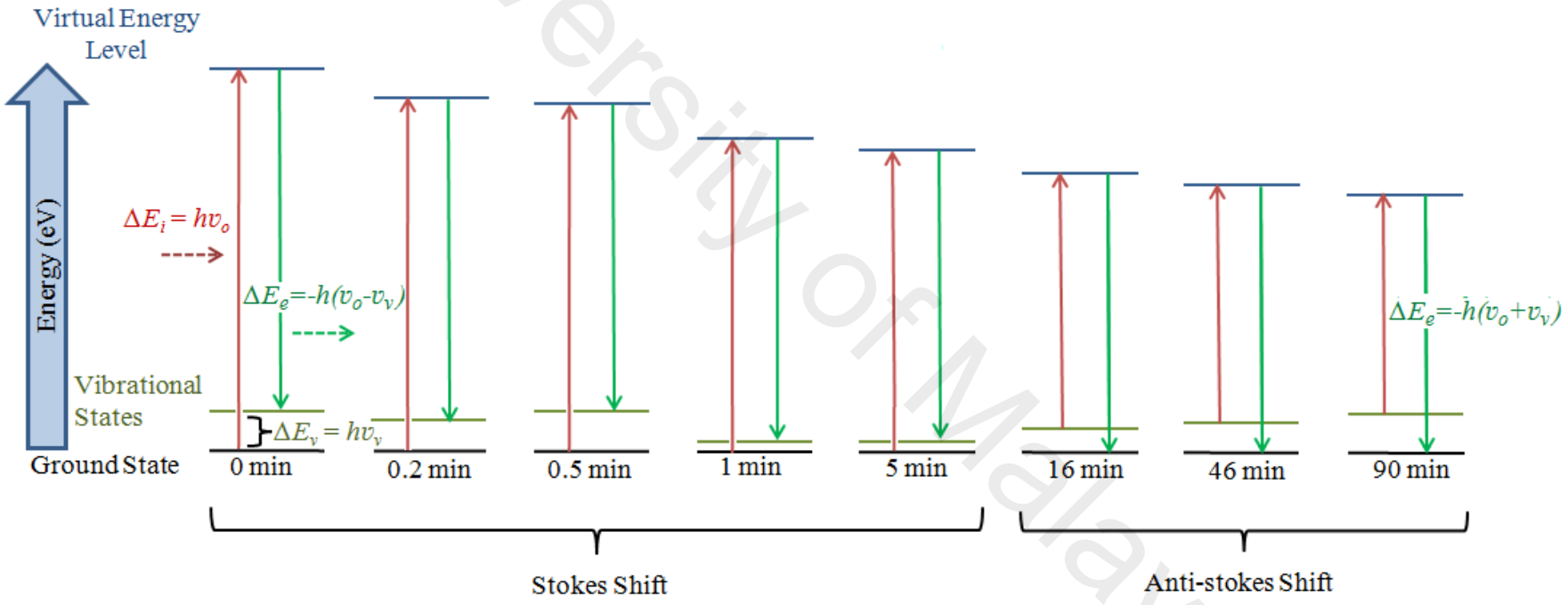

Figure 4.34: The approximation of carrier energy structure evolution of Mn-doped CdSe QDs throughout different reaction times

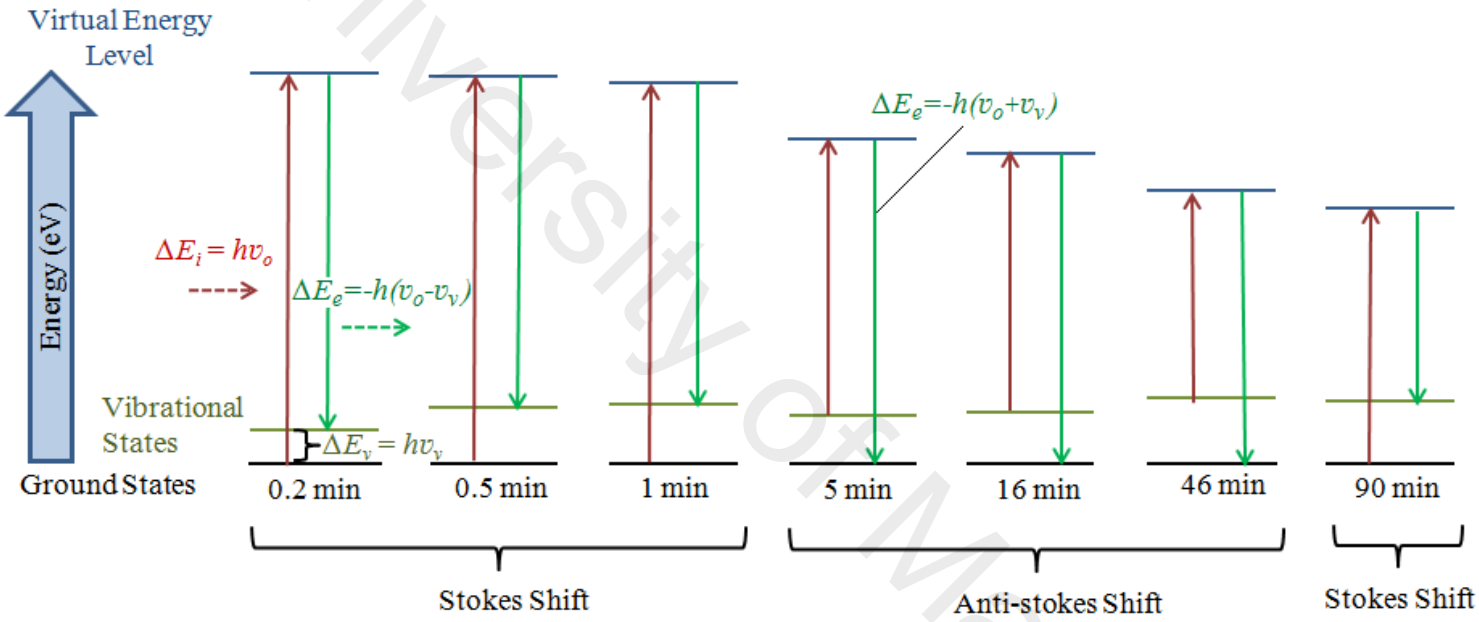

Figure 4.35: The approximation of carrier energy structure evolution of pure CdSe QDs throughout different reaction times (Hamizi & Johan, 2010)

4.6 Fourier Transform Infra-red (FTIR) Analysis

The surface analysis of Mn-doped CdSe QDs performed by observing the FTIR transmittance spectra of Mn-doped CdSe QDs samples, paraffin oil and oleic acid (Figure 4.36). Mn-doped CdSe QDs samples spectra exhibits a well defined peak of triplet band located at 2855, 2925 and 2956 cm^{-1} correspond to CH_2 stretching (sp3) which might act as surface termination of these QDs by functional groups (Deacon, et al., 1986). The band at 722 cm^{-1} corresponding to CH_2 vibrational mode (Becerra et al., 1994). The peak at 1377cm^{-1} shows the CH_3 bending in paraffin oil. C–N stretching behavior can be shown by a peak at 1463cm^{-1}. In addition, the presence of IR peak at 1712 cm^{-1} indicates the signatures of capping agent, oleic acid bounded to the surface of Mn-doped CdSe QDs. On the basis of the FTIR data, the surface of the CdSe QDs is mainly coated with oleic acid ligand. Flexible organic molecules provide repulsive interactions between the QDs in methanol, thus preventing aggregation. A small peak shifting (~0.1 – 2 cm^{-1}) towards larger wavenumber observed as the QDs sizes increase.

Small peak shift towards larger wavenumber also observed in Mn-doped CdSe QDs FTIR peaks as compared to pure CdSe QDs (Hamizi & Johan, 2010), particularly for triplet band of CH_2 stretching.

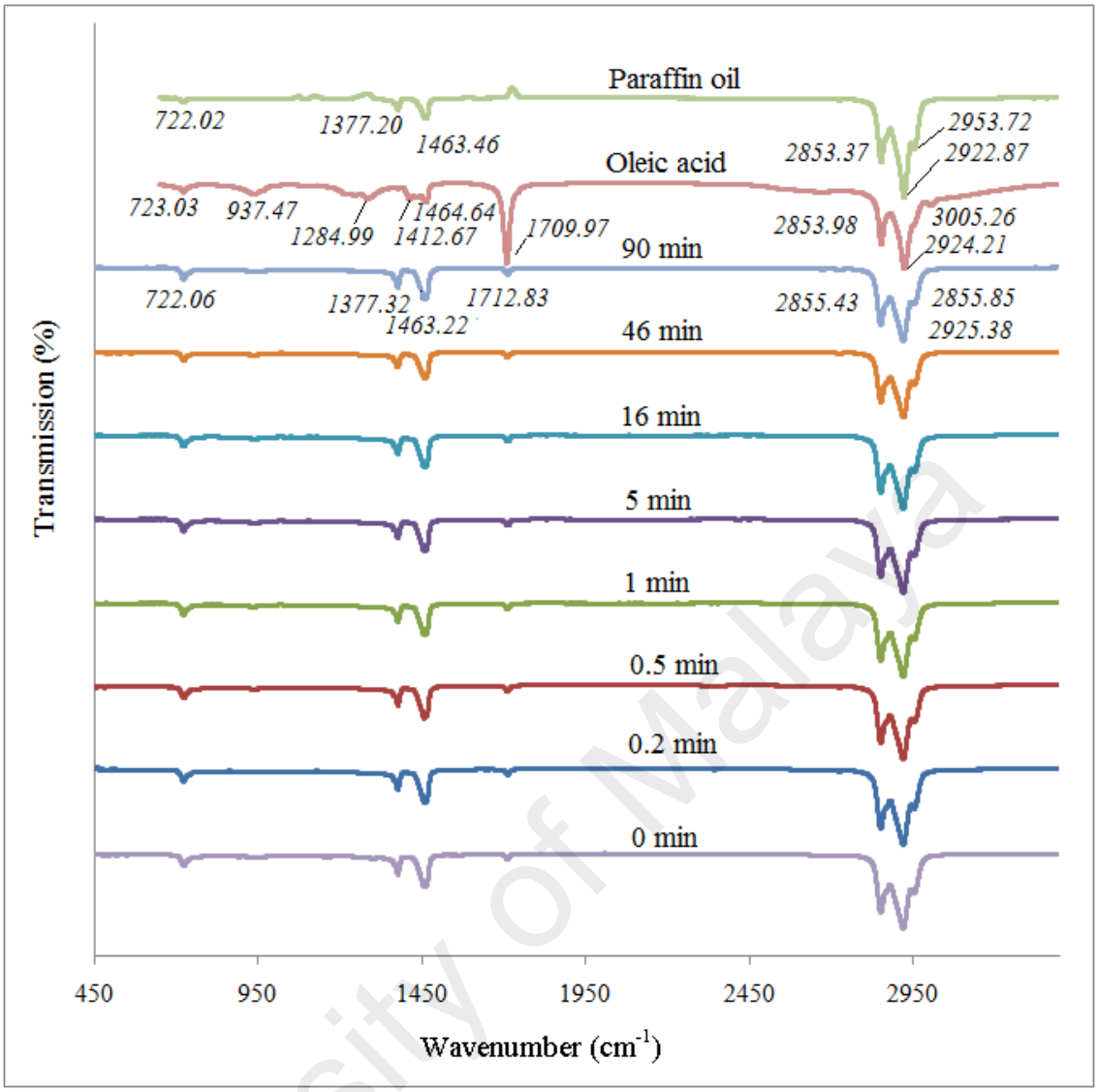

Figure 4.36: The FTIR pattern of paraffin oil, oleic acid and Mn-doped CdSe QDs at various reaction time and

4.7 Raman Spectroscopy Analysis

Further analysis on optical and vibrational properties of Mn-doped CdSe QDs various sizes are studied using Raman spectroscopy. Figure 4.37 shows the Raman spectra of Mn-doped CdSe QDs of 0 to 90 min samples. Two significant peaks were observed correspond to the scattering by the longitudinal optical (LO) of phonon and its first overtone (2LO) which located near ~ 200 and 400 cm^{-1} under an exposure of 532 nm incident laser. The LO and 2LO peaks were observed to behave red-shifted with respect to the excitation wavelength as tabulated in Table 4.4. Furthermore, the overall LO of Mn-doped CdSe QDs shows strong blue-shift compared to the LO for and pure CdSe QDs of 3.15 nm particle diameter (206 cm^{-1}) (Kelley et al., 2013) and bulk CdSe QDs (210 cm^{-1}) (Plotnichenko et al., 1977). Both of these raman-shifts are induced by phonon confinement. Furthermore, this red-shift behavior may contributed by lattice strain induced by the doping of Mn mechanism into CdSe QDs (Barglikchory et al, 2003). These two factors may also lead to the domination of anti-Stoke`s shift in highest occupied molecular orbital and lowest un-occupied molecular orbital (HOMO-LUMO) transition for 16, 46 and 90 mins samples respectively (Plotnichenko et al., 1977).

In addition, Mn-doped CdSe QDs exhibits extremely broader LO (~100 cm^{-1}) peak compared to bulk CdSe (~5 cm^{-1}) (Plotnichenko et al., 1977) which can induced by combination factor of phonon confinement, band gap structural disorder and QDs sizes distribution that are all is a function of QDs sizes growth and Mn-doped factor (Patel et al., 2014; Kelley et al., 2013).

On the other hand, there was a slight increase in LO line width as the QDs size reduced. The increment is believe to be arises from the low-wavenumber side induced

by the negative dispersion of phonon branch away from the zone-centre optical phonon as proposed in Brillouin zone (Bilz and Kress., 1979). It is also reported that the line width increases are prominent for QDs with size below 10 nm (Arora et al., 2007). This which is contradic with Mn-doped CdSe QDs raman analysis which shows of constant increase in LO line width for QDs size 11 to 14 nm (16- 90 mins) which similarly observed for QDs with below size of 10 nm.

Equally important, the peak shoulder features at low wavenumber of LO peak observed in each Raman spectra. This surface optical (SO) phonon mode are observed in wide range of QDs semiconductors which is also contributed by the phonon confinement phenomenon of LO phonon with non-zero angular momenta (Trallero et al., 1998). Then again, the Mn-doped as a lattice strain inducer can influence the formation of this SO features (Muck et al., 2004).

The intensity ratio of 2LO and LO (I_{2LO}/I_{LO}) reported to be strongly related to the electron-phonon coupling strength in QDs (Klein et al., 1990). As for Mn-doped CdSe QDs the I_{2LO}/I_{LO} not varied much change (~0.32- 0.37), which indicated that electron-phonon coupling in Mn-doped CdSe QDs were not affected much with QDs size variations (Klein et al., 1990).

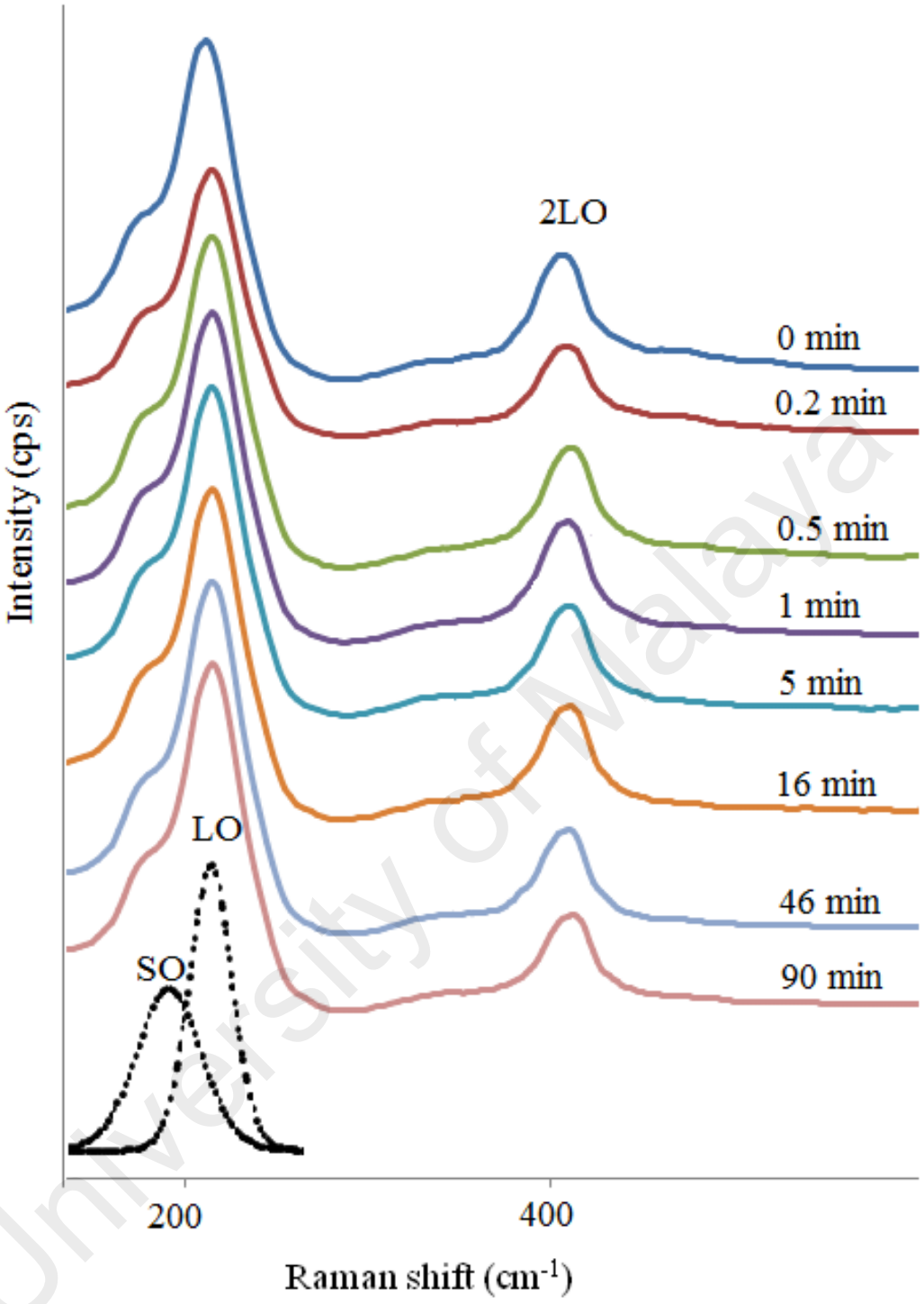

Figure 4.37: Raman scattering spectra of Mn-doped CdSe QDs at various reaction times

Table 4.5: Raman scattering parameters and excitation wavelengths for various sizes of Mn-doped CdSe QDs samples

QDs physical size (nm)	LO (cm^{-1})	2LO	I_{2LO}/I_{LO} (cps)
3	205.3	410.0	0.37
5	205.6	410.7	0.37
8	206.2	411.5	0.36
9	206.6	412.3	0.33
10	207.0	412.9	0.33
11	207.8	413.4	0.34
12	208.3	414.0	0.32
14	208.8	415.0	0.33

4.8 X-Ray Photoelectron Spectroscopy Analysis

The surface composition of Mn-doped CdSe QDs was analyzed using X-ray photoelectron spectroscopy (XPS) as shown Figure 4.38 The XPS scans traced the presence of Se 3d and Cd 3d band of CdSe crystal which having a binding energy of 54.1 and 404.5 eV (Agostenelli et al., 1989), respectively. The Mn 2p band from Mn element traced to have a binding energy of 640.7 eV (Ivanov et al., 1982) approximately, thus confirmed the presence of Mn interstitial site on the surface of CdSe QDs core act as a dope element. Figure 4.39 also shows the presence of C 1s and O 1s band which each has a binding energy of 285 and 532 eV, respectively (Dai et al., 2004).

The background correction of each XPS scan is based on C 1s (285 eV). This background correction to tailor the shift of the peak due to the retarding field at the surface of the specimen called static charging. The static charging phenomena reduce the kinetic energy of the excited electron (Dai et al., 2004).

The intensity of the C 1s and O 1s peaks observed to be remained significant in each scan, both traced elements peaks show notable intensity in each scan compared to other element band traced such as Cd 3d, Se 3d and Mn 2p that may indicate the influenced of oleic acid capping on the surface of the Mn-doped CdSe QDs, which contributed to the formation of Cd-oleate ($C_{36}H_{70}CdO_4$) and Mn-oleate ($C_{36}H_{66}MnO_4$) on the surface of QDs specifically on {001} planes. The present of Cd-oleate and Mn-oleate reduced the dangling orbitals on the surface of QDs which add the essential point of doping Mn into the CdSe QDs. These dangling orbitals is the orbitals that point away from the surface of the QDs results from the incomplete bonding because of the lower

coordination number on the surface on contrary of the interior QDs structure. In the case of CdSe QDs, both Cd and Se dangling orbitals will each act as an electron trap and hole trap, thus will trap charge carriers on the surface of CdSe QDs which lead to the decreases of quantum yield (Smith & Shuming, 2010; Pokrant & Whaley, 1999). Hence, it is assume that Mn-doped CdSe QDs will have higher florescence quantum yield disputes from pure CdSe QDs.

Furthermore, the significant C 1s peak also may associate with the existence of organic residue from solvent used, which is a paraffin that having a general chemical formula of $C_xH_{(2x+2)}$. The adsorption of adventitious carbon during the drying and handling process may add a point to observed C 1s peak (Dai et al., 2004).

Figure 4.38 not just give the information about surface elementary, it also supplied the crucial information of the kinetic and interaction between electron at certain orbital that contain un-paired electron. In initial or original state, the un-paired electron suggested to be located at 3d orbital for Cd and Se and 2p orbital for Mn for CdSe Mn-doped QDs. The spin orbital splitting may occur in the final state when the un-paired electron from ionization during the photoemission process coupled with the un-paired electron from the initial or original state at specific spin orbital (Dai et al., 2004).

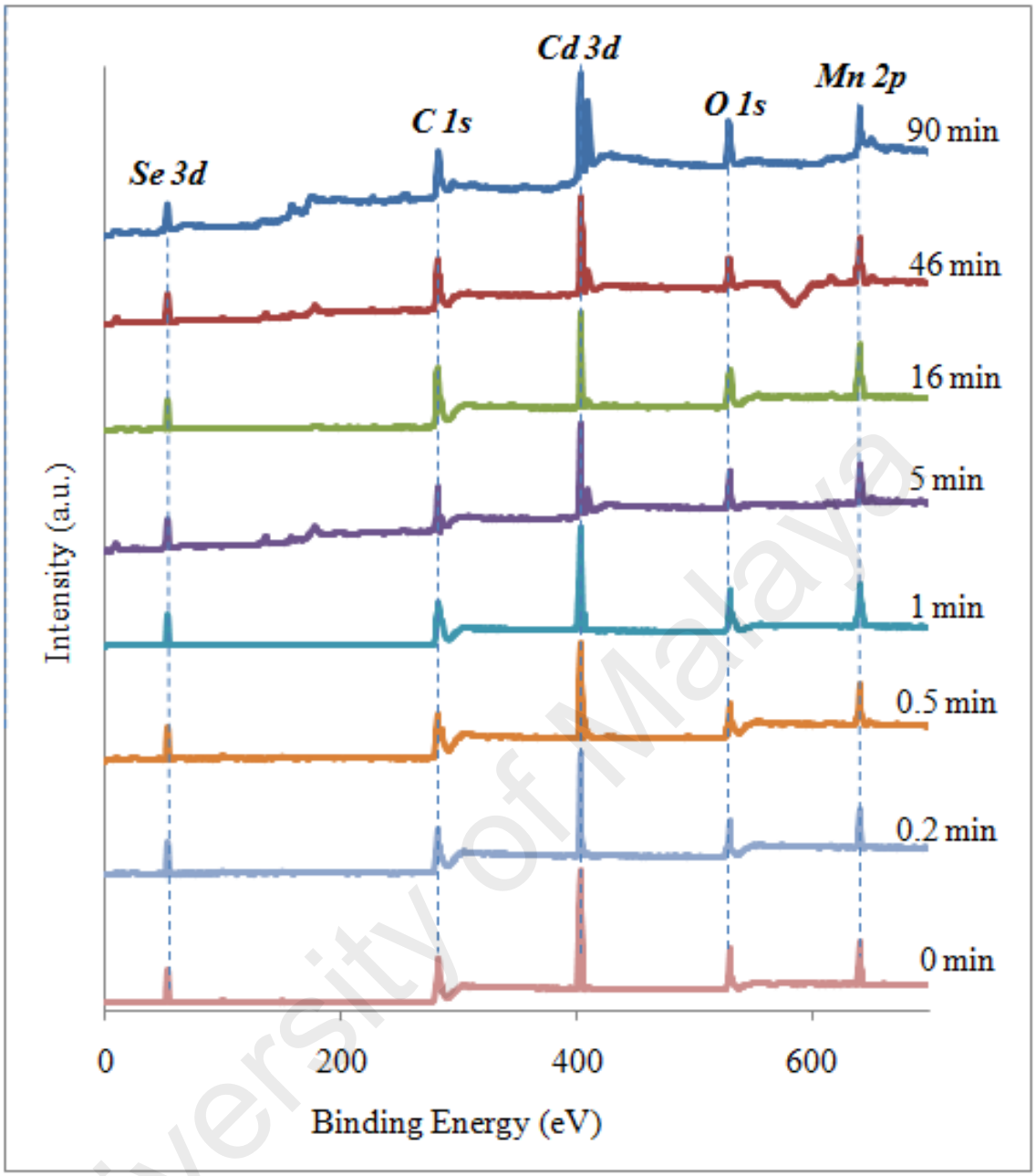

Figure 4.38: XPS wide scan of Mn-doped CdSe QDs at different reaction times

Figure 4.39 shows the Cd 3d individual peaks of Mn-doped CdSe QDs of different reaction times. The maximum peak intensity (original spectra) observed to shift towards larger binding energy as the reaction time rises. This suggests that this chemical shift is a function of size of the Mn-doped CdSe QDs (Katari et al., 1994).

Figure 4.39 also shows Cd 3d Lorentzian-Gaussian fit peaks. The Cd 3d peak is deconvoluted using a Lorentzian-Gaussian function. The Lorentzian-Gaussian fit shows the existence of Cd 3d (Lorentz fit 1) and Cd $3d_{5/2}$ (Lorentz fit 2) band which suggested that Cd is bound directly to Se at this two possible spin-orbital to form the CdSe QDs core. The Cd 3d band with a binding energy of 404.8 eV (Agostinelli et al., 1989) observed to be consistently appeared in 0-90 min XPS scan. The Cd $3d_{5/2}$ band peak fitted to have a binding energy range from 405.3 to 406.1 eV quite near to the value reported to be 405.8 eV (±2) (Gaarenstroom & Winograd,1977). The position of Lorentz fit 1 shows that Cd 3d band appeared to have consistent binding energy of 404.8 eV for each scan, where as Cd $3d_{5/2}$ (Lorentz fit 2) appeared to have slight chemical shift ranging between 405.3 to 406.1 eV.

In addition, Cd $3d_{5/2}$ band observed to appeared in Lorentz fit for 0.5, 1, 5, 16, 46 and 90 mins samples scan and not in 0 and 1 min. This suggested that 0.5, 1, 5, 16, 46 and 90 mins Mn-doped CdSe QDs have a un-paired electron at Cd 3d band with total electronic angular momentum (*j*) of 5/2 for the multiple spin orbital splitting to occurred. The values of *j* are described in Eq. (4.6).

$$j = l + s \tag{4.6}$$

where,

l = total orbital angular/ angular quantum number (>1 for p, d and f orbitals)

s = spin momenta/ spin quantum number (± ½)

Because l is larger than zero for d orbital, the orbital line have the tendency to split into doublet. For 3d orbital, the doublet will be $3d_{3/2}$ ($s = -½$) indicated that the orbital is spinning down and $3d_{5/2}$ ($s = +½$) indicated that the orbital is spinning up. Therefore, the spinning up orbital dominant in CdSe Mn-doped QDs orbital splitting system (Dai et al, 2004).

In contrary, 0 and 0.2 min samples no spin orbital interaction, therefore the energy contained in Cd 3d spin orbital are equal for both before and after the photoemission process. This suggests being due to the increase in quantum yield on the surface of atom as the size of QDs decrease to 5 nm downward.

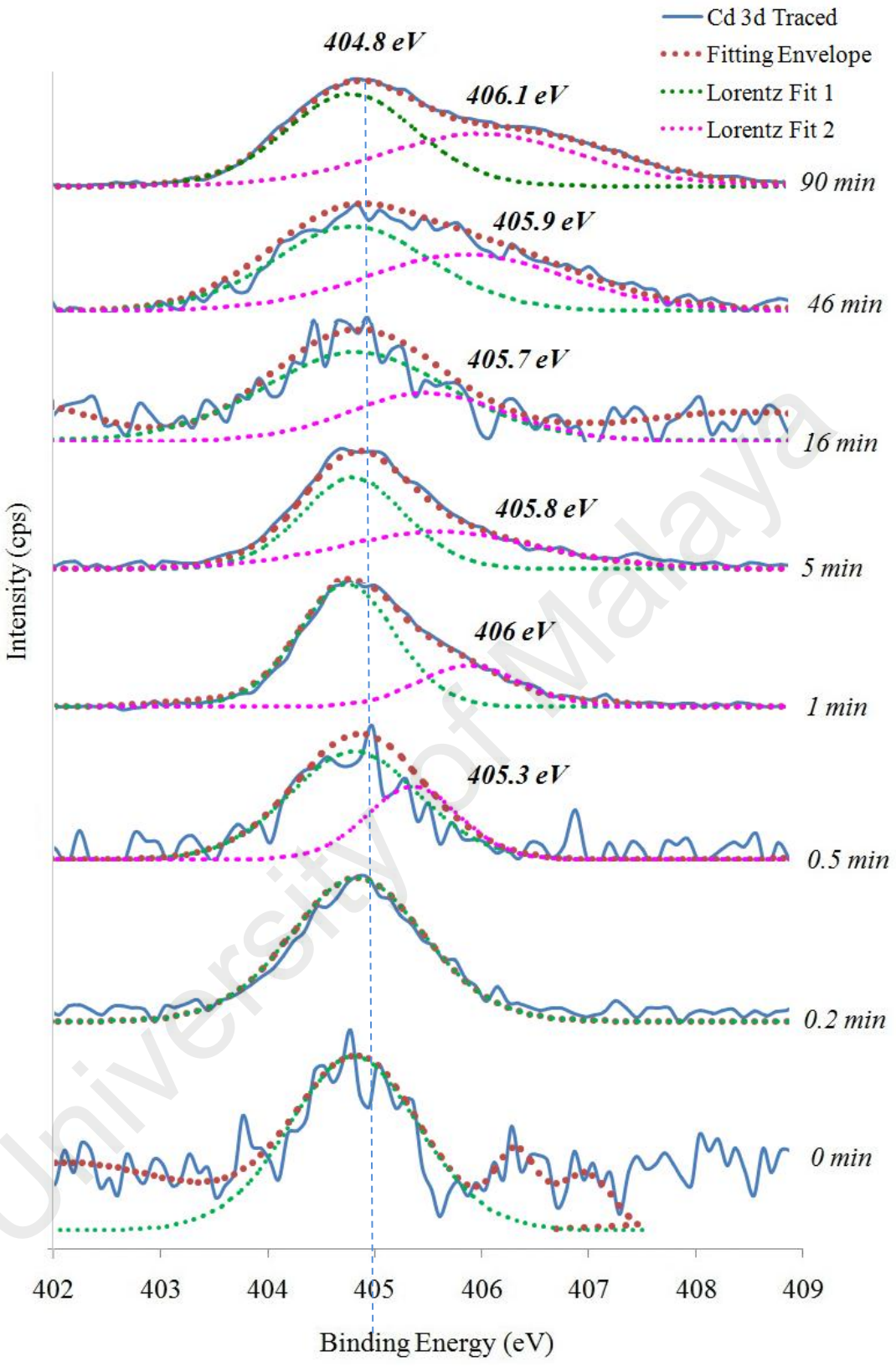

Figure 4.39: XPS scan of Cd 3d traced for Mn-doped CdSe QDs samples

Figure 4.40 shows the individual XPS peaks of Se 3d and its Lorentz fits. There is no obvious shift of original peak observed in contrary with Cd 3d results. On the other hand, the Lorentz fit 1 notice to be shift to smaller binding energy (404.2 eV) for 0 and 0.2 mins samples which also may due to the function of QDs size to the chemical shift.

Lorentz fit 2 shows distributed reading ranging from 54.9 to 56.7 eV exclude for 46 and 16 min samples. 0 min XPS spectra fitted to have extra Lorentz fit at 56.7 eV. Lorentz fit 2 and 3 indicated the influence of Se $3d_{5/2}$ band in the CdSe QDs bounding. Same elaboration as in Figure 4.10, the spinning up orbital are dominating the Se system exclude 46 and 16 mins which may due to the absence of spinning orbital interaction (Dai et al., 2004).

Interesting observation on 0 min samples Se 3d peak exhibit three Lorentz fitting features, which is 54.4 eV which correspond to Se 3d band, and 55.2 and 56.7 eV corresponds to $3d_{5/2}$ which assume to be due to the band structure complexation due to the higher density of lattice strain of core CdSe QDs where Se atom are mainly located.

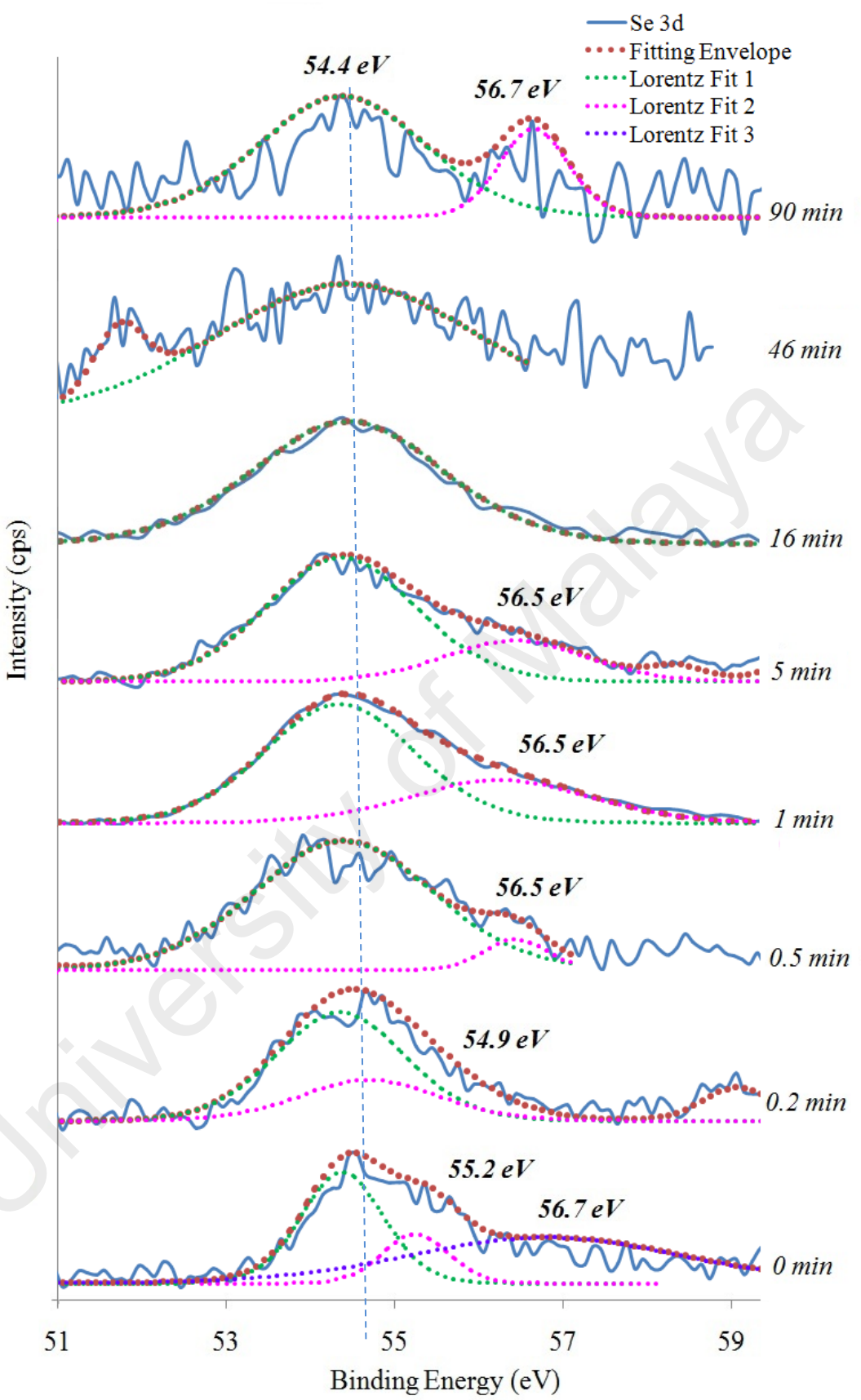

Figure 4.40: The XPS scan of Se traced for Mn-doped CdSe QDs at various reaction times

Figure 4.41 shows the Mn 2p traced having which is crucial to the point of proving the present of Mn-doped act as a shell in core-shell Mn-doped CdSe QDs samples. The Lorentz fit 1 corresponds to the Mn 2p band with binding energy of 640.7 eV is well fit in each sample.

Lorentz Fit 2 with binding energy ranging from 642.2 to 645.9 eV in each XPS scan which observed to initially created a shouldering peak and eventually shifted to create another defined peak as the QDs size increases. The roles of Mn shell as a lattice strain inducer may change with growth of QDs sizes. Moreover, the present of Lorentz fit 3 and 4 for 0 min sample give an idea of extreme changes in lattice parameter at critically small QDs which may induced by the Mn shell. In extent, the intensity of the Mn 2p peaks is declined with QDs size growth. This can due to the decrease in Mn shell thickness with QDs size growth, which related to the function of Mn ion concentration with reaction time (Dai et al., 2004).

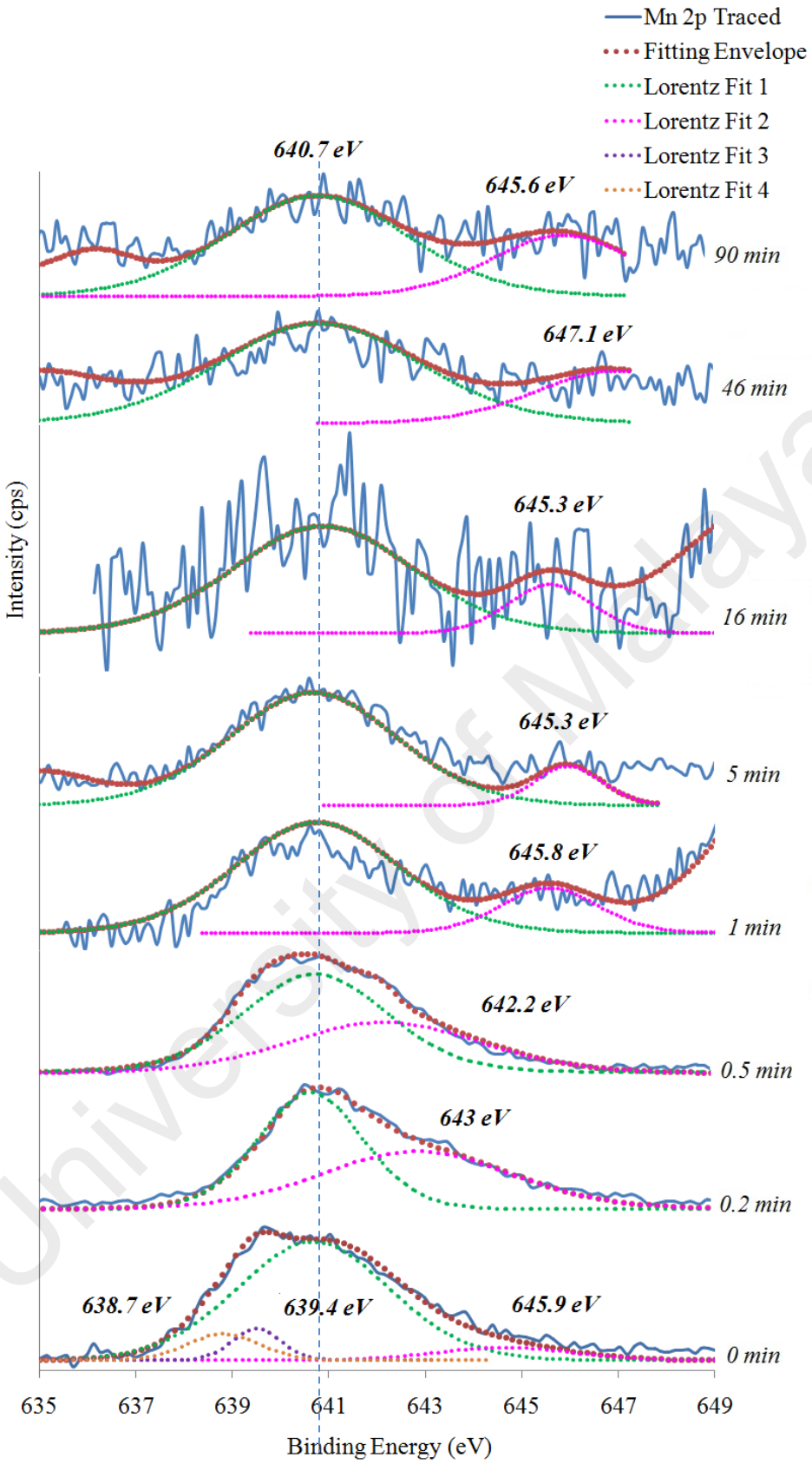

Figure 4.41: XPS scan for Mn traced for Mn-doped CdSe QDs at various reaction time

The oxidation states of excited element generally reported to be 2 for Cd, ±2, 4 and 6 for Se (Dai et al, 2004) and 7, 6, 4, 2 and 3 for Mn (Biesinger et al., 2011).

Figure 4.42 shows the relation between the Mn-doped CdSe QDs sizes with Cd 3d, Se 3d and Mn 2p XPS peak intensity. Traced Cd 3d element shows the high values of peak intensity compared to Se 3d and Mn 2p. This due to high concentration of Cd atoms on the surface of QDs that are presence as a Cd-oleate that act as ligand and Cd atoms that near to the core-shell intermediate. These also add essential idea of the role of Cd as the major electron donor in Mn-doped CdSe QDs system. The relation between the XPS peak intensity and the ion or atom concentration are strongly support by Eq. (4.7) where the electron intensity (I) presents by XPS peak are directly proportional to the concentration of the atom or ion on the samples (ρ) especially on the surface of the samples (Katari et al., 1994).

$$I = J\,\rho\,\sigma\,K\,\boldsymbol{\lambda} \tag{4.7}$$

where,

I = Electron intensity

J = Photon flux

ρ = Concentration of the atom or ion in the solid

σ = Cross-section for photoelectron production

K = Instrumental factors

$\boldsymbol{\lambda}$ = Electron attenuation length

In addition, the intensity of Cd 3d peaks observed to be decreases from 3364 to 2000 cps as the QDs size increases. This may due to the increases of electron

concentration that leave the CdSe Mn-doped QDs solid samples after been irradiated by X-ray as the sizes of QDs became smaller. The smaller QDs have a larger surface area thus, larger sample area are exposed to the x-ray resulting in higher concentration of electron emitted from the QDs surface (Dai et al., 2004). A great drop of peak intensity observed for 0 to 46 min samples and became stable at the final stage (46 and 90 mins). The influence of QDs size is less effective to the peak intensity as the size became larger than 12 nm.

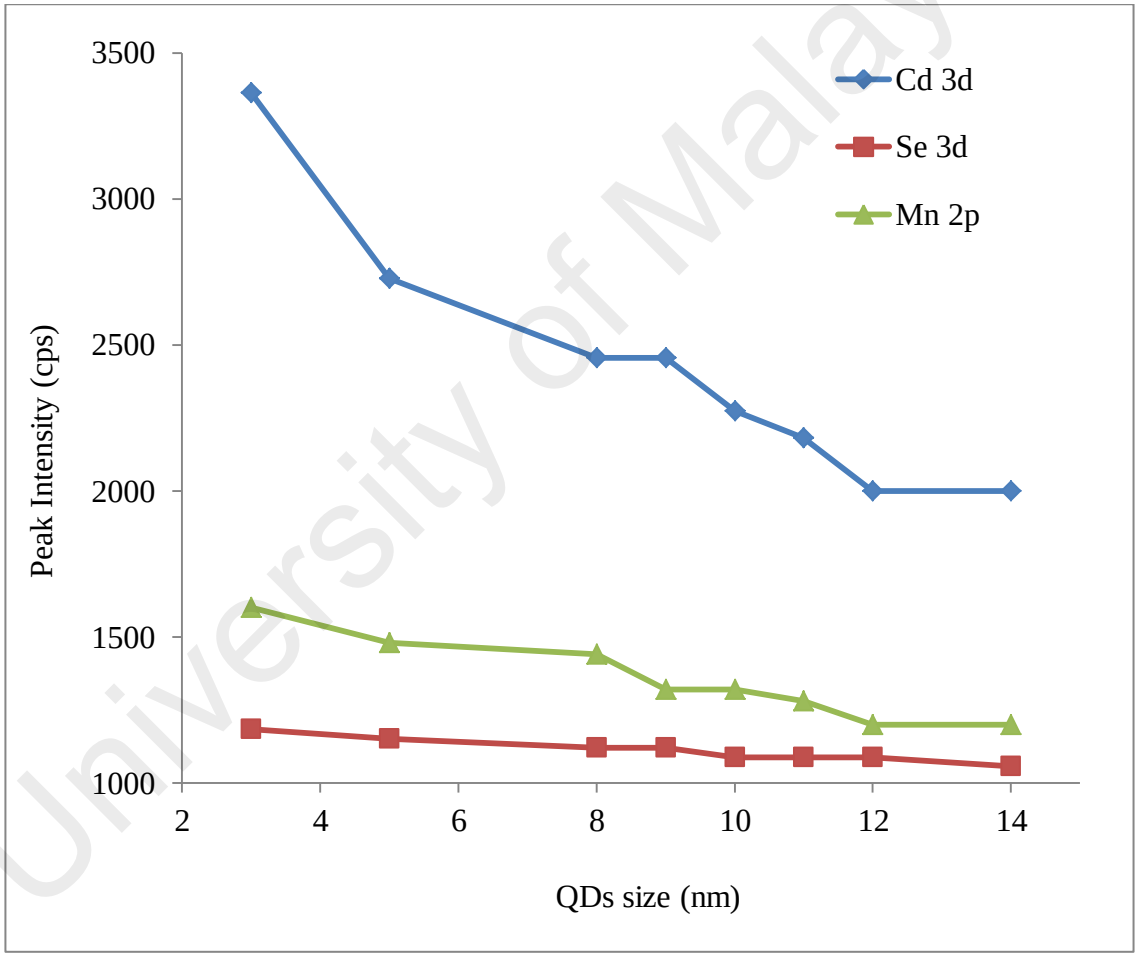

Figure 4.42: Relation between peak intensity and the variation in size of Mn-doped CdSe QDs

Another interest feature of XPS spectra is the peak broadening. Table 4.1 tabulated the full width at half maximum (FWHM) of Cd 3d, Se 3d and Mn 2p peaks.

The FWHM of Cd 3d are ranging between 1.3 to 1.5 eV for 0 to 5 min reaction time samples, but then the FWHM values shows increment patent for 16 to 90 mins samples. Se 3d and Mn 2p show FWHM values are narrowly distributed for 0 to 16 mins samples. The FWHM values measured to be rising for 46 and 90 min.

This increment patent may relative to the QDs size increment especially for Cd 3d since Cd are predicted to be the larger carrier donor at the surface of QDs. Beside, increases in energy band gap inversely proportional to the QDs. To elaborate more, Eq. (4.8) are stated to shows the relation between energy band gap (E) and the carrier effective mass (m^*) that are also inversely proportional where $\hbar$ and k are constants factors.

$$E = \frac{\hbar^2 k^2}{2m^*} \tag{4.8}$$

The charge carrier lifetime is highly depending on the charge carrier concentration since it also proportional to effective mass of carrier. Peak broadening with decrement of energy band gap may be due to the increase in carrier lifetime. Attribute to the Heisenberg's uncertainty principle (Stohr, 1992), the core-hole which created by the incident photon has a finite lifetime, which will create a broadening effect in XPS peak. This broadening is well known as natural or lifetime broadening which is also the minimum attainable peak width. The collision of Cd, Se and Mn atoms with each other whether between same or different element will create distorted energy level and resulting in a shorter lifetime of the excited state. This collision effect leads to the broadening of XPS peak (collision broadening). Both of this broadening match a Lorentzian profile (Dai et al., 2004). Table 4.6 summary the results.

Table 4.6: Full width at half maximum of XPS peak of Mn-doped CdSe QDs for different reaction times.

Reaction Time (min)	FHWM (eV)		
	Cd 3d	Se 3d	Mn 2p
0	1.5	2.2	2.3
0.2	1.4	2.2	2.2
0.5	1.3	2.6	2.3
1	1.3	2.7	2.3
5	1.3	2.6	2.4
16	2.2	2.7	2.5
46	2.5	3.6	3.0
90	2.3	4.1	5.1

A broad QDs size distribution may also lead to the XPS peak broadening. The variation of defect density due to the QDs size distribution will lead to the variations in band bending. This band bending will produced broaden peak. This discussion are supported by the QDs size distribution histogram in Chapter 4.2 that shows broad QDs size distribution in samples 46 and 90 mins samples compared to others (Dai et al., 2004).

4.9 Mechanism of Mn-doped CdSe QDs Formation

Based on the properties results and some literatures, a possible mechanism for the formation of Mn-doped CdSe QDs is suggested and summaries in Eq. (4.9) which indicated the general redox reaction for the formation of Mn-doped CdSe QDs. Firstly, when the mixture of Mn acetate, Cd oxide and oleic acid (OA) were dissolved in the paraffin oil, and leaded to 160 ºC, a light yellowish solution was produced that indicated that the formation of Mn-Cd complex (Deng et al., 2005) as shown in Eq. (4.10). Then Se was dissolved in the paraffin oil and heated to 220 ˚C through dehydrogenation reaction, a light orange then turn wine red solution was produced as shown in Eq. (4.11). Se is reduced to H_2Se gas under heating while the long alkane chain is oxidated to the long alkene chain since carbon atom in the long alkane chains acts as the reducing agent and the long alkene should be the oxidation product. When the Mn-Cd complex was mixed with H_2Se, resulting in the formation of Mn-doped CdSe nuclei as shown in Eq (4.12):

There are three possible reasons behind the formation stable homogeneous Se solution:

(1) The melting point of as-used Se powder is 217 ˚C. Thus the liquid stable of Se could be formed near or above 217 ˚C in the paraffin liquid.

(2) The liquid state of Se can be well dispersed in the paraffin liquid or other solvents with long alkane chains.

(3) H_2Se gas can be formed into alkene after heating.

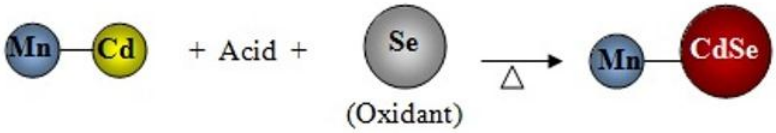

(4.9)

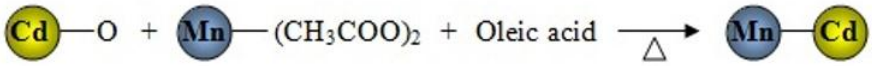

(4.10)

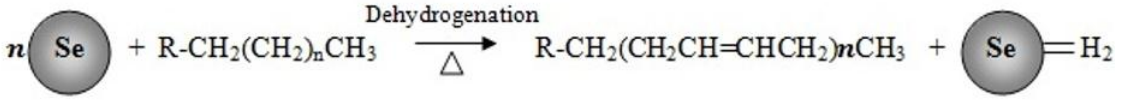

(4.11)

(4.12)

CHAPTER FIVE

CONCLUSION

Mn-doped CdSe QDs with physical size of 3 to 14 nm and crystallite size of 2.46 to 5.46 nm are successfully synthesized using inverse Micelle technique with narrow QDs size distribution and possesses quasi-sphere QDs shape. The Mn-doped CdSe QDs possesses high quality zinc blende crystal structure with tetrahedral plane (001) doped with Mn ion. The QDs size reduction shows typical blue-shift of absorption and emission wavelengths due to the quantum confinement effect. The marginal transition from HOMO-LUMO Stoke`s shift to anti-Stoke shift as the QDs physical size rose to 11 to 14 nm is prominent combination effect of lattice straining and QDs size reduction. This band gap structure modification is prominenetly effected by the introduction of lattice strain to the surface of QDs. The effect of this latice strain is observed to be highly significant at smaller QDs. FTIR spectra confirmed the oleate-capping introduced to the surface of Mn-doped CdSe QDs which act as the surface passivator which reduced the particle interfacial electron and hole trapping phenomenon. The phonon confinement observed in Mn-doped CdSe QDs from the blue-shift behavior of LO and 2LO compared to pure CdSe QDs. The surface composion of the Mn-doped CdSe QDs are shows the corporation of Mn into CdSe lattice. The introduction of strain to the lattice of the core CdSe QDs are prominently at interfacial of QDs which is highly corporate by Mn dopants. The mechanism of Mn-doped CdSe formation are purposed.

FURTHER RECOMMENDATIONS

Mn-doped CdSe QDs has shown promising tunable optical and electronic properties from this work and significant work by other researcher. Despite all this, many research gaps have to be fill in order to provide a better understanding in Mn-doped CdSe QDs system affected its properties. Therefore, for further work, it is recommended to have a rapid quenching procedure immediately after the each reaction times is over to reduce ripening effect to QDs sizes since the solution bath still under significantly high temperature near to reaction temperature after the heating process were stop. Furthermore, determination of quantum yield via PL spectroscopy are highly recommended which will significantly support the discussion and better understanding in the improvement that been contributed by Mn doping mechanism into CdSe QDs. Further study on the thickness or the density state of Mn dopant on the surface of the CdSe QDs are significant for further work since it is reported in this work that the Mn-doped induced strain to the CdSe QDs lattice hence tuned the optical inter-band structure. Intense studies on the behavior of strain apply to the CdSe QDs lattice are highly recommended by varying a strain induced parameter such as dopants concentration and location.

REFERENCES

Agostinelli, E., Battistoni, C., Fiorani, D., Mattogno, G., & Nogues, M. (1989). An XPS study of the electronic structure of the Zn x Cd 1− x Cr 2 (X= S, Se) spinel system. *Journal of Physics and Chemistry of Solids, 50*(3), 269-272.

Alahmed, Z. A. (2013). Effects of in-plane tensile strains on structural, electronic, and optical properties of CdSe. *Solid State Sciences, 21*, 11-18.

Alivisatos, A. P. (1996). Semiconductor clusters, nanocrystals, and quantum dots. *Science, 271*(5251), 933-937.

Ameen, T., Ilatikhameneh, H., Charles, J., Hsueh, Y., Chen, S., Fonseca, J., . . . Klimeck, G. (2014). *Optimization of the anharmonic strain model to capture realistic strain distributions in quantum dots.* Paper presented at the 14th IEEE International Conference on Nanotechnology.

Arora, A. K., Rajalakshmi, M., Ravindran, T., & Sivasubramanian, V. (2007). Raman spectroscopy of optical phonon confinement in nanostructured materials. *Journal of Raman Spectroscopy, 38*(6), 604-617.

Awschalom, D. D., & Kikkawa, J. M. (1999). Electron spin and optical coherence in semiconductors. *Physics Today, 52*, 33-39.

Bae, W. K., Nam, M. K., Char, K., & Lee, S. (2008). Gram-Scale One-Pot Synthesis of Highly Luminescent Blue Emitting Cd1− x Zn x S/ZnS Nanocrystals. *Chemistry of Materials, 20*(16), 5307-5313.

Bae, Y., Myung, N., & Bard, A. J. (2004). Electrochemistry and electrogenerated chemiluminescence of CdTe nanoparticles. *Nano Letters, 4*(6), 1153-1161.

Baker, S. N., & Baker, G. A. (2010). Luminescent carbon nanodots: emergent nanolights. *Angew Chem Int Ed Engl, 49*(38), 6726-6744. doi:10.1002/anie.200906623

Bakueva, L., Musikhin, S., Hines, M., Chang, T.-W., Tzolov, M., Scholes, G., & Sargent, E. (2003). Size-tunable infrared (1000–1600 nm) electroluminescence from PbS quantum-dot nanocrystals in a semiconducting polymer. *Applied physics letters, 82*(17), 2895-2897.

Balet, L. P., Ivanov, S. A., Piryatinski, A., Achermann, M., & Klimov, V. I. (2004). Inverted core/shell nanocrystals continuously tunable between type-I and type-II localization regimes. *Nano Lett., 4*, 1485-1488. Retrieved from http://dx.doi.org/10.1021/nl049146c

Balzar, D. (1999). Voigt-function model in diffraction line-broadening analysis. *International Union of Crystallography Monographs on Crystallography, 10*, 94-126.

Bang, J., Yang, H., & Holloway, P. H. (2006). Enhanced and stable green emission of ZnO nanoparticles by surface segregation of Mg. *Nanotechnology, 17*(4), 973.

Battaglia, D., & Peng, X. (2002). Formation of high quality InP and InAs nanocrystals in a noncoordinating solvent. *Nano Letters, 2*(9), 1027-1030.

Beaulac, R., Schneider, L., Archer, P. I., Bacher, G., & Gamelin, D. R. (2009). Light-induced spontaneous magnetization in doped colloidal quantum dots. *Science, 325*(5943), 973-976.

Becerra, L. R., Murray, C. B., Griffin, R. G., & Bawendi, M. G. (1994). Investigation of the surface morphology of capped CdSe nanocrystallites by 31P nuclear magnetic resonance. *The Journal of chemical physics, 100*(4), 3297-3300.

Bera, D., Qian, L., Sabui, S., Santra, S., & Holloway, P. H. (2008). Photoluminescence of ZnO quantum dots produced by a sol–gel process. *Optical Materials, 30*(8), 1233-1239.

Bera, D., Qian, L., Tseng, T.-K., & Holloway, P. H. (2010). Quantum Dots and Their Multimodal Applications: A Review. *Materials, 3*(4), 2260. Retrieved from http://www.mdpi.com/1996-1944/3/4/2260

Bera, D., Yang, H., & Holloway, P. (2006). Efficient and photostable ZnS-passivated CdS: Mn quantum dots. *ECS Transactions, 3*(5), 5-17.

Bhargava, R. N., Gallagher, D., Hong, X., & Nurmikko, A. (1994). Optical properties of manganese-doped nanocrystals of ZnS. *Phys. Rev. Lett., 72*, 416-419. Retrieved from http://dx.doi.org/10.1103/PhysRevLett.72.416

Biju, V., Kanemoto, R., Matsumoto, Y., Ishii, S., Nakanishi, S., Itoh, T., . . . Ishikawa, M. (2007). Photoinduced photoluminescence variations of CdSe quantum dots in polymer solutions. *The Journal of Physical Chemistry C, 111*(22), 7924-7932.

Bilz, H., & Kress, W. (1979). Springer Series in Solid State Sciences.

Bockris, J. O. M., & Reddy, A. K. N. (1970). *Modern Electrochemistry*.

Brennan, J. G., Siegrist, T., Carroll, P. J., Stuczynski, S. M., Reynders, P., Brus, L. E., & Steigerwald, M. L. (1990). Bulk and nanostructure Group II-VI compounds from molecular organometallic precursors. *Chemistry of Materials, 2*(4), 403-409. doi:10.1021/cm00010a017

Bruchez, M. J., Moronne, M., Gin, P., Weiss, S., & Alivisatos, A. P. (1998). Semiconductor nanocrystals as fluorescent biological labels. *Science, 281*(5385), 2013-2016.

Brus, L. (1986). Electronic wave functions in semiconductor clusters: experiment and theory. *The Journal of Physical Chemistry, 90*(12), 2555-2560. doi:10.1021/j100403a003

Brus, L. (2008). Noble Metal Nanocrystals: Plasmon Electron Transfer Photochemistry and Single-Molecule Raman Spectroscopy. *Accounts of Chemical Research, 41*(12), 1742-1749. doi:10.1021/ar800121r

Brus, L. E. (1983). A simple model for the ionization potential, electron affinity, and aqueous redox potentials of small semiconductor crystallites. *J. Chem. Phys., 79*, 5566-5571. Retrieved from http://dx.doi.org/10.1063/1.445676

Brus, L. E. (1984). Electron-electron and electron-hole interactions in small semiconductor crystallites: The size dependence of the lowest excited electronic state. *Chemical Physics, 80,* 4403-4409. doi:10.1063/1.447218

Bryan, J. D., & Gamelin, D. R. (2005). Doped semiconductor nanocrystals: synthesis, characterization, physical properties, and applications. *Prog. Inorg. Chem, 54*, 47-126.

Bullen, C. R., & Mulvaney, P. (2004). Nucleation and Growth Kinetics of CdSe Nanocrystals in Octadecene. *Nano Letters, 4*(12), 2303-2307. doi:10.1021/nl0496724

Burda, C., Chen, X., Narayanan, R., & El-Sayed, M. A. (2005). Chemistry and properties of nanocrystals of different shapes. *Chemical reviews, 105*(4), 1025-1102.

Canham, L. T. (1990). Silicon quantum wire array fabrication by electrochemical and chemical dissolution of wafers. *Applied Physics Letters, 57*(10), 1046-1048. doi:doi:http://dx.doi.org/10.1063/1.103561

Canham, L. T. (2007). Nanoscale semiconducting silicon as a nutritional food additive. *Nanotechnology, 18*(18), 185704. Retrieved from http://stacks.iop.org/0957-4484/18/i=18/a=185704

Cao, L., Wang, X., Meziani, M. J., Lu, F., Wang, H., Luo, P. G., . . . Sun, Y. P. (2007). Carbon dots for multiphoton bioimaging. *J Am Chem Soc, 129*(37), 11318-11319. doi:10.1021/ja073527l

Cao, Y.-W., & Banin, U. (1999). Synthesis and Characterization of InAs/InP and InAs/CdSe Core/Shell Nanocrystals. *Angewandte Chemie International Edition, 38*(24), 3692-3694. doi:10.1002/(SICI)1521-3773(19991216)38:24<3692::AID-ANIE3692>3.0.CO;2-W

Castro, S. L., Bailey, S. G., Raffaelle, R. P., Banger, K. K., & Hepp, A. F. (2003). Nanocrystalline Chalcopyrite Materials (CuInS2 and CuInSe2) via Low-Temperature Pyrolysis of Molecular Single-Source Precursors. *Chemistry of Materials, 15*(16), 3142-3147. doi:10.1021/cm034161o

Chason, E., Picraux, S., Poate, J., Borland, J., Current, M., De la Rubia, T. D., . . . Magee, C. (1997). Ion beams in silicon processing and characterization. *Journal of applied physics, 81*(10), 6513-6561.

Chen, H.-Y., Maiti, S., Nelson, C. A., Zhu, X., & Son, D. H. (2012). Tuning Temperature Dependence of Dopant Luminescence via Local Lattice Strain in Core/Shell Nanocrystal Structure. *The Journal of Physical Chemistry C, 116*(44), 23838-23843.

Chen, H. S., Wang, S. J. J., Lo, C. J., & Chi, J. Y. (2005). White-light emission from organics-capped ZnSe quantum dots and application in white-light-emitting diodes. *Applied Physics Letters, 86*(13), 131905.

Chen, X., Hutchison, J. L., Dobson, P. J., & Wakefield, G. (2009). Highly luminescent monodisperse CdSe nanoparticles synthesized in aqueous solution. *Journal of materials science, 44*(1), 285-292.

Chen, X., Lou, Y., Samia, A. C., & Burda, C. (2003). Coherency strain effects on the optical response of core/shell heteronanostructures. *Nano Letters, 3*(6), 799-803.

Chen, Y., Li, S., Huang, L., & Pan, D. (2013). Green and facile synthesis of water-soluble Cu–In–S/ZnS core/shell quantum dots. *Inorganic chemistry, 52*(14), 7819-7821.

Choi, C. L., Koski, K. J., Sivasankar, S., & Alivisatos, A. P. (2009). Strain-dependent photoluminescence behavior of CdSe/CdS nanocrystals with spherical, linear, and branched topologies. *Nano letters, 9*(10), 3544-3549.

Coe-Sullivan, S., Steckel, J. S., Woo, W. K., Bawendi, M. G., & Bulović, V. (2005). Large-Area Ordered Quantum-Dot Monolayers via Phase Separation During Spin-Casting. *Advanced Functional Materials, 15*(7), 1117-1124. doi:10.1002/adfm.200400468

Colvin, V., Goldstein, A., & Alivisatos, A. (1992). Semiconductor nanocrystals covalently bound to metal surfaces with self-assembled monolayers. *Journal of the American Chemical Society, 114*(13), 5221-5230.

Crooker, S. A., Barrick, T., Hollingsworth, J. A., & Klimov, V. I. (2003). Multiple temperature regimes of radiative decay in CdSe nanocrystal quantum dots: Intrinsic limits to the dark-exciton lifetime. *Appl. Phys. Lett. , 82*(2793). doi:http://dx.doi.org/10.1063/1.1570923

Dabbousi, B. O., Rodriguez-Viejo, J., Mikulec, F. V., Heine, J. R., Mattoussi, H., Ober, R., . . . Bawendi, M. G. (1997). (CdSe)ZnS Core−Shell Quantum Dots:

Synthesis and Characterization of a Size Series of Highly Luminescent Nanocrystallites. *The Journal of Physical Chemistry B, 101*(46), 9463-9475. doi:10.1021/jp971091y

Dahan, M., Levi, S., Luccardini, C., Rostaing, P., Riveau, B., & Triller, A. (2003). Diffusion dynamics of glycine receptors revealed by single-quantum dot tracking. *Science, 302*(5644), 442-445. doi:10.1126/science.1088525

Dai, Q., Sabio, E. M., Wang, W., & Tang, J. (2014). Pulsed laser deposition of Mn doped CdSe quantum dots for improved solar cell performance. *Applied Physics Letters, 104*(18), 183901.

Danek, M., Jensen, K. F., Murray, C. B., & Bawendi, M. G. (1996). Synthesis of luminescent thin-film CdSe/ZnSe quantum dot composites using CdSe quantum dots passivated with an overlayer of ZnSe. *Chemistry of Materials, 8*(1), 173-180.

Das, S., Dutta, A., Banerjee, S., & Sinha, T. P. (2014). Phonon modes and activation energy of Fe-doped CdSe nanoparticles. *Materials Science in Semiconductor Processing, 18*, 152-159. doi:http://dx.doi.org/10.1016/j.mssp.2013.11.023

Deacon, G. B., Faulks, S. J., & Pain, G. N. (1986). The synthesis of organometallics by decarboxylation reactions. *Advances in organometallic chemistry, 25*, 237-276.

Delhez, R., de Keijser, T. H., Langford, J., Louër, D., Mittemeijer, E., & Sonneveld, E. (1993). Crystal imperfection broadening and peak shape in the Rietveld method. *The Rietveld Method*, 132.

Deng, Z., Cao, L., Tang, F., & Zou, B. (2005). A New Route to Zinc-Blende CdSe Nanocrystals: Mechanism and Synthesis. *The Journal of Physical Chemistry B, 109*(35), 16671-16675. doi:10.1021/jp052484x

Devi, L. S., Devi, K. N., Sharma, B. I., & Sarma, H. N. (2014). Influence of Mn doping on structural and optical properties of CdS nanoparticles. *Indian Journal of Physics, 88*(5), 477-482. doi:10.1007/s12648-013-0436-8

Ding, Z., Quinn, B. M., Haram, S. K., Pell, L. E., Korgel, B. A., & Bard, A. J. (2002). Electrochemistry and electrogenerated chemiluminescence from silicon nanocrystal quantum dots. *Science, 296*(5571), 1293-1297. doi:10.1126/science.1069336

Dong, H., Jin, S., Ju, H., Hao, K., Xu, L.-P., Lu, H., & Zhang, X. (2012). Trace and label-free microRNA detection using oligonucleotide encapsulated silver nanoclusters as probes. *Analytical chemistry, 84*(20), 8670-8674.

Dongzhi, Y., Qifan, C., & Shukun, X. (2007). Synthesis of CdSe/CdS with a simple non-TOP-based route. *Journal of Luminescence, 126*(2), 853-858.

Edamatsu, K., Watatani, C., Itoh, T., Shimomura, S., & Hiyamizu, S. (2001). Resonant excitation and anti-Stokes luminescence of GaAs single quantum dots. *Journal of luminescence, 94*, 143-146.

Efros, A. L., & Efros, A. L. (1982). Interband absorption of light in a semiconductor sphere. *Soviet Physics Semiconductors-Ussr, 16*(7), 772-775.

Efros, A. L., Rashba, E. I., & Rosen, M. (2001). Paramagnetic ion-doped nanocrystal as a voltage-controlled spin filter. *Phys. Rev. Lett., 87*, 206601. Retrieved from http://dx.doi.org/10.1103/PhysRevLett.87.206601

Ekimov, A. I., & Efros, A. L. (1988). Optical Spectroscopy of Size Effects in Semiconductor Microcrystals. In J. L. Birman, H. Z. Cummins, & A. A. Kaplyanskii (Eds.), *Laser Optics of Condensed Matter* (pp. 199-207). Boston, MA: Springer US.

Ekimov, A. I., Efros, A. L., & Onushchenko, A. A. (1985). Quantum size effect in semiconductor microcrystals. *Solid State Communications, 56*(11), 921-924. doi:http://dx.doi.org/10.1016/S0038-1098(85)80025-9

Ekimov, A. I., & Onushchenko, A. A. (1981). Quantum size effect in 3-dimensional microscopic semiconductor crystals. *JETP Lett., 34*, 345-349.

Embden, v. J., & Mulvaney, P. (2005). Nucleation and growth of CdSe nanocrystals in a binary ligand system. *Langmuir, 21*(22), 10226-10233.

Erogbogbo, F., Yong, K.-T., Roy, I., Hu, R., Law, W.-C., Zhao, W., . . . Prasad, P. N. (2011). In Vivo Targeted Cancer Imaging, Sentinel Lymph Node Mapping and Multi-Channel Imaging with Biocompatible Silicon Nanocrystals. *ACS Nano, 5*(1), 413-423. doi:10.1021/nn1018945

Erwin, S. C., Zu, L., Haftel, M. I., Efros, A. L., Kennedy, T. A., & Norris, D. J. (2005). Doping semiconductor nanocrystals. *Nature, 436*(7047), 91-94. doi:http://www.nature.com/nature/journal/v436/n7047/suppinfo/nature03832_S1.html

Fan, Z., Li, Y., Li, X., Fan, L., Zhou, S., Fang, D., & Yang, S. (2014). Surrounding media sensitive photoluminescence of boron-doped graphene quantum dots for highly fluorescent dyed crystals, chemical sensing and bioimaging. *Carbon, 70*, 149-156.

Fujioka, K., Hiruoka, M., Sato, K., Manabe, N., Miyasaka, R., Hanada, S., . . . Yamamoto, K. (2008). Luminescent passive-oxidized silicon quantum dots as biological staining labels and their cytotoxicity effects at high concentration. *Nanotechnology, 19*(41), 415102. doi:10.1088/0957-4484/19/41/415102

Gaarenstroom, S., & Winograd, N. (1977). Initial and final state effects in the ESCA spectra of cadmium and silver oxides. *The Journal of Chemical Physics, 67*(8), 3500-3506.

Gaponenko, S. V. (1998). *Optical properties of semiconductor nanocrystals* (Vol. 23): Cambridge university press.

Gerion, D., Pinaud, F., Williams, S. C., Parak, W. J., Zanchet, D., Weiss, S., & Alivisatos, A. P. (2001). Synthesis and properties of biocompatible water-soluble silica-coated CdSe/ZnS semiconductor quantum dots. *The Journal of Physical Chemistry B, 105*(37), 8861-8871.

Giribabu, G., Murali, G., Amaranatha Reddy, D., Liu, C., & Vijayalakshmi, R. P. (2013). Structural, optical and magnetic properties of Co doped CdS nanoparticles. *Journal of Alloys and Compounds, 581*, 363-368. doi:http://dx.doi.org/10.1016/j.jallcom.2013.07.082

Girit, Ç. Ö., Meyer, J. C., Erni, R., Rossell, M. D., Kisielowski, C., Yang, L., . . . Zettl, A. (2009). Graphene at the Edge: Stability and Dynamics. *Science, 323*(5922), 1705. Retrieved from http://science.sciencemag.org/content/323/5922/1705.abstract

Gong, K., & Kelley, D. F. (2015). Lattice strain limit for uniform shell deposition in zincblende CdSe/CdS quantum dots. *The journal of physical chemistry letters, 6*(9), 1559-1562.

Green, M., & O'Brien, P. (1999). The synthesis of cadmium phosphide nanoparticles using cadmium diorganophosphide precursors. *Journal of Materials Chemistry, 9*(1), 243-247. doi:10.1039/A804965C

Gu, Y.-P., Cui, R., Zhang, Z.-L., Xie, Z.-X., & Pang, D.-W. (2011). Ultrasmall near-infrared Ag2Se quantum dots with tunable fluorescence for in vivo imaging. *Journal of the American Chemical Society, 134*(1), 79-82.

Guifu, Z., Hui, L., Yuanguang, Z., Kan, X., & Yitai, Q. (2006). Solvothermal/hydrothermal route to semiconductor nanowires. *Nanotechnology, 17*(11), S313. Retrieved from http://stacks.iop.org/0957-4484/17/i=11/a=S14

Guzelian, A. A., Banin, U., Kadavanich, A. V., Peng, X., & Alivisatos, A. P. (1996). Colloidal chemical synthesis and characterization of InAs nanocrystal quantum dots. *Applied Physics Letters, 69*(10), 1432-1434 (a). doi:doi:http://dx.doi.org/10.1063/1.117605

Guzelian, A. A., Katari, J. E. B., Kadavanich, A. V., Banin, U., Hamad, K., Juban, E., . . . Heath, J. R. (1996). Synthesis of Size-Selected, Surface-Passivated InP Nanocrystals. *The Journal of Physical Chemistry, 100*(17), 7212-7219 (b). doi:10.1021/jp953719f

Hambrock, J., Becker, R., Birkner, A., Wei, & Fischer, R. A. (2002). A non-aqueous organometallic route to highly monodispersed copper nanoparticles using [Cu(OCH(Me)CH2NMe2)2]. *Chemical Communications*(1), 68-69. doi:10.1039/B108797E

Hamizi, N. A., & Johan, M. R. (2010). Synthesis and size dependent optical studies in CdSe quantum dots via inverse micelle technique. *Materials Chemistry and Physics, 124*(1), 395-398. doi:http://dx.doi.org/10.1016/j.matchemphys.2010.06.053

Han, L., Qin, D., Jiang, X., Liu, Y., Wang, L., Chen, J., & Cao, Y. (2006). Synthesis of high quality zinc-blende CdSe nanocrystals and their application in hybrid solar cells. *Nanotechnology, 17*(18), 4736.

Hanif, K. M., Meulenberg, R. W., & Strouse, G. F. (2002). Magnetic ordering in doped Cd1-xCoxSe diluted magnetic quantum dots. *J. Am. Chem. Soc., 124*, 11495-11502. Retrieved from http://dx.doi.org/10.1021/ja0262840

Hao, X., Cho, E.-C., Scardera, G., Shen, Y., Bellet-Amalric, E., Bellet, D., . . . Green, M. (2009). Phosphorus-doped silicon quantum dots for all-silicon quantum dot tandem solar cells. *Solar Energy Materials and Solar Cells, 93*(9), 1524-1530.

Hikmet, R. A. M., Talapin, D. V., & Weller, H. (2003). Study of conduction mechanism and electroluminescence in CdSe/ZnS quantum dot composites. *Journal of Applied Physics, 93*(6), 3509-3514. doi:doi:http://dx.doi.org/10.1063/1.1542940

Hines, M. A., & Guyot-Sionnest, P. (1996). Synthesis and Characterization of Strongly Luminescing ZnS-Capped CdSe Nanocrystals. *The Journal of Physical Chemistry, 100*(2), 468-471. doi:10.1021/jp9530562

Hines, M. A., & Guyot-Sionnest, P. (1998). Bright UV-blue luminescent colloidal ZnSe nanocrystals. *The Journal of Physical Chemistry B, 102*(19), 3655-3657.

Hoener, C. F., Allan, K. A., Bard, A. J., Campion, A., Fox, M. A., Mallouk, T. E., . . . White, J. M. (1992). Demonstration of a shell-core structure in layered cadmium selenide-zinc selenide small particles by x-ray photoelectron and Auger spectroscopies. *The Journal of Physical Chemistry, 96*(9), 3812-3817.

Hoffman, D. M. (2000). Giant internal magnetic fields in Mn doped nanocrystal quantum dots. *Solid State Commun., 114*, 547-550. Retrieved from http://dx.doi.org/10.1016/S0038-1098(00)00089-2

Hong, G., Robinson, J. T., Zhang, Y., Diao, S., Antaris, A. L., Wang, Q., & Dai, H. (2012). In Vivo Fluorescence Imaging with Ag2S Quantum Dots in the Second Near-Infrared Region. *Angewandte Chemie, 124*(39), 9956-9959.

Hou, J., Zhao, H., Huang, F., Jing, Q., Cao, H., Wu, Q., . . . Cao, G. (2016). High performance of Mn-doped CdSe quantum dot sensitized solar cells based on the vertical ZnO nanorod arrays. *Journal of Power Sources, 325*, 438-445. doi:http://dx.doi.org/10.1016/j.jpowsour.2016.06.070

Huang, J., Jiang, Y., Duan, H., Liu, C., Mi, L., Lan, X., . . . Zhong, H. (2013). Large Stokes Shift of Ag Doped CdSe Quantum Dots via Aqueous Route. *Journal of nanoscience and nanotechnology, 13*(10), 6687-6693.

Huang, Z., Pu, F., Lin, Y., Ren, J., & Qu, X. (2011). Modulating DNA-templated silver nanoclusters for fluorescence turn-on detection of thiol compounds. *Chemical Communications, 47*(12), 3487-3489.

Huynh, W. U., Dittmer, J. J., & Alivisatos, A. P. (2002). Hybrid nanorod-polymer solar cells. *science, 295*(5564), 2425-2427.

Hwang, I. S., Kim, H. D., Kim, J. E., Park, H. Y., & Lim, H. (1994). Solid solubilities of magnetic ions in diluted magnetic semiconductors grown under equilibrium conditions. *Phys. Rev. B, 50*, 8849-8852. Retrieved from http://dx.doi.org/10.1103/PhysRevB.50.8849

Ignatiev, I. V., Kozin, I. E., Ren, H.-W., Sugou, S., & Masumoto, Y. (1999). Anti-Stokes photoluminescence of InP self-assembled quantum dots in the presence of electric current. *Physical review B, 60*(20), R14001.

Inamdar, S. N., Ingole, P. P., & Haram, S. K. (2008). Determination of Band Structure Parameters and the Quasi-Particle Gap of CdSe Quantum Dots by Cyclic Voltammetry. *ChemPhysChem, 9*(17), 2574-2579.

Ivanov-Ehmin, B., Nevskaya, N., Zajtsev, B., & Ivanova, T. (1982). Synthesis and properties of calcium and strontium hydroxomanganates (3). *Zhurnal Neorganicheskoj Khimii, 27*(12), 3101-3104.

Ivanov, S. A., Piryatinski, A., Nanda, J., Tretiak, S., Zavadil, K. R., Wallace, W. O., . . . Klimov, V. I. (2007). Type-II Core/Shell CdS/ZnSe Nanocrystals: Synthesis, Electronic Structures, and Spectroscopic Properties. *Journal of the American Chemical Society, 129*(38), 11708-11719. doi:10.1021/ja068351m

Jamil, N. Y., & Shaw, D. (1995). The diffusion of Mn in CdTe. *Semicond. Sci. Technol., 10*, 952-958. Retrieved from http://dx.doi.org/10.1088/0268-1242/10/7/009

Jang, E., Jun, S., & Pu, L. (2003). High quality CdSeS nanocrystals synthesized by facile single injection process and their electroluminescence. *Chemical Communications*(24), 2964-2965. doi:10.1039/B310853H

Ji, T. H., Jian, W. B., & Fang, J. Y. (2003). The first synthesis of Pb1-xMnxSe nanocrystals. *J. Am. Chem. Soc., 125*, 8448-8449. Retrieved from http://dx.doi.org/10.1021/ja0351746

Jian, Z., & Hejing, W. (2003). The physical meanings of 5 basic parameters for an X-ray diffraction peak and their application. *Chinese Journal of Geochemistry, 22*(1), 38-44.

Jiang, F., & Muscat, A. J. (2012). Ligand-controlled growth of ZnSe quantum dots in water during Ostwald ripening. *Langmuir, 28*(36), 12931-12940.

Kammerer, C., Cassabois, G., Voisin, C., Delalande, C., Roussignol, P., & Gérard, J. (2001). Photoluminescence up-conversion in single self-assembled InAs/GaAs quantum dots. *Physical review letters, 87*(20), 207401.

Karen, P., & Woodward, P. M. (1998). Liquid-mix disorder in crystalline solids: ScMnO 3. *Journal of Solid State Chemistry, 141*(1), 78-88.

Kasuya, A. (2004). Ultra-stable nanoparticles of CdSe revealed from mass spectrometry. *Nature Mater., 3*, 99-102. Retrieved from http://dx.doi.org/10.1038/nmat1056

Katari, J. B., Colvin, V. L., & Alivisatos, A. P. (1994). X-ray photoelectron spectroscopy of CdSe nanocrystals with applications to studies of the nanocrystal surface. *The Journal of Physical Chemistry, 98*(15), 4109-4117.

Katari, J. E. B., Colvin, V. L., & Alivisatos, A. P. (1994). X-ray Photoelectron Spectroscopy of CdSe Nanocrystals with Applications to Studies of the Nanocrystal Surface. *The Journal of Physical Chemistry, 98*(15), 4109-4117. doi:10.1021/j100066a034

Kaxiras, E. (1990). Effect of surface reconstruction on stability and reactivity of Si clusters. *Phys. Rev. Lett., 64*, 551-554. Retrieved from http://dx.doi.org/10.1103/PhysRevLett.64.551

Kelley, A. M., Dai, Q., Jiang, Z.-j., Baker, J. A., & Kelley, D. F. (2013). Resonance Raman spectra of wurtzite and zincblende CdSe nanocrystals. *Chemical Physics, 422*, 272-276.

Kher, S. S., & Wells, R. L. (1994). A Straightforward, New Method for the Synthesis of Nanocrystalline GaAs and GaP. *Chemistry of Materials, 6*(11), 2056-2062. doi:10.1021/cm00047a027

Klein, M., Hache, F., Ricard, D., & Flytzanis, C. (1990). Size dependence of electron-phonon coupling in semiconductor nanospheres: the case of CdSe. *Physical Review B, 42*(17), 11123.

Klimov, V. I. (2006). Mechanisms for photogeneration and recombination of multiexcitons in semiconductor nanocrystals: implications for lasing and solar energy conversion. *The Journal of Physical Chemistry B, 110*(34), 16827-16845.

Klimov, V. I., Mikhailovsky, A. A., Xu, S., Malko, A., Hollingsworth, J. A., Leatherdale, C. A., . . . Bawendi, M. G. (2000). Optical gain and stimulated emission in nanocrystal quantum dots. *Science, 290*(5490), 314-317.

Knox, R. S. (1963). *Theory of excitons* (Vol. 5): Academic Press.

Koh, A. K., & Miller, D. J. (1986). The systematic variation of the EPR parameters of manganese in II-VI semiconductors. *Solid State Commun., 60*, 217-222. Retrieved from http://dx.doi.org/10.1016/0038-1098(86)90449-7

Kortan, A., Hull, R., Opila, R. L., Bawendi, M. G., Steigerwald, M. L., Carroll, P., & Brus, L. E. (1990). Nucleation and growth of cadmium selendie on zinc sulfide quantum crystallite seeds, and vice versa, in inverse micelle media. *Journal of the American Chemical Society, 112*(4), 1327-1332.

Kotkata, M., Masoud, A., Mohamed, M., & Mahmoud, E. (2009). Structural characterization of chemically synthesized CdSe nanoparticles. *Physica E: Low-dimensional Systems and Nanostructures, 41*(4), 640-645.

Kresse, G., & Furthmuller, J. (1996). Efficient iterative schemes for ab initio total-energy calculations using a plane-wave basis set. *Phys. Rev. B, 54*, 11169-11186. Retrieved from http://dx.doi.org/10.1103/PhysRevB.54.11169

Kümmell, T., Bacher, G., Forchel, A., Lermann, G., Kiefer, W., Jobst, B., . . . Landwehr, G. (1998). Size dependence of strain relaxation and lateral quantization in deep etched Cd x Zn 1− x S e/Z n S e quantum wires. *Physical Review B, 57*(24), 15439.

Kwak, W.-C., Kim, T. G., Chae, W.-S., & Sung, Y.-M. (2007). Tuning the energy bandgap of CdSe nanocrystals via Mg doping. *Nanotechnology, 18*(20), 205702.

Kwak, W.-C., Sung, Y.-M., Kim, T. G., & Chae, W.-S. (2007). Synthesis of Mn-doped zinc blende CdSe nanocrystals. *Applied Physics Letters, 90*(17), 173111. doi:doi:http://dx.doi.org/10.1063/1.2731682

Lan, G.-Y., Huang, C.-C., & Chang, H.-T. (2010). Silver nanoclusters as fluorescent probes for selective and sensitive detection of copper ions. *Chemical communications, 46*(8), 1257-1259.

Langford, J. (1980). Accuracy of crystallite size and strain determined from the integral breadth of powder diffraction lines *NBS Spec. Publ. 567* (pp. 255-269): National Bureau of Standards Washington, DC.

Langford, J. I., & Wilson, A. (1978). Scherrer after sixty years: a survey and some new results in the determination of crystallite size. *Journal of Applied Crystallography, 11*(2), 102-113.

Leatherdale, C. A., Kagan, C. R., Morgan, N. Y., Empedocles, S. A., Kastner, M. A., & Bawendi, M. G. (2000). Photoconductivity in CdSe quantum dot solids. *Physical Review B, 62*(2669).

Lee, H., Holloway, P. H., & Yang, H. (2006). Synthesis and characterization of colloidal ternary ZnCdSe semiconductor nanorods. *The Journal of chemical physics, 125*(16), 164711.

Lee, Y.-b., Ho Lee, S., Lee, S., Lee, H., Kim, J., & Joo, J. (2013). Surface enhanced Raman scattering effect of CdSe/ZnS quantum dots hybridized with Au nanowire. *Applied Physics Letters, 102*(3), 033109. doi:doi:http://dx.doi.org/10.1063/1.4788926

Lehmann, V., & Gösele, U. (1991). Porous silicon formation: A quantum wire effect. *Applied Physics Letters, 58*(8), 856-858. doi:doi:http://dx.doi.org/10.1063/1.104512

Leonard, D., Krishnamurthy, M., Reaves, C. M., Denbaars, S. P., & Petroff, P. M. (1993). Direct formation of quantum-sized dots from uniform coherent islands of InGaAs on GaAs surfaces. *Applied Physics Letters, 63*(23), 3203-3205. doi:doi:http://dx.doi.org/10.1063/1.110199

Levy, L., Hochepied, J., & Pileni, M. (1996). Control of the size and composition of three dimensionally diluted magnetic semiconductor clusters. *The Journal Of Physical Chemistry, 100*(47), 18322-18326.

Li, H., Kang, Z., Liu, Y., & Lee, S.-T. (2012). Carbon nanodots: synthesis, properties and applications. *Journal of Materials Chemistry, 22*(46), 24230-24253. doi:10.1039/C2JM34690G

Li, J., Zhong, X., Zhang, H., Le, X. C., & Zhu, J.-J. (2012). Binding-induced fluorescence turn-on assay using aptamer-functionalized silver nanocluster DNA probes. *Analytical chemistry, 84*(12), 5170-5174.

Li, L., Daou, T. J., Texier, I., Kim Chi, T. T., Liem, N. Q., & Reiss, P. (2009). Highly luminescent CuInS2/ZnS core/shell nanocrystals: cadmium-free quantum dots for in vivo imaging. *Chemistry of Materials, 21*(12), 2422-2429.

Li, L., Wu, G., Yang, G., Peng, J., Zhao, J., & Zhu, J.-J. (2013). Focusing on luminescent graphene quantum dots: current status and future perspectives. *Nanoscale, 5*(10), 4015-4039. doi:10.1039/C3NR33849E

Li, Y., Qian, F., Xiang, J., & Lieber, C. M. (2006). Nanowire electronic and optoelectronic devices. *Materials today, 9*(10), 18-27.

Liang, W. (1970). Excitons. *Physics Education, 5*(4), 226.

Lim, S. F., Riehn, R., Ryu, W. S., Khanarian, N., Tung, C. K., Tank, D., & Austin, R. H. (2006). In vivo and scanning electron microscopy imaging of up-converting nanophosphors in Caenorhabditis elegans. *Nano Lett, 6*(2), 169-174. doi:10.1021/nl0519175

Linhui, Y., Hong, R., Yi, Z., & Danzhen, L. (2013). A facile solvothermal method to produce ZnS quantum dots-decorated graphene nanosheets with superior photoactivity. *Nanotechnology, 24*(37), 375601. Retrieved from http://stacks.iop.org/0957-4484/24/i=37/a=375601

Liu, R., Wu, D., Feng, X., & Müllen, K. (2011). Bottom-up fabrication of photoluminescent graphene quantum dots with uniform morphology. *Journal of the American Chemical Society, 133*(39), 15221-15223.

Lobo, C., & Leon, R. (1998). InGaAs island shapes and adatom migration behavior on (100), (110), (111), and (311) GaAs surfaces. *Journal of Applied Physics, 83*(8), 4168-4172. doi:doi:http://dx.doi.org/10.1063/1.367170

Maki, H., Sato, T., & Ishibashi, K. (2007). Direct observation of the deformation and the band gap change from an individual single-walled carbon nanotube under uniaxial strain. *Nano letters, 7*(4), 890-895.

Manna, L., Scher, E. C., & Alivisatos, A. P. (2000). Synthesis of Soluble and Processable Rod-, Arrow-, Teardrop-, and Tetrapod-Shaped CdSe Nanocrystals. *Journal of the American Chemical Society, 122*(51), 12700-12706. doi:10.1021/ja003055+

Mehta, S., Kumar, S., Chaudhary, S., Bhasin, K., & Gradzielski, M. (2008). Evolution of ZnS nanoparticles via facile CTAB aqueous micellar solution route: a study on controlling parameters. *Nanoscale research letters, 4*(1), 17.

Mekis, I., Talapin, D. V., Kornowski, A., Haase, M., & Weller, H. (2003). One-Pot Synthesis of Highly Luminescent CdSe/CdS Core−Shell Nanocrystals via Organometallic and "Greener" Chemical Approaches. *The Journal of Physical Chemistry B, 107*(30), 7454-7462. doi:10.1021/jp0278364

Meulenberg, R. W., Jennings, T., & Strouse, G. F. (2004). Compressive and tensile stress in colloidal CdSe semiconductor quantum dots. *Physical Review B, 70*(23), 235311.

Meulenberg, R. W., van Buuren, T., Hanif, K. M., Willey, T. M., Strouse, G. F., & Terminello, L. J. (2004). Structure and Composition of Cu-Doped CdSe Nanocrystals Using Soft X-ray Absorption Spectroscopy. *Nano Letters, 4*(11), 2277-2285. doi:10.1021/nl048738s

Micic, O. I., Sprague, J. R., Curtis, C. J., Jones, K. M., Machol, J. L., Nozik, A. J., . . . Peyghambarian, N. (1995). Synthesis and Characterization of InP, GaP, and GaInP2 Quantum Dots. *The Journal of Physical Chemistry, 99*(19), 7754-7759. doi:10.1021/j100019a063

Mikulec, F. V. (2000). Organometallic synthesis and spectroscopic characterization of manganese-doped CdSe nanocrystals. *J. Am. Chem. Soc., 122*, 2532-2540. Retrieved from http://dx.doi.org/10.1021/ja991249n

Ming, H., Ma, Z., Liu, Y., Pan, K., Yu, H., Wang, F., & Kang, Z. (2012). Large scale electrochemical synthesis of high quality carbon nanodots and their photocatalytic property. *Dalton Trans, 41*(31), 9526-9531. doi:10.1039/c2dt30985h

Mooradian, A. (1969). Photoluminescence of metals. *Physical Review Letters, 22*(5), 185.

Muck, T., Wagner, J. W., Hansen, L., Wagner, V., & Geurts, J. (2004). Raman identification of the in-plane axes of zincblende (100) surfaces: Basic principles and application to II–VI/III–V heterostructures. *Journal of Applied Physics, 95*(10), 5403-5407. doi:doi:http://dx.doi.org/10.1063/1.1707209

Murray, C. B., Kagan, C., & Bawendi, M. (2000). Synthesis and characterization of monodisperse nanocrystals and close-packed nanocrystal assemblies. *Annual Review of Materials Science, 30*(1), 545-610.

Murray, C. B., Norris, D. J., & Bawendi, M. G. (1993). Synthesis and characterization of nearly monodisperse CdE (E = sulfur, selenium, tellurium) semiconductor nanocrystallites. *Journal of the American Chemical Society, 115*(19), 8706-8715. doi:10.1021/ja00072a025

Murray, C. B., Sun, S., Gaschler, W., Doyle, H., Betley, T. A., & Kagan, C. R. (2001). Colloidal synthesis of nanocrystals and nanocrystal superlattices. *IBM Journal of Research and Development, 45*(1), 47-56. doi:10.1147/rd.451.0047

Nehru, L. C., & Sanjeeviraja, C. (2014). Rapid synthesis of nanocrystalline SnO2 by a microwave-assisted combustion method. *Journal of Advanced Ceramics, 3*(3), 171-176. doi:10.1007/s40145-014-0101-5

Norris, D. J., & Bawendi, M. G. (1996). Measurement and assignment of the size-dependent optical spectrum in CdSe quantum dots. *Physical Review B, 53*(24), 16338-16346. Retrieved from http://link.aps.org/doi/10.1103/PhysRevB.53.16338

Norris, D. J., Efros, A. L., & Erwin, S. C. (2008). Doped nanocrystals. *Science, 319*(5871), 1776-1779.

Norris, D. J., Yao, N., Charnock, F. T., & Kennedy, T. A. (2001). High-Quality Manganese-Doped ZnSe Nanocrystals. *Nano Letters, 1*(1), 3-7. doi:10.1021/nl005503h

Ogawa, S., Hu, K., Fan, F.-R. F., & Bard, A. J. (1997). Photoelectrochemistry of films of quantum size lead sulfide particles incorporated in self-assembled monolayers on gold. *The Journal of Physical Chemistry B, 101*(29), 5707-5711.

Olshavsky, M. A., Goldstein, A. N., & Alivisatos, A. P. (1990). Organometallic synthesis of gallium-arsenide crystallites, exhibiting quantum confinement. *Journal of the American Chemical Society, 112*(25), 9438-9439. doi:10.1021/ja00181a080

Oluwafemi, O. S., Revaprasadu, N., & Adeyemi, O. O. (2010). A new synthesis of hexadecylamine-capped Mn-doped wurtzite CdSe nanoparticles. *Materials Letters, 64*(13), 1513-1516.

Orlinskii, S. B., Schmidt, J., Baranov, P. G., Hofmann, D. M., de Mello Donegá, C., & Meijerink, A. (2004). Probing the wave function of shallow Li and Na donors in ZnO nanoparticles. *Physical review letters, 92*(4), 047603.

Pan, D., Zhang, J., Li, Z., & Wu, M. (2010). Hydrothermal route for cutting graphene sheets into blue-luminescent graphene quantum dots. *Adv Mater, 22*(6), 734-738. doi:10.1002/adma.200902825

Paskov, P., Holtz, P.-O., Monemar, B., Garcia, J., Schoenfeld, W., & Petroff, P. M. (2000). Photoluminescence up-conversion in InAs/GaAs self-assembled quantum dots. *Applied Physics Letters, 77*(6), 812-814.

Patel, N. H., Deshpande, M., Bhatt, S. V., Patel, K. R., & Chaki, S. (2014). Structural and magnetic properties of undoped and Mn doped CdS nanoparticles prepared by chemical co-precipitation method. *Advanced Materials Letters, 5*, 671-677.

Pejova, B., & Abay, B. (2011). Nanostructured CdSe films in low size-quantization regime: Temperature dependence of the band gap energy and sub-band gap absorption tails. *The Journal of Physical Chemistry C, 115*(47), 23241-23255.

Peng, X. (2002). Green Chemical Approaches toward High-Quality Semiconductor Nanocrystals. *Chemistry–A European Journal, 8*(2), 334-339.

Peng, X. (2010). Band gap and composition engineering on a nanocrystal (BCEN) in solution. *Accounts of chemical research, 43*(11), 1387-1395.

Peng, X., Manna, L., Yang, W., Wickham, J., Scher, E., Kadavanich, A., & Alivisatos, A. P. (2000). Shape control of CdSe nanocrystals. *Nature, 404*(6773), 59-61. Retrieved from http://dx.doi.org/10.1038/35003535

Peng, X., Schlamp, M. C., Kadavanich, A. V., & Alivisatos, A. P. (1997). Epitaxial Growth of Highly Luminescent CdSe/CdS Core/Shell Nanocrystals with Photostability and Electronic Accessibility. *Journal of the American Chemical Society, 119*(30), 7019-7029. doi:10.1021/ja970754m

Peng, X., Wickham, J., & Alivisatos, A. P. (1998). Kinetics of II-VI and III-V Colloidal Semiconductor Nanocrystal Growth: "Focusing" of Size Distributions. *Journal of the American Chemical Society, 120*(21), 5343-5344. doi:10.1021/ja9805425

Peng, X. G. (2000). Shape control of CdSe nanocrystals. *Nature*, *404*, 59-61. Retrieved from http://dx.doi.org/10.1038/35003535

Peng, Z. A., & Peng, X. (2001). Formation of High-Quality CdTe, CdSe, and CdS Nanocrystals Using CdO as Precursor. *Journal of the American Chemical Society, 123*(1), 183-184. doi:10.1021/ja003633m

Perdew, J. P., Burke, K., & Ernzerhof, M. (1996). Generalized gradient approximation made simple. *Phys. Rev. Lett., 77*, 3865-3868. Retrieved from http://dx.doi.org/10.1103/PhysRevLett.77.3865

Persson, J., Håkanson, U., Johansson, M.-J., Samuelson, L., & Pistol, M.-E. (2005). Strain effects on individual quantum dots: Dependence of cap layer thickness. *Physical Review B, 72*(8), 085302.

Phadnis, C., Sonawane, K. G., Hazarika, A., & Mahamuni, S. (2015). Strain-Induced Hierarchy of Energy Levels in CdS/ZnS Nanocrystals. *The Journal of Physical Chemistry C, 119*(42), 24165-24173.

Plotnichenko, V., & Mityagin, Y. (1977). Investigation of Fundamental Vibrations in CdSe by Raman Scattering and Infrared Methods. *Sov. Phys. Solid State, 19*(9), 1584-1586.

Pokrant, S., & Whaley, K. B. (1999). Tight-binding studies of surface effects on electronic structure of CdSe nanocrystals: the role of organic ligands, surface reconstruction, and inorganic capping shells. *Eur. Phys. J. D, 6*(2), 255-267. Retrieved from http://dx.doi.org/10.1007/s100530050307

Poles, E., Selmarten, D. C., Mićić, O. I., & Nozik, A. J. (1999). Anti-Stokes photoluminescence in colloidal semiconductor quantum dots. *Applied physics letters, 75*(7), 971-973.

Ponomarenko, L. A., Schedin, F., Katsnelson, M. I., Yang, R., Hill, E. W., Novoselov, K. S., & Geim, A. K. (2008). Chaotic Dirac Billiard in Graphene Quantum Dots. *Science, 320*(5874), 356. Retrieved from http://science.sciencemag.org/content/320/5874/356.abstract

Qian, H., Li, L., & Ren, J. (2005). One-step and rapid synthesis of high quality alloyed quantum dots (CdSe–CdS) in aqueous phase by microwave irradiation with controllable temperature. *Materials Research Bulletin, 40*(10), 1726-1736. doi:http://dx.doi.org/10.1016/j.materresbull.2005.05.022

Qu, L., & Peng, X. (2002). Control of photoluminescence properties of CdSe nanocrystals in growth. *Journal of the American Chemical Society, 124*(9), 2049-2055.

Qu, L., Peng, Z. A., & Peng, X. (2001). Alternative Routes toward High Quality CdSe Nanocrystals. *Nano Letters, 1*(6), 333-337. doi:10.1021/nl0155532

Radovanovic, P. V., & Gamelin, D. R. (2001). Electronic absorption spectroscopy of cobalt ions in diluted magnetic semiconductor quantum dots: demonstration of an isocrystalline core/shell synthetic method. *Journal of the American Chemical Society, 123*(49), 12207-12214.

Rajabi, H. R., Khani, O., Shamsipur, M., & Vatanpour, V. (2013). High-performance pure and Fe 3+-ion doped ZnS quantum dots as green nanophotocatalysts for the

removal of malachite green under UV-light irradiation. *Journal of hazardous materials, 250*, 370-378.

Reed, M. A. (1993). Quantum dots. *Scientific American, 268*(1), 118-123.

Reed, M. A., Randall, J. N., Aggarwal, R. J., Matyi, R. J., Moore, T. M., & Wetsel, A. E. (1988). Observation of discrete electronic states in a zero-dimensional semiconductor nanostructure. *Physical Review Letters, 60*(6), 535-537. Retrieved from http://link.aps.org/doi/10.1103/PhysRevLett.60.535

Reiss, P., Bleuse, J., & Pron, A. (2002). Highly Luminescent CdSe/ZnSe Core/Shell Nanocrystals of Low Size Dispersion. *Nano Letters, 2*(7), 781-784. doi:10.1021/nl025596y

Reiss, P., Quemard, G., Carayon, S., Bleuse, J., Chandezon, F., & Pron, A. (2004). Luminescent ZnSe nanocrystals of high color purity. *Materials Chemistry and Physics, 84*(1), 10-13.

Ren, S.-F., Xia, J.-B., Han, H.-X., & Wang, Z.-P. (1994). Electronic structure and optical properties of [(ZnSe) m (CdSe) n] N-ZnSe multiple quantum wells. *Physical Review B, 50*(19), 14416.

Rogach, A. L., Katsikas, L., Kornowski, A., Su, D., Eychmüller, A., & Weller, H. (1996). Synthesis and characterization of thiol-stabilized CdTe nanocrystals. *Berichte der Bunsengesellschaft für physikalische Chemie, 100*(11), 1772-1778. doi:10.1002/bbpc.19961001104

Sapsford, K. E., Berti, L., & Medintz, I. L. (2006). Materials for fluorescence resonance energy transfer analysis: beyond traditional donor-acceptor combinations. *Angew Chem Int Ed Engl, 45*(28), 4562-4589. doi:10.1002/anie.200503873

Sashchiuk, A., Lifshitz, E., Reisfeld, R., Saraidarov, T., Zelner, M., & Willenz, A. (2002). Optical and conductivity properties of PbS nanocrystals in amorphous zirconia sol-gel films. *Journal of sol-gel science and technology, 24*(1), 31-38.

Scherer, A., Craighead, H. G., & Beebe, E. D. (1987). Gallium arsenide and aluminum gallium arsenide reactive ion etching in boron trichloride/argon mixtures. *Journal of Vacuum Science & Technology B, 5*(6), 1599-1605. doi:doi:http://dx.doi.org/10.1116/1.583635

Scherrer, P. (1918). The Scherrer Formula for X-Ray Particle Size Determination. *Göttinger Nachrichten, 2*, 98-100.

Schumacher, W., Nagy, A., Waldman, W. J., & Dutta, P. K. (2009). Direct Synthesis of Aqueous CdSe/ZnS-Based Quantum Dots Using Microwave Irradiation. *The Journal of Physical Chemistry C, 113*(28), 12132-12139. doi:10.1021/jp901003r

Sethi, R., Kumar, L., Sharma, P. K., & Pandey, A. (2009). Tunable visible emission of Ag-doped CdZnS alloy quantum dots. *Nanoscale research letters, 5*(1), 96.

Sharma, J., Yeh, H.-C., Yoo, H., Werner, J. H., & Martinez, J. S. (2011). Silver nanocluster aptamers: in situ generation of intrinsically fluorescent recognition ligands for protein detection. *Chemical Communications, 47*(8), 2294-2296.

Sharma, S. N., Pillai, Z. S., & Kamat, P. V. (2003). Photoinduced charge transfer between CdSe quantum dots and p-phenylenediamine. *The Journal of Physical Chemistry B, 107*(37), 10088-10093.

Shen, J., Zhu, Y., Yang, X., & Li, C. (2012). Graphene quantum dots: emergent nanolights for bioimaging, sensors, catalysis and photovoltaic devices. *Chemical Communications, 48*(31), 3686-3699. doi:10.1039/C2CC00110A

Shen, J., Zhu, Y., Yang, X., Zong, J., Zhang, J., & Li, C. (2012). One-pot hydrothermal synthesis of graphene quantum dots surface-passivated by polyethylene glycol and their photoelectric conversion under near-infrared light. *New Journal of Chemistry, 36*(1), 97-101. doi:10.1039/C1NJ20658C

Shen, T., Tian, J., Lv, L., Fei, C., Wang, Y., Pullerits, T., & Cao, G. (2016). Investigation of the role of Mn dopant in CdS quantum dot sensitized solar cell. *Electrochimica Acta, 191*, 62-69. doi:http://dx.doi.org/10.1016/j.electacta.2016.01.056

Shiang, J. J., Kadavanich, A. V., Grubbs, R. K., & Alivisatos, A. P. (1995). Symmetry of annealed wurtzite CdSe nanocrystals [mdash] assignment to the C3v point group. *J. Phys. Chem., 99*, 17417-17422. Retrieved from http://dx.doi.org/10.1021/j100048a017

Shim, M., & Guyot-Sionnest, P. (2000). n-type colloidal semiconductor nanocrystals. *Nature, 407*, 981-983. Retrieved from http://dx.doi.org/10.1038/35039577

Shinae, J., Eunjoo, J., & Youngsu, C. (2006). Alkyl thiols as a sulfur precursor for the preparation of monodisperse metal sulfide nanostructures. *Nanotechnology, 17*(19), 4806. Retrieved from http://stacks.iop.org/0957-4484/17/i=19/a=004

Smith, A. M., Mohs, A. M., & Nie, S. (2009). Tuning the optical and electronic properties of colloidal nanocrystals by lattice strain. *Nature nanotechnology, 4*(1), 56-63.

Smith, A. M., & Nie, S. (2009). Semiconductor nanocrystals: structure, properties, and band gap engineering. *Accounts of chemical research, 43*(2), 190-200.

Smith, A. M., & Nie, S. (2010). Semiconductor Nanocrystals: Structure, Properties, and Band Gap Engineering. *Accounts of Chemical Research, 43*(2), 190-200. doi:10.1021/ar9001069

Spanhel, L., & Anderson, M. A. (1991). Semiconductor clusters in the sol-gel process: quantized aggregation, gelation, and crystal growth in concentrated zinc oxide colloids. *Journal of the American Chemical Society, 113*(8), 2826-2833.

Spanhel, L., Haase, M., Weller, H., & Henglein, A. (1987). Photochemistry of colloidal semiconductors. 20. Surface modification and stability of strong luminescing CdS particles. *Journal of the American Chemical Society, 109*(19), 5649-5655.

Steiner, D., Dorfs, D., Banin, U., Della Sala, F., Manna, L., & Millo, O. (2008). Determination of band offsets in heterostructured colloidal nanorods using scanning tunneling spectroscopy. *Nano letters, 8*(9), 2954-2958.

Stouwdam, J. W., & Janssen, R. A. (2009). Electroluminescent Cu-doped CdS Quantum Dots. *Advanced Materials, 21*(28), 2916-2920.

Stowell, C. A., Wiacek, R. J., Saunders, A. E., & Korgel, B. A. (2003). Synthesis and characterization of dilute magnetic semiconductor manganese-doped indium arsenide nanocrystals. *Nano Letters, 3*(10), 1441-1447.

Su, Y.-T., Lan, G.-Y., Chen, W.-Y., & Chang, H.-T. (2010). Detection of copper ions through recovery of the fluorescence of DNA-templated copper/silver nanoclusters in the presence of mercaptopropionic acid. *Analytical chemistry, 82*(20), 8566-8572.

Sung, Y.-M., Kwak, W.-C., & Kim, T. G. (2008). Coarsening Kinetics of Mn-Doped CdSe Nanocrystals. *Crystal Growth & Design, 8*(4), 1186-1190. doi:10.1021/cg0705005

Sung, Y. M., Lee, Y. J., & Park, K. S. (2006). Kinetic analysis for formation of Cd1-xZnxSe solid-solution nanocrystals. *J. Am. Chem. Soc., 128*(28), 9002-9003.

Suri, P., & Mehra, R. M. (2007). Effect of electrolytes on the photovoltaic performance of a hybrid dye sensitized ZnO solar cell. *Solar Energy Materials and Solar Cells, 91*(6), 518-524. doi:http://dx.doi.org/10.1016/j.solmat.2006.10.025

Suyver, J. F., Wuister, S. F., Kelly, J. J., & Meijerink, A. (2000). Luminescence of nanocrystalline ZnSe:Mn2+. *Phys. Chem. Chem. Phys., 2*, 5445-5448. Retrieved from http://dx.doi.org/10.1039/b006950g

Swihart, M. T. (2003). Vapor-phase synthesis of nanoparticles. *Current Opinion in Colloid & Interface Science, 8*(1), 127-133. doi:http://dx.doi.org/10.1016/S1359-0294(03)00007-4

Takagahara, T., & Takeda, K. (1992). Theory of the quantum confinement effect on excitons in quantum dots of indirect-gap materials. *Physical Review B, 46*(23), 15578.

Talapin, D. V., Mekis, I., Götzinger, S., Kornowski, A., Benson, O., & Weller, H. (2004). CdSe/CdS/ZnS and CdSe/ZnSe/ZnS core-shell-shell nanocrystals. *The Journal of Physical Chemistry B, 108*(49), 18826-18831.

Talapin, D. V., Rogach, A. L., Kornowski, A., Haase, M., & Weller, H. (2001). Highly Luminescent Monodisperse CdSe and CdSe/ZnS Nanocrystals Synthesized in a Hexadecylamine−Trioctylphosphine Oxide−Trioctylphospine Mixture. *Nano Letters, 1*(4), 207-211. doi:10.1021/nl0155126

Tamang, S., Beaune, G., Texier, I., & Reiss, P. (2011). Aqueous phase transfer of InP/ZnS nanocrystals conserving fluorescence and high colloidal stability. *ACS nano, 5*(12), 9392-9402.

Tang, L., Ji, R., Cao, X., Lin, J., Jiang, H., Li, X., . . . Lau, S. P. (2012). Deep ultraviolet photoluminescence of water-soluble self-passivated graphene quantum dots. *ACS Nano, 6*(6), 5102-5110. doi:10.1021/nn300760g

Thanh, N. T., Maclean, N., & Mahiddine, S. (2014). Mechanisms of nucleation and growth of nanoparticles in solution. *Chemical Reviews, 114*(15), 7610-7630.

Thanikaikarasan, S., Shajan, X. S., Dhanasekaran, V., & Mahalingam, T. (2011). X-ray line broadening and photoelectrochemical studies on CdSe thin films. *Journal of materials science, 46*(11), 4034-4045.

Trallero-Giner, C., Debernardi, A., Cardona, M., Menendez-Proupin, E., & Ekimov, A. (1998). Optical vibrons in CdSe dots and dispersion relation of the bulk material. *Physical Review B, 57*(8), 4664.

Trindade, T., Neves, M., & Barros, A. (2000). Preparation and optical properties of CdSe/polymer nanocomposites. *Scripta materialia, 43*(6), 567-571.

Tsutsui, K., Hu, E. L., & Wilkinson, C. D. (1993). Reactive ion etched II-VI quantum dots: dependence of etched profile on pattern geometry. *Japanese journal of applied physics, 32*(12S), 6233.

Wang, C., Jiang, Y., Chen, L., Li, S., Li, G., & Zhang, Z. (2009). Temperature dependence of optical properties and size tunability CdSe quantum dots via non-TOP synthesis. *Materials Chemistry and Physics, 116*(2), 388-391.

Wang, J., Zhang, G., Li, Q., Jiang, H., Liu, C., Amatore, C., & Wang, X. (2013). In vivo self-bio-imaging of tumors through in situ biosynthesized fluorescent gold nanoclusters. *Scientific reports, 3*, 1157.

Wang, X., Cao, L., Lu, F., Meziani, M. J., Li, H., Qi, G., . . . Sun, Y.-P. (2009). Photoinduced electron transfers with carbon dots. *Chemical Communications*(25), 3774-3776. doi:10.1039/B906252A

Wang, Y., & Herron, N. (1991). Nanometer-sized semiconductor clusters: materials synthesis, quantum size effects, and photophysical properties. *The Journal of Physical Chemistry, 95*(2), 525-532.

Wang, Y., Herron, N., Moller, K., & Bein, T. (1991). 3-dimensionally confined diluted magnetic semiconductor clusters: Zn1-xMnxS. *Solid State Commun., 77*, 33-38. Retrieved from http://dx.doi.org/10.1016/0038-1098(91)90421-Q

Warren, B., & Averbach, B. (1950). The effect of cold-work distortion on X-ray patterns. *Journal of Applied Physics, 21*(6), 595-599.

Wei, S.-H., & Zunger, A. (1999). Predicted band-gap pressure coefficients of all diamond and zinc-blende semiconductors: Chemical trends. *Physical Review B, 60*(8), 5404.

Williamson, G., & Hall, W. (1953). X-ray line broadening from filed aluminium and wolfram. *Acta metallurgica, 1*(1), 22-31.

Wortis, M. (1988). Chemistry and Physics of Solid Surfaces VII.

Xie, Y., Qian, Y., Wang, W., Zhang, S., & Zhang, Y. (1996). A Benzene-Thermal Synthetic Route to Nanocrystalline GaN. *Science, 272*(5270), 1926-1927. doi:10.1126/science.272.5270.1926

Xu, X., Ray, R., Gu, Y., Ploehn, H. J., Gearheart, L., Raker, K., & Scrivens, W. A. (2004). Electrophoretic Analysis and Purification of Fluorescent Single-Walled Carbon Nanotube Fragments. *Journal of the American Chemical Society, 126*(40), 12736-12737. doi:10.1021/ja040082h

Yamamoto, A., Sasao, T., Goto, T., Arai, K., Lee, H. Y., Makino, H., & Yao, T. (2003). Anti-Stokes photoluminescence in CdSe self-assembled quantum dots. *physica status solidi (c)*(4), 1246-1249.

Yan, X., Cui, X., Li, B., & Li, L.-s. (2010). Large, Solution-Processable Graphene Quantum Dots as Light Absorbers for Photovoltaics. *Nano Letters, 10*(5), 1869-1873. doi:10.1021/nl101060h

Yang, C., Zhong, Z., & Lieber, C. M. (2005). Encoding electronic properties by synthesis of axial modulation-doped silicon nanowires. *Science, 310*(5752), 1304-1307.

Yang, D., Chen, Q., & Xu, S. (2007). Synthesis of CdSe/CdS with a simple non-TOP-based route. *Journal of luminescence, 126*(2), 853-858.

Yang, H., & Holloway, P. H. (2003). Enhanced photoluminescence from CdS: Mn/ZnS core/shell quantum dots. *Applied Physics Letters, 82*, 1965.

Yang, H., & Holloway, P. H. (2004). Efficient and photostable ZnS-passivated CdS: Mn luminescent nanocrystals. *Advanced Functional Materials, 14*(2), 152-156.

Yang, H., Holloway, P. H., Cunningham, G., & Schanze, K. S. (2004). CdS: Mn nanocrystals passivated by ZnS: Synthesis and luminescent properties. *The Journal of chemical physics, 121*(20), 10233-10240.

Yang, H., Santra, S., & Holloway, P. H. (2005). Syntheses and applications of Mn-doped II-VI semiconductor nanocrystals. *Journal of nanoscience and nanotechnology, 5*(9), 1364-1375.

Yang, H., Yin, W., Zhao, H., Yang, R., & Song, Y. (2008). A complexant-assisted hydrothermal procedure for growing well-dispersed InP nanocrystals. *Journal of Physics and Chemistry of Solids, 69*(4), 1017-1022. doi:http://dx.doi.org/10.1016/j.jpcs.2007.11.017

Yeh, H.-C., Sharma, J., Han, J. J., Martinez, J. S., & Werner, J. H. (2010). A DNA− Silver nanocluster probe that fluoresces upon hybridization. *Nano letters, 10*(8), 3106-3110.

Yeh, H.-C., Sharma, J., Shih, I.-M., Vu, D. M., Martinez, J. S., & Werner, J. H. (2012). A fluorescence light-up Ag nanocluster probe that discriminates single-nucleotide variants by emission color. *Journal of the American Chemical Society, 134*(28), 11550-11558.

Yong-Ji, L., Tae-Geun, K., & Yun-Mo, S. (2006). Lattice distortion and luminescence of CdSe/ZnSe nanocrystals. *Nanotechnology, 17*(14), 3539. Retrieved from http://stacks.iop.org/0957-4484/17/i=14/a=030

Yong, K.-T., Ding, H., Roy, I., Law, W.-C., Bergey, E. J., Maitra, A., & Prasad, P. N. (2009). Imaging pancreatic cancer using bioconjugated InP quantum dots. *Acs Nano, 3*(3), 502-510.

Yordanov, C., & Minkova, L. (2005). Fractionated crystallization of compatibilized LDPE/PA6 blends. *European polymer journal, 41*(3), 527-534.

Yu-Hong, Z., Jian-Hua, Z., Jing-Feng, B., Wei-Zhu, W., Yang, J., Xiao-Guang, W., & Jian-Bai, X. (2007). Cr-doped InAs self-organized diluted magnetic quantum dots with room-temperature ferromagnetism. *Chinese Physics Letters, 24*(7), 2118.

Yu, J., Choi, S., & Dickson, R. M. (2009). Shuttle-Based Fluorogenic Silver-Cluster Biolabels. *Angewandte Chemie, 121*(2), 324-326.

Yu, J. H., Liu, X., Kweon, K. E., Joo, J., Park, J., Ko, K.-T., . . . Son, J. S. (2010). Giant Zeeman splitting in nucleation-controlled doped CdSe: Mn2+ quantum nanoribbons. *Nature materials, 9*(1), 47-53.

Yu, W. W., & Peng, X. (2002). Formation of high-quality CdS and other II-VI semiconductor nanocrystals in noncoordinating solvents: tunable reactivity of monomers. *Angew Chem Int Ed Engl, 41*(13), 2368-2371. doi:10.1002/1521-3773(20020703)41:13<2368::aid-anie2368>3.0.co;2-g

Yu, W. W., Wang, Y. A., & Peng, X. (2003). Formation and stability of size-, shape-, and structure-controlled CdTe nanocrystals: ligand effects on monomers and nanocrystals. *Chemistry of Materials, 15*(22), 4300-4308.

Yupapin, D. P., Pivsa-Art, D. S., Ohgaki, D. H., Wongpisutpaisan, N., Charoonsuk, P., Vittayakorn, N., & Pecharapa, W. (2011). 9th Eco-Energy and Materials Science and Engineering SymposiumSonochemical Synthesis and Characterization of Copper Oxide Nanoparticles. *Energy Procedia, 9*, 404-409. doi:http://dx.doi.org/10.1016/j.egypro.2011.09.044

Zhang, H., Huang, H., Ming, H., Li, H., Zhang, L., Liu, Y., & Kang, Z. (2012). Carbon quantum dots/Ag3PO4 complex photocatalysts with enhanced photocatalytic activity and stability under visible light. *Journal of Materials Chemistry, 22*(21), 10501-10506. doi:10.1039/C2JM30703K

Zherebetskyy, D., Scheele, M., Zhang, Y., Bronstein, N., Thompson, C., Britt, D., . . . Wang, L. W. (2014). Hydroxylation of the surface of PbS nanocrystals passivated with oleic acid. *Science, 344*(6190), 1380-1384. doi:10.1126/science.1252727

Zhong, X., Han, M., Dong, Z., White, T. J., & Knoll, W. (2003). Composition-Tunable Zn x Cd1-x Se Nanocrystals with High Luminescence and Stability. *Journal of the American Chemical Society, 125*(28), 8589-8594.

Zhou, J., Booker, C., Li, R., Sun, X., Sham, T.-K., & Ding, Z. (2010 (a)). Electrochemistry and electrochemiluminescence study of blue luminescent carbon nanocrystals. *Chemical Physics Letters, 493*(4–6), 296-298. doi:http://dx.doi.org/10.1016/j.cplett.2010.05.030

Zhou, X., Zhang, Y., Wang, C., Wu, X., Yang, Y., Zheng, B., . . . Zhang, J. (2012 (b)). Photo-Fenton reaction of graphene oxide: a new strategy to prepare graphene quantum dots for DNA cleavage. *ACS Nano, 6*(8), 6592-6599. doi:10.1021/nn301629v

Zhu, H., Wang, X., Li, Y., Wang, Z., Yang, F., & Yang, X. (2009). Microwave synthesis of fluorescent carbon nanoparticles with electrochemiluminescence properties. *Chem Commun (Camb)*(34), 5118-5120. doi:10.1039/b907612c

Zhu, J., Koltypin, Y., & Gedanken, A. (2000). General Sonochemical Method for the Preparation of Nanophasic Selenides: Synthesis of ZnSe Nanoparticles. *Chemistry of Materials, 12*(1), 73-78. doi:10.1021/cm990380r

LIST OF PUBLICATIONS

1. Hamizi, N. A., Aplop, F., Haw, H. Y., Sabri, A. N., Wern, A. Y. Y., & Johan, M. R. (2016). Tunable optical properties of Mn-doped CdSe quantum dots synthesized via inverse micelle technique. *Optical Materials Express, 6*(9), 2915-2924.

2. Hamizi, N. A., & Johan, M. R. (2012a). Enhanced ripening behaviour of cadmium selenide quantum dots (CdSe QDs). *Int. J. Electrochem. Sci, 7*, 8473-8480.

3. Hamizi, N. A., & Johan, M. R. (2012b). Optical properties of CdSe quantum dots via non-TOP based route. *International Journal of Electrochemical Science, 7*, 8458-8467.

4. Hamizi, N. A., Ying, C. n. S., & Johan, M. R. (2012). Synthesis with Different Se Concentrations and Optical Studies of CdSe Quantum Dots via Inverse Micelle Technique. *International Journal Of Electrochemical Science, 7*(5), 4727-4734.